Glasses for Energy Applications: Atomic Scale Network Structure and Properties

Thorsten Stechert

Submitted in part fulfilment of the requirements for the degree of Doctor of Philosophy in Materials Science and Engineering of Imperial College London

This hereby declare that this thesis is my original work, which is written in my own words, unless proper references are given.

T.R. Stechert

Abstract

Glass is used for the vitrification of high level waste that results from the reprocessing of spent nuclear fuel. A better understanding of the structure of vitrified wastes may lead to insights into the observed compositional flexibility. It is also the starting point for studies of the self-irradiation behaviour of glasses under long-term repository conditions.

Appropriate models need to be employed for the study of glasses when using molecular dynamics. The nature of nuclear waste necessitates an accurate structure prediction for a range of compositions and parameters. To this end, the suitability of established potential sets have been compared.

The established potential models were used to investigate the structure of zinc containing sodium silicate glass. Once validated, this structure was used to investigate structural changes observed during simulated self-irradiation, where significant changes were observed on the atomic scale. This will provide the basis for further studies of radiation damage, glass-crystal interfaces and damage across glass-crystal interfaces.

In order to further enhance the understanding of potential models, a novel glass of composition $LiAlF_4$ has been successfully described, and may become relevant in the future as a thin film coating in Li-ion batteries .

Acknowledgements

First and foremost I would like to thank my supervisor Robin Grimes for making this thesis possible. You have accompanied my academic journey since my very first day at Imperial, way back as a prospective student in 2005. Your uncanny ability to make even the most mundane seem miraculous and exciting, while also being able to explain the most complex concepts in simple terms (even to me) fascinates me to this day. I am truly grateful for your continued support and encouragement throughout my studies and for always finding time for me even though you had none to spare.

I wish to thank the DIAMOND consortium as a whole and Jim Young in particular, not only for financial support, but also for organising and hosting so many interesting and thoroughly enjoyable conferences and events.

I am grateful to the other members of the Atomistic Simulation Group (past and present), whose wit, open minds and open hearts have made my time at Imperial and the many nights at the Union and the Holland Bar thoroughly enjoyable. I want to thank Rizgar for his insight and humour, Sam for his friendship and encouragement (I can not imagine a better dad), and Emma for her lending an ear and support to me with all manner of problems throughout the years. Two members of the group stand out, who have spent a considerable amount of time to help me finish this thesis: Elly and Michael.

Michael, you have taught me so many things over the years that it would be impossible to list them all. You have spent countless hours discussing the merits of my crazy ideas, helping me out with your vast technical knowledge and of course reading through my thesis and various papers and documents over the years, often many times over. I cannot thank you enough for always encouraging me to do better, inspiring me to seek new ways of solving problems. Above all, you always had time for me, be it in the office, on a park bench or in the pub with a cold pint of “Star”.

Elly, I cannot thank you enough for being there for me, especially during the hardest stages of my PhD. Your big heart always made me feel like part of a family and not just a group of colleagues. From living it up in the San Francisco to getting stuck in Argentina but making the best of it, you are part of many fond memories. Your encouragement and support went far beyond simply proofreading the many chapters of my thesis and for that I am truly grateful.

Working on a PhD is not always easy, and I often found myself doubting my ability to complete it. I was very fortunate to have three of my best friends, Hok Man, Sergey and Alan do a PhD of their own. While we may have been working on different things, in different research groups and in a different country, I am truly grateful to you for helping to keep me on track and I am immensely proud of what we have achieved together. May our friendship last a lifetime.

Thank you Mama and Papa, for without your continued support I would not have been able to come to Imperial College in the first place, let alone finish this thesis. You have given up much to allow me to pursue my dreams and I will never forget that. Many a time it was just the sound of your voices and your words of encouragement that provided all the motivation I needed to continue with this thesis to the end.

Table of Contents

List of Figures

List of Tables

Acronyms

AGR advanced gas reactor

BKS Beest-Kramer-Santen (potentials)

BO Bridging oxygen

BWR boiling water reactor

DFT density-functional theory

GULP General Utility Lattice Program

HLW high level waste

HXRD Hard X-Ray diffraction

ILW intermediate level waste

LLW low level waste

MAE mixed alkali effect

MAS magic angle spinning

MD Molecular Dynamics

MOX mixed oxide

Mtoe Megatons of oil equivalent

NBO non-bridging oxygen

NFC nuclear fuel cycle

NMR nuclear magnetic resonance

OECD Organisation for Economic Co-operation and Development

PDF pair distribution function

PKA primary knock-on atom

PWR pressurised water reactor

SEI solid electrolyte interphase

SNF spent nuclear fuel

SRIM Stopping and Range of Ions in Matter

THORP thermal oxide reprocessing plant

TRIM Transport of Ions in Matter

U.S. United States of America

UK United Kingdom of Great Britain and Northern Ireland

VLLW very low level waste

VMD Visual Molecular Dynamics

XRD X-Ray diffraction

ZBL Ziegler-Biersack-Littmark (potential)

1 Introduction

1.1 The Energy Landscape

The provision of reliable energy sources is likely to be one of the defining challenges of the 21st century. The availability of fossil fuels such as coal, oil and natural gas and to a lesser extent, mineable minerals such as uranium oxide for use as fuel in nuclear reactors have not only allowed unprecedented economic growth in the 20th century, but have defined the foundations of our economies [1]. In the past energy could be treated like any other commodity, and with the exception of the politically motivated 1973 and 1979 oil crises [2, 3], supply of fossil fuels and other energy sources have always been able to meet demand [4], despite markedly increased energy consumption in the last 50 years [4].

As of 2011, 10.2% of the primary energy supply[1] in OECD (Organisation for Economic Co-operation and Development) countries is made up by nuclear energy [4]. Estimates on the availability of fossil fuels are hard to make, and only recently the exploitation of unconventional oil, such as shale oil may lead to a reassessment of oil reserves [6].

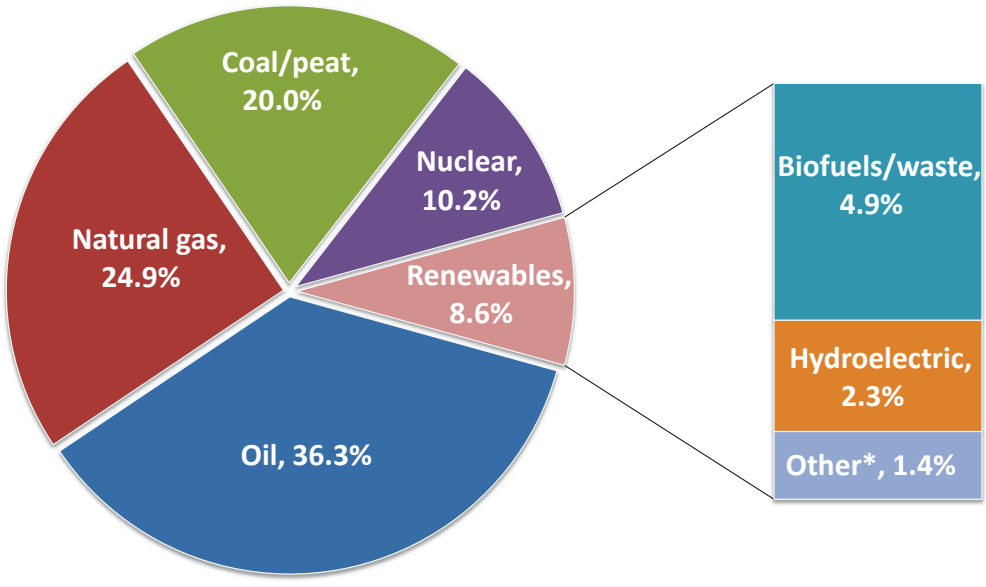

Figure 1.1 – OECD Total Primary Energy Supply (5305 million tons of oil equivalent (Mtoe)) by Fuel, with data from the International Energy Agency [4]. (*Other includes geothermal, solar, wind, heat, etc.)

[1] Primary energy supply refers to the total energy used by humanity (including power plants, transportation, etc.), but does not include losses due to energy losses or the inevitable inefficiencies in energy conversion (e.g. from the Carnot cycle [5]).

The problem of energy production is not just a problem of supply and demand though, but is also related to the responsible and sustainable use of energy. As rising sea levels [7], rising temperatures [7] and events such as the Fukushima nuclear disaster have tragically illustrated, it does not only matter how much energy we use, but also how this energy is generated, stored, transmitted and eventually consumed. With fossil fuels accounting for over 80% [4] of all primary energy supply in OECD countries, a diversification of energy supply is necessary for both energy security and to limit CO_2 production.

These problems demand solutions from scientists, politicians and our societies as a whole. We must, however, not only look to solving problems of the present and future, but in some cases, face unresolved issues of the past. One such issue is the potentially dangerous radioactive material left over from academic and military research, industrial activity and from the operation of civil and military nuclear reactors.

In this work, two very different sides of the energy problem will be discussed. On the one hand, the work aims to help provide insights into the safe disposal of radioactive waste that is continuously generated by nuclear power plants. On the other hand, new ways of improving the storage of energy in batteries will be discussed. The overarching theme connecting these important issues are the properties of glasses and their investigation by molecular dynamics simulations. The study of glasses can provide unique insights and potential improvements to existing and novel materials in energy applications.

1.2 Glass - An Amorphous Material

1.2.1 A Brief History of Glass Science

As this thesis is dedicated to glasses, a good understanding of the unique characteristics of amorphous materials in general and glasses in particular is required. Glass is one of the oldest processed materials known to man, with glass fragments having been found in Iraq dating back to 1500 B.C. [8]. The technique of making glassy materials from sand, however, is likely to be even older. Whilst many civilizations such as the Romans prized glass highly for its colour and transparency, the processes by which crystalline sand is turned into an amorphous glass was little understood, being more of an art than a science for millennia. It was not until the first half of the 20th century that there was shift in glass-making from an art and a craft to a

field of scientific study. Most of the work in the field of glass science originated from William Houlder Zachariasen who published his paper on "The Atomic Arrangement in Glass" in 1932 [9]. Whilst earlier works by Otto Schott and other glass makers led to the discovery of new glasses [10] (such as the borosilicate glass system), the scientific work on glasses up until then was focussed on making new glasses for particular (usually optical) applications, rather than trying to understand the atomic structure of these materials in detail [10].

Zachariasen developed a theory [9] according to which the local bonding in glasses is very similar to that of crystalline materials of the same composition. Both materials are made up of atoms bonded together into structural units, that is polyhedra (the most important structural unit in silicate glasses is the SiO_4 tetrahedron, which is illustrated in figure 1.2). The difference between glasses and crystals is, that while crystals have structural units that are connected in such a way as to periodically repeat themselves, in glasses, they are connected in a random manner. Zachariasen wrote: *"The presence or absence of periodicity and symmetry in the network distinguishes a crystal from a glass."* [9] He went on to explain why some oxides may form glasses, whilst others do not and formulated four rules which must be fulfilled for the formation of glasses from an oxide:

"An oxide may be formed (1) if the sample contains a high percentage of cations which are surrounded by oxygen tetrahedra or by oxygen triangles; (2) if these tetrahedra or triangles share only corners with each other and; (3) if some oxygen atoms are linked to only two such cations and do not form further bonds with other cations." [9].

The original drawing, showing a two-dimensional representation of a simple silicate glass structure, reproduced in figure 1.3. While this describes the situation in silicate glasses quite well, aluminium-fluoride glasses, which will be discussed later on in this thesis feature octahedral structural units or edge-sharing polyhedra instead. Similarly, Zachariasen predicted that the only fluoride material able to form a glass is BeF_2, whereas this work will show that other fluoride glass formers do indeed exist. Since Zachariasen's pioneering paper [9], much more work has been done on the theory of glasses, which has evolved from the luxury material of antiquity, to a modern engineering material found in anything from tableware to state-of-the-art electronic devices [11].

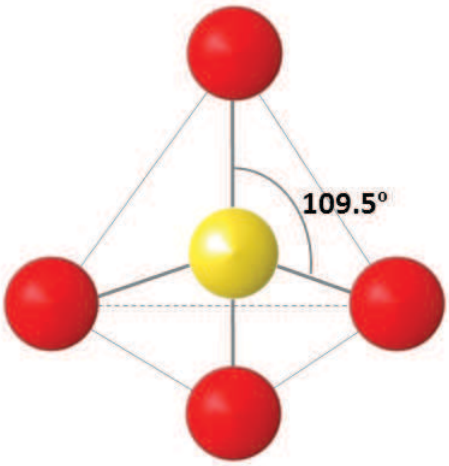

Figure 1.2 – Schematic of a silicon oxide tetrahedron: A single silicon ion (yellow) is coordinated by four oxygen ions (red), with an internal O-Si-O bond angle of 109.5°.

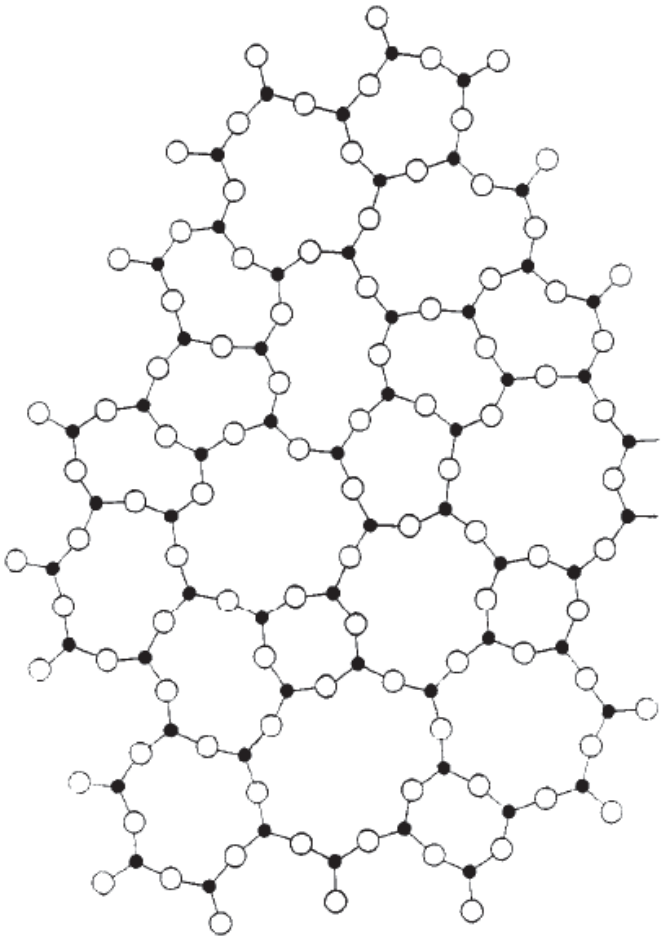

Figure 1.3 – Zachariasen's original drawing describing the random network structure of a silicate glass. The dots represent silicon ions, while the open circles represent bonded oxygen ions [9].

1.2.2 Glass Components

Glasses are made up of various component oxides, which are added to perform different roles in the formation of the glass network. Additionally, it may be necessary to add further constituents to help with processing or to slightly alter the properties of the glass, such as metal oxides used to colour or de-colour the glass via redox reactions [12]. The three fundamental roles in the formation of the glass network are outlined below.

Network Formers: A network former is an oxide capable of forming a glass network structure of linked polyhedra. These include oxides such as SiO_2, GeO and B_2O_3 and provide the chemically bonded network of polyhedra (SiO_4, BO_4, etc.) by means of some of the anions being corner-shared between two polyhedra (edge- and face-sharing is also possible in some glasses). In a silicate glass made up of only network formers, all anions are shared (also called bridging). The proportion of shared anions can be reduced by adding network modifiers.

Network Modifiers: These constituents are responsible for breaking up the bonds between polyhedra, by providing the cations necessary to charge-balance the anions. A common example in commercial silicate glasses is Na_2O, which makes processing a lot easier by increasing the temperature range over which these glasses melt. In addition, the lowering of the processing temperatures decreases the cost of the glass product.

Network Intermediates: As the name suggests, network intermediates fulfil the role of either a network former or a network modifier, depending on the composition. Oxides such as Al_2O_3, TiO_2 and ZnO can not form a network by themselves, but may act in a manner similar to a network former as a component of a glass [10]. This means that they also tend to form polyhedra, but these are often not charge-balanced when forming edge-sharing polyhedra (e.g. ZnO_4), and may not be stable without the presence of other elements, such as alkalis. They may also modify the network, for example by forming octahedra in a network made up of tetrahedra.

1.2.3 Types of Glasses

Typically, the stoichiometry of glasses is given by the weight or molar ratio of constituent oxides (or fluorides), rather than the elements. This stems from the use of these constituents in the preparation of the glass batch[2] [10]. By fine-tuning the ratio of these constituents, the properties of glasses can be tailored. Based on the constituents, below are some typical glasses with industrial applications:

Soda-Lime Glass:

The most widely used glass is soda-lime glass, which is named after the inclusion of soda (Na_2CO_3) and lime ($CaCO_3$) in its composition, both of which are cheap and provide the constituent oxides Na_2O and CaO. Soda is added to lower the melting temperature and make the glass cheaper to produce. Unfortunately, sodium also makes the glass water soluble and soft. To counter this problem, lime is added, which provides some chemical durability and improved the hardness of the glass. Various other oxides such as MgO and Al_2O_3, as well as impurities such as Fe_2O_3 may also be present in the composition [10,13].

Borosilicate Glass:

This glass composition has many industrial uses, as it is more chemically durable and has a higher melting temperature and a lower coefficient of thermal expansion compared to ordinary soda-lime glass. This is achieved through the addition of boron oxide (B_2O_3) [13]. Borosilicate glass is sometimes known by its Schott brand name of Duran or the Corning brand name Pyrex [10,13]. It is found anywhere from laboratory glass ware to kitchenware, as the base glass for nuclear waste immobilisation or in any application where its superior thermal properties are required, but the high melting point makes it too expensive for some consumer products.

[2]The glass batch is the mix of raw materials fed into the glass melter (either continuously or in a single batch) to form the glass.

Lead Glass

Often misleadingly called crystal glass, this glass is not crystalline, but is similar in appearance to rock crystal. It contains lead oxide (PbO), which is responsible for its increased refractive index, making the glass appear more brilliant [10]. The attractive optical properties are mostly useful in consumer products, but the inclusion of the heavy element lead, also makes these types of glasses suitable for radiation shielding [14].

Phosphate Glasses

Glasses based on the phosphate (P_2O_5) system are often used in biomedical glasses in applications such as bone scaffolds, as they can be absorbed by the human body over time [15]. Their differing optical properties makes them useful in some photonic applications, for instance as laser waveguides. Finally, phosphate glasses have high chemical durability, which is why they can also be used as a nuclear waste host material [16–18].

Fluoride Glasses

These glasses rely on the fluorides of various metals, such as fluoroaluminate glass, which contains AlF_3 and fluorozirconate glass which contains ZrF_4. They are mainly used in optical fibres, where their lack of oxygen means they are non-absorbing in different parts of the optical spectrum in comparison to silicate glasses [19]. Recently, glasses of this composition have also been suggested for use in electrochromic devices and lithium-ion batteries [20, 21].

1.3 Categorising Nuclear Waste

One area where glasses are used is in the immobilisation of radioactive elements resulting from operation of nuclear power plants, scientific research, the medical industry or the military [17, 18, 22]. The UK in particular is in the difficult position of having to tackle a large variety of waste streams with varying elemental compositions that require disposal [23]. Glasses can be used to provide a host material for these dangerous elements, and are a widely used host material for the long-term disposal of nuclear waste, particularly highly radioactive waste [24, 25].

The oldest nuclear waste in the UK dates back to the early Cold War and Britain's desire to obtain nuclear weapons as fast as possible [18,25]. To that aim, little consideration was given to the quantity and kind of waste produced from these experiments. Since nuclear power became available for civil use, Britain has built three commercial reactor designs in addition to several research reactors [26]. This has led to a wide variety of waste compositions, each calling for specialised treatment, making a standardised disposal procedure more complex.

The problem of nuclear waste poses significant technical and socio-economic difficulties, since the waste resulting from the reprocessing of nuclear fuel used in power generation is highly radioactive, containing large quantities of unstable isotopes. This makes it not only difficult to find suitable disposal routes and sites for the differing wastes, but also exerts pressure on the government to secure political support for such disposal actions, which may last for decades and will affect future generations.

Efforts are being made to provide long-term storage for the UK's current stockpile of nuclear waste [23,27,28]. Nevertheless, no permanent repository has been built to accommodate it. So far, it is also not clear what materials will need to be disposed of. Plutonium and spent fuel in particular were long regarded as a resource from which to manufacture mixed oxide (MOX) fuel [23], but with stockpiles growing, disposal is also being considered [27].

Although the problem of waste disposal has yet to be solved, new nuclear power plants are being built. Considering the already accumulated stockpile of legacy wastes, this make it more important than ever to properly understand the properties and potential challenges of these vitrified waste forms.

1.3.1 Radioactivity

The nature of nuclear waste is largely determined by the type(s) and intensity of radiation that is emitted from it. Usually, these will be related to decay processes (i.e. resulting from an inherent instability of the involved isotopes), but activated processes as a result of neutrons interacting with ions can also occur. Ionising radiation is of particular interest in the treatment of nuclear waste, as it has the potential of stripping electrons from other atoms, thus being able to break bonds. The four basic types of ionising radiation are:

α-radiation

The origin of α-radiation is the nuclear binding energy (plotted in figure 1.4 as a function of nucleon number), which shows how the number of nucleons (i.e. the combined number of protons and neutrons) affects the energy of the nucleus. Nuclei with very high mass numbers can thus release energy by emitting nucleons (the basis of fission and α-decay), while nucleons with low mass numbers can release energy by incorporating more nucleons (the basis of nuclear fusion).^{62}Ni is the most stable isotope, and any higher mass number nuclei will have lower average binding energy per nucleon. In alpha radiation, two neutrons and two protons are simultaneously shed from a nucleus in the form of an α-particle (which is effectively a helium nucleus with a 2^+ charge, as it has no attached electrons). For example, an important α-decay process is that of the most common uranium isotope, ^{238}U:

$$^{238}_{92}\mathrm{U} \longrightarrow {}^{234}_{90}\mathrm{Th} + {}^{4}_{2}\mathrm{He}$$

Fission In the more general case, it is also possible for the emitted daughter nucleus to be larger than helium. This is usually the case when an external particle (e.g. a neutron) impacts a heavy nucleus such as ^{235}U, causing it to split into two or more nuclei as well as a number of other particles (such as neutrons, electrons and positrons). The average fission yield of this process is shown in figure 1.5. This particular reaction is a very important concept in nuclear waste, as the fission of the fissile isotope ^{235}U is the most important reaction to occur in a conventional reactor, and is largely responsible for the distribution of radioactive isotopes found in the resulting waste (although later in fuel life fission of ^{239}Pu also becomes important). While α-particles have high mass and are charged (meaning they can easily strip electrons from other atoms), their range is very limited and a few millimetres of paper (or skin) are enough to stop this kind of radiation. The large momentum transfer over small distance due to the α-particle itself, as well as the corresponding recoil nucleus and primary knock-on atom (PKA) makes α-emitting waste highly damaging to the waste material. As a biological risk to humans however, α-emitting nuclei are only problematic when they are released from the storage material and become water or airborne (at which point it could be inhaled and ingested).

Self-damage of the nuclear waste can occur from all types of radiation, but the short-range,

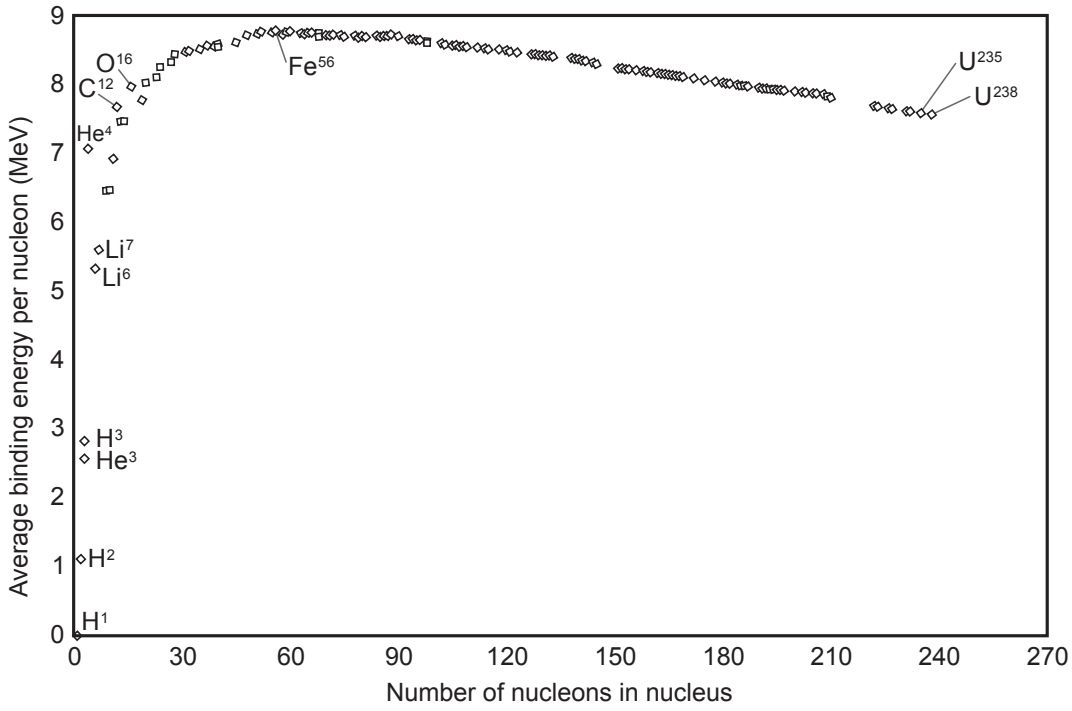

Figure 1.4 – Nuclear binding energy as a function of number of nucleons in the nucleus, copied from [29].

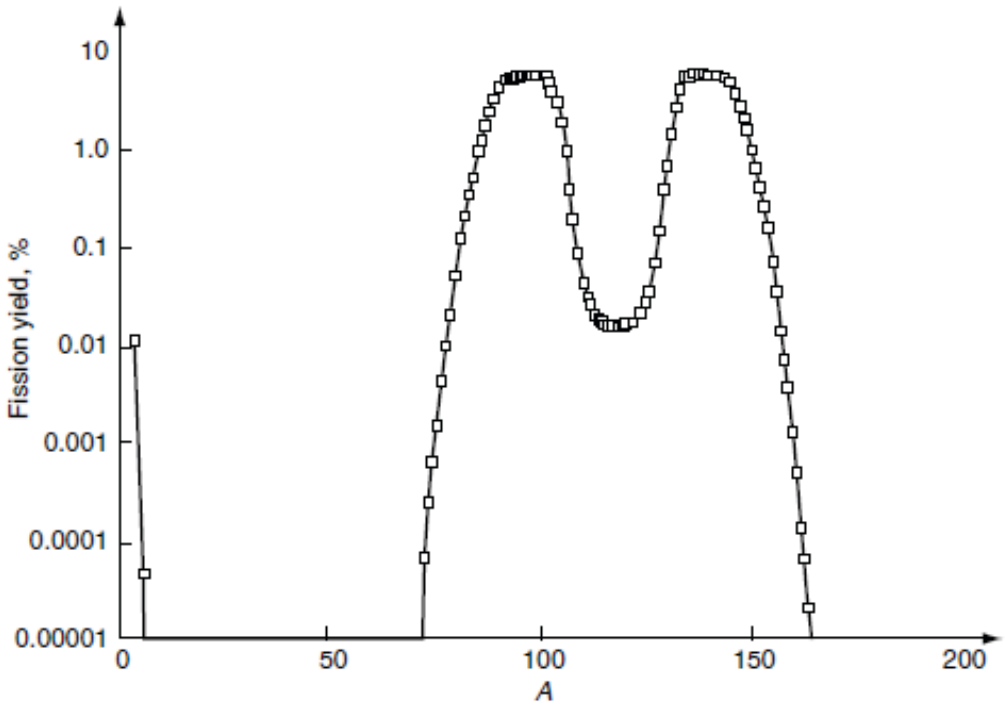

Figure 1.5 – Fission products of ^{235}U and their mass numbers (A), copied from [17].

high-energy α-radiation is particularly problematic, as it is the most ionising type of radiation [22]. The α-decay of ^{238}U for example generates both an α-particle of energies between 4.5 and 5.5 MeV and as well as a recoil nucleus (the parent ion) of energy between 10 and 70 keV [22]. The damage caused by the α-particle occurs mostly by ionisation and the overall displacive energy is estimated to be as low as 6% [30]. Ionisation damage can lead to the breakup of bonds within the waste, potentially leading to the release of previously immobilised species. In terms of wasteform design however, the highly localised damage caused by the recoil nucleus and the primary knock-on atom (i.e. the first atom impacted by the high-energy α-particle) are very challenging. The elastic collisions can lead to the displacement of atoms along the particle and recoil trajectories, which can have a significant effect on host material properties [31, 32]. For example, recoil trajectories have been shown to lead to the formation of amorphous channels in crystalline waste materials [22]. Furthermore, cracks and grain-boundary degradation can occur as a result of the atomic displacements [22].

β-radiation

Another important type of ionising radiation is β-radiation. β-decay processes are very common and occur when the ratio of protons to neutrons in the nucleus is either too high or too low. This often occurs readily after either an α-decay or fission process, as the stable ratio changes as a function of mass number (shown in figure 1.6). The two β-decay processes are:

$$\beta^- \text{decay: } {}^{A}_{Z}\mathrm{X} \longrightarrow {}^{A}_{Z+1}\mathrm{Y} + \bar{\nu} + \mathrm{e}^-$$

$$\beta^+ \text{decay: } {}^{A}_{Z}\mathrm{X} \longrightarrow {}^{A}_{Z-1}\mathrm{Y} + \nu + \mathrm{e}^+$$

In each case, a parent nucleus of element X transforms into a new element Y with a proton number (Z) one higher (β^+ decay) or one lower (β^- decay) than before, while maintaining its mass number (A). This is achieved by a neutron decaying into a proton, an electron and an antineutrino ($\bar{\nu}$), or by a proton decaying into a neutron, a positron and a neutrino (ν). β-radiation can travel long distances through air, and a few millimetres of metallic shielding (ideally lead due to its high mass, which is usually used to slow and capture the charged electrons/positrons). While of high energy, electrons produced by β-decay are of comparatively low mass. As such, most of their damage is caused by ionisation, making β-radiation

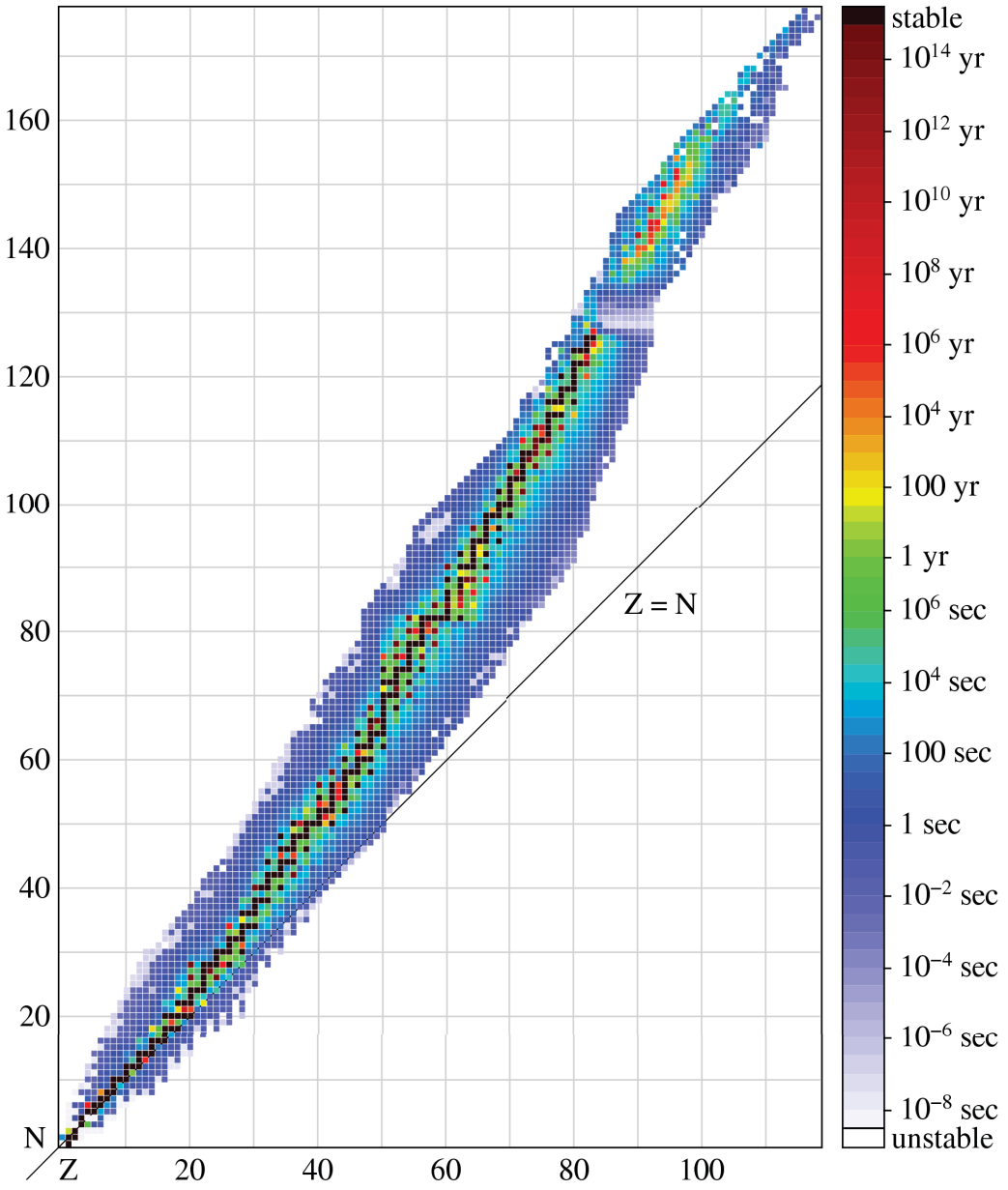

Figure 1.6 – Isotopes and their half-lives, as determined by the number of protons (Z) and neutrons (N) [33].

most damaging in materials susceptible to radiolysis (bond-breaking by radiation), such as cements [22].

γ-radiation

Gamma radiation is the highest energy (lowest wavelength) type of electromagnetic radiation, but the least ionising form of radiation. It commonly occurs as a consequence of other decay types, which may leave a nucleus in a highly excited state. The emission of excess energy as electromagnetic radiation allows these excited nuclei to lower their energy levels. As such, γ-radiation is actually a high-energy case of the more general emission of photons from excited ions. Due to the high energy of the emitted photons, as well as the lack of any charge, this type of radiation can easily penetrate most matter, but can equally ionise atoms by exciting electrons with enough energy to be ejected from the nucleus via the so-called photoelectric effect, or Compton scattering.

Like β-radiation, γ-radiation is most damaging to materials which suffer from radiolysis [22]. Furthermore, the high energies of γ-radiation may mean that the damage is not actually occurring within the waste, but can damage or weaken the waste container itself [17].

Neutrons

In addition to these types of radiation, free neutrons are also considered a form of radiation and can ionise atoms indirectly. This occurs, for example, when a neutron is captured by another atom, thus forming a different isotope and resulting in gamma emission, which ionises another atom. Due to the high mass and energy of neutrons and the lack of charge, neutrons can be highly penetrating in areas of low average atomic mass (such as water), as the atomic mass is proportional to the ability of an atom to stop and absorb a neutron. A common neutron capture reaction is the capture of a neutron by ^{239}Pu to form ^{240}Pu:

$$^{239}\mathrm{Pu} + \mathrm{n} \longrightarrow ^{240}\mathrm{Pu}$$

Neutron capture reactions are also exploited in breeder reactors, where ^{239}Pu can be bred from the non-fissile uranium isotope ^{238}U (by far the most common U isotope):

$$^{238}\mathrm{U} + \mathrm{n} \longrightarrow ^{239}\mathrm{U} \xrightarrow{\beta^-} ^{239}\mathrm{Np} \xrightarrow{\beta^-} ^{239}\mathrm{Pu}$$

1.3.2 Types of Nuclear Waste

Nuclear waste is typically categorised by the type and intensity of radiation originating from the isotopes in the waste, as well as the intensity of heating occurring as a result of decay processes within the waste. Radioactive waste can be broadly classified into five major categories [17,34]:

Very Low Level Waste (VLLW)

In the UK, the radiation limit above which material is treated as managed nuclear waste is 4 GBq of β and/or γ-radiation per cubic metre. Waste below this limit is classified as very low level waste (VLLW) and can either be low volume or high volume. Low volume VLLW is disposed of in a regular landfill alongside ordinary rubbish, while high volume VLLW goes to a specialised landfill.

Low Level Waste (LLW)

LLW is only lightly radioactive. Typical examples include parts of the structural materials used in nuclear power plants, and everyday products, such as hospital wastes, protective clothing and lab supplies. Low level waste has radiation above the lower bounds for VLLW, but below 4 GBq of α-radiation per tonne or 12 GBq of β-radiation and γ-radiation per tonne [34].

Intermediate Level Waste (ILW)

ILW is waste which is more radioactive than LLW, but not so heat generating that larger quantities could not be stored in close proximity. Typically this includes the fuel cladding swarf left over from fuel decanning, plutonium contaminated materials and scrapped equipment [34]. ILW exceeds the radiation limits for LLW, without being at risk of significantly raising the temperature of the waste as a result of the radioactivity.

High Level Waste (HLW)

HLW is not only highly radioactive (like ILW), but is also expected to be highly heat generating [34]. This can lead to potential safety issues in short-term disposal, as sufficient cooling is necessary to prevent melting and potential radiation hotspots. It typically comprises waste from reprocessed spent nuclear fuel and any materials which have been highly contaminated by fission products (such as the interior fuel cladding and the reactor core). While the PUREX process reduces the minor actinide concentration, the large variety of radioactive elements still make this the most difficult class of waste to dispose of. The high content of ^{90}Sr and ^{137}Cs are particularly problematic in the short term, as their respective half-lifes of 28.8 and 30.2 years make the waste significantly heat generating, while the longer lived isotopes such as ^{126}Tin with a half-life of 230,000 years mean that it remains significantly radioactive for a long period of time.

Spent Nuclear Fuel (SNF)

SNF is the summary term for used fuel rods from a nuclear power station. It is only classified as nuclear waste in countries that operate an open nuclear fuel cycle (NFC) such as the U.S. [35]. In countries with a closed NFC, uranium and plutonium are seen as resources and are extracted from the spent nuclear fuel (via reprocessing) prior to disposal of the residual material as HLW.

The origins, classification and disposal routes of the various types of waste are summarised in Table 1.1.

1.4 The Evolution of Nuclear Waste

Through time, the types, origins and disposal routes for nuclear waste have changed significantly. In the 1950s and early 1960s, there was a large effort to produce fissile material for both research and nuclear weapons programmes [18]. This meant that large quantities of other radioactive isotopes, not suitable for fission were created as by-products, and so these early types of legacy wastes vary a lot in their composition and radioactivity [17]. As nuclear waste is rarely homogeneous and can exist in all manner of shapes and sizes, a common approach

Table 1.1 – Waste origins, classification and disposal routes. Adapted from [23] and [27]

Classification	Sources/origins	Disposal route	Waste host
VLLW	hospitals, industry	landfill (sometimes post-incineration)	
LLW	decommissioning, hospitals, research, industry	managed site	cement
ILW	reprocessing (e.g. cladding swarf), power plant operation	geological repository (planned)	cement
HLW	reprocessed fuel	geological repository (planned)	glasses (e.g. borosilicate), ceramics (e.g. Synroc)
SNF	irradiated fuel	reprocessing	none, glasses (e.g. borosilicate), ceramics (e.g. Synroc)

that is still used today is to first dissolve the waste in nitric acid. Unfortunately, this leads to large volumes of acidic liquor which need to be stored or otherwise processed. In the U.S., the resultant acidic liquor from research and military projects was initially stored at two sites: the Hanford and Savannah River plants [34]. Due to a shortage of stainless steel in the aftermath of World War II, single walled carbon steel tanks were built underground for the liquid waste to be pumped into [18]. The secrecy of the projects and the prospect of a nuclear war meant that the lax treatment of highly dangerous wastes did not gather the attention it deserved. Indeed, nuclear waste was treated much like a conventional waste, which could be partially disposed of by dispersion in the wider environment [36]. This led to a daily release of radiation in the terabecquerel range, freely entering the adjoining Columbia river, an important fresh water source in the state of Washington [37]. Another series of leaks in early 2013 [38] prove that the problems of legacy waste at Hanford persist, even more than sixty years after the initial leaks. While our understanding of the challenges associated with radioactivity and nuclear waste has improved significantly, the fundamental problem of waste disposal remains.

Similarly in the UK, spent fuel from the early Magnox programme was stored in ponds that

are to this day open to the atmosphere. These contain spent fuel who's irradiation history is unknown and that has now corroded to the extent that the bottom of the ponds are covered in a sludge consisting of radioactive material, as well as biological matter (as a consequence of the open ponds). Retrieving and disposing of this waste is problematic due to the large number of unknowns (waste composition, radioactivity, mechanical properties) which need to be identified first, before retrieval of the waste can begin [17, 25].

Before discussing waste form design and disposal techniques for nuclear waste, it is important to understand the origin of these wastes and their connection within the nuclear fuel cycle as a whole. There is no one nuclear fuel cycle, as it is dependent on the type of reactor and fuel used, and whether reprocessing of the fuel occurs. A general outline was compiled by Wilson and is shown in figure 1.7 [35].

At the core of the (civil) nuclear fuel cycle stands the nuclear reactor. The designs for this reactor, and thus the type of fuel required and the waste produced has changed over the years. When the Windscale Pile went critical in 1950, at today's Sellafield site (then named Windscale), it was perceived that there was a desperate need for weapons grade materials in the short term, which defined the design [25, 39]. A nuclear pile is not a reactor *per se*, as the generated heat is not used in power generation, but the features which allowed for a controlled fission process in both nuclear piles and nuclear reactors are the same. The main components are summarised in table 1.2. These components are also the origin of the various types of nuclear waste, as while some of them receive a very high radiation flux (particularly the core and parts of the cladding), other parts of a nuclear plant are much less radioactive (e.g. the coolant pipeworks).

The first such British nuclear project that produced significant volumes of nuclear waste was the Windscale Pile. It also marks the beginning of the UK's independent history of nuclear technology (post-collaboration with the U.S. on the Manhattan project), and its design significantly influenced the design of the Calder Hall reactor and the Magnox reactor series [25], which featured all of the aforementioned design features outlined in table 1.2. Magnox reactors along with most currently operating reactor designs (with the exception of fast neutron reactors) rely on thermal neutrons. These neutrons have been slowed by a moderator (e.g. graphite or water) to allow them to more effectively interact with fissile nuclei and cause fission.

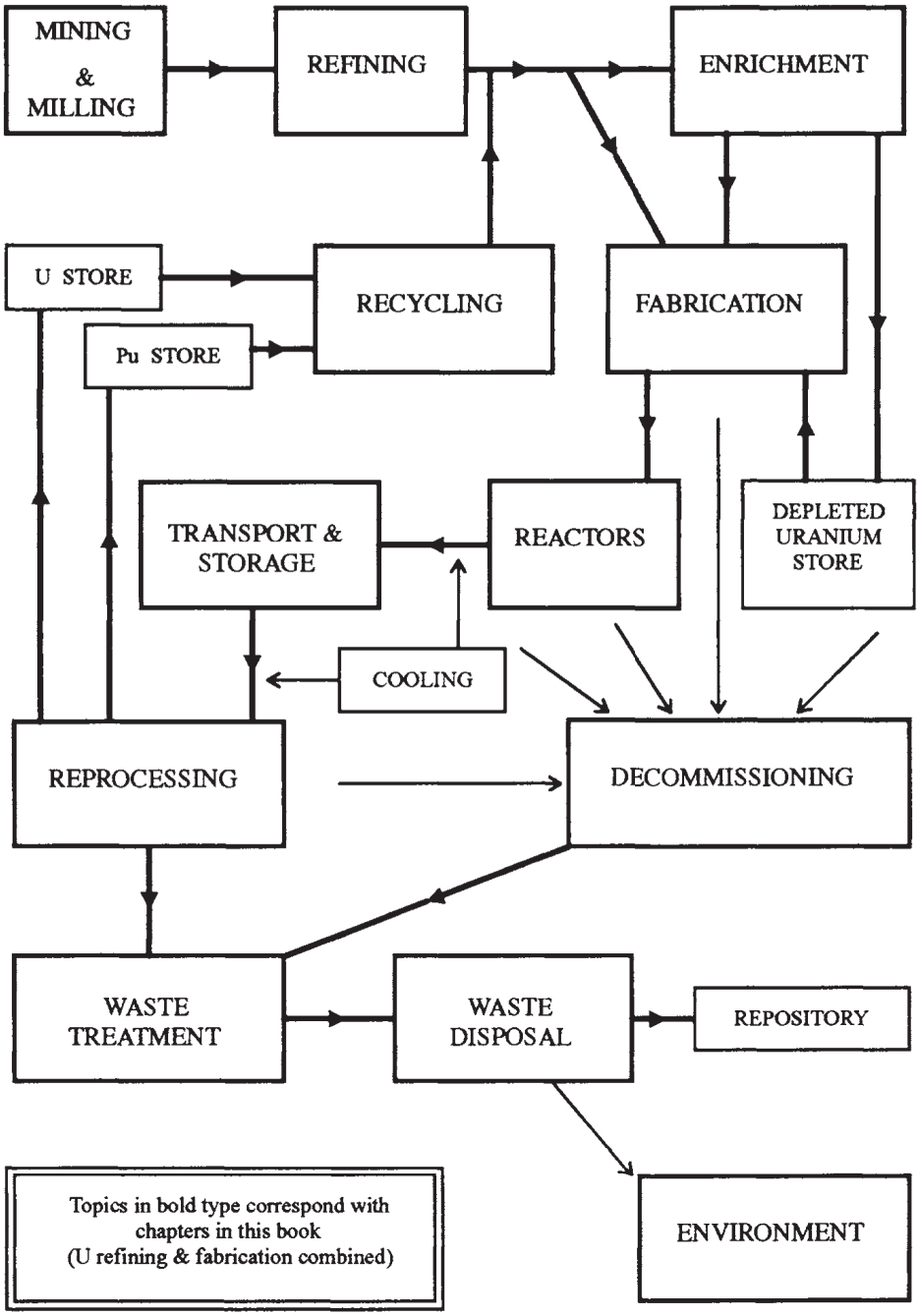

Figure 1.7 – The nuclear fuel cycle, copied from [35].

Table 1.2 – The main components of a nuclear reactor.

Component	Description
Moderator	The moderator forms the matrix within which the fuel assemblies are positioned. They are also responsible for slowing the neutrons produced by the fission reaction sufficiently that they can be captured by other fissile elements to sustain the fission reaction.
Fuel	The fuel is the reactor's source of fissile material. Two types of fuel are being used: natural uranium metal and oxide fuel enriched in the fissile isotope U^{235}. Mixed oxide fuel may also include plutonium recycled from spent nuclear fuel. Fuel assemblies typically consist of several pins containing the fuel in the form of small pellets. In addition to Uranium-based fuels, Thorium-based fuels are currently investigated for future reactor designs [40].
Cladding	The cladding is typically made up of a corrosion and heat-resistant metal with a small neutron cross-section (i.e. not likely to absorb neutrons). It is used to contain waste products produced by the nuclear reaction and thus forms a significant part of the waste stream. They typically feature fins in order to optimise the heat flow between fuel and coolant
Control rods	Control rods are mechanically operated and lowered into, or retracted from the core. They are strong neutron absorbers and are thus used to control the rate of reaction within the reactor.
Coolant	Typically a primary and a secondary cooling circuit are used. The coolant in the primary circuit (e.g. light water, heavy water, molten salt) is in direct contact with the cladding and transfers its energy to the secondary coolant (water) to generate the steam driving the turbines.

The use of uranium metal fuel in the first nuclear reactors meant that while enrichment (the process of increasing the content of the fissile isotope ^{235}U in the fuel) was not needed, very large quantities of fuel were required to achieve criticality. This led to a very large reactor core along with a low percentage of the uranium inventory actually undergoing a reaction within the reactor (usually referred to as low burn-up) and meant that the Magnox design produced large quantities of radioactive waste. When Calder Hall, the first commercial nuclear power plant, opened in 1956, no long-term storage and management plan for the resulting waste existed [25]. Nuclear waste presented a new challenge, as unlike conventional wastes, it was relatively small in volume but highly dangerous for very long periods. In the first ten years of Calder Hall's operation, 9 more sites and 23 additional reactors went onto the grid in the UK alone [25]. To deal with the waste issue in the short term, large ponds were constructed at Sellafield in which a variety of wastes, both in solid and liquid form, could be stored in a similar fashion [17, 25]. As mentioned earlier, these ponds (shown in figure 1.8) still exist today, and only in recent years have efforts begun to clean up these legacy wastes.

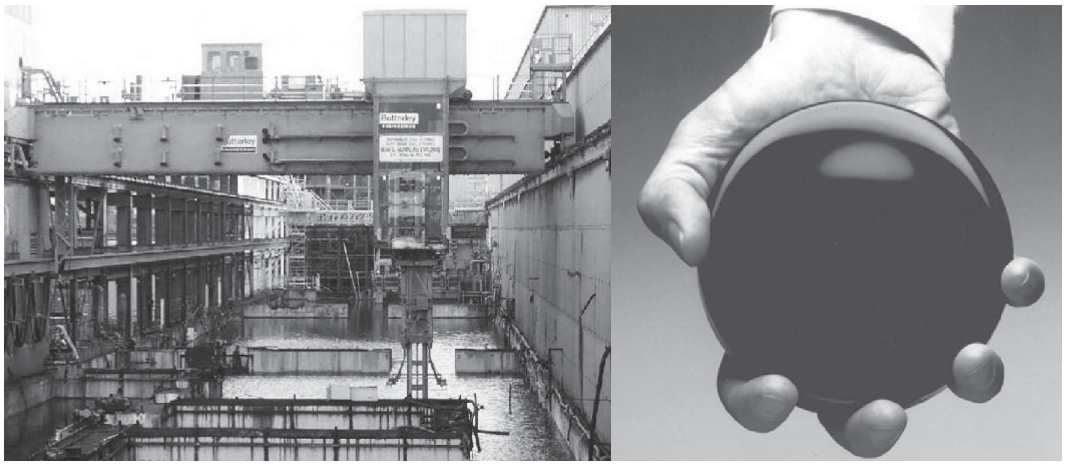

Figure 1.8 – Advances in Waste management: Disused storage pond at Sellafield (left) and a mock-up of the 80 year lifetime volume equivalent of HLW generated per person by currently operating nuclear power plants (right). Images taken from Ojovan [17].

To achieve higher operating temperatures and thus higher thermal efficiencies (the steam turbine's efficiency is limited by the Carnot cycle), in the late 1960s a new type of reactor was designed: the Advanced Gas Cooled Reactor (AGR). In addition to higher operating temperatures compared to natural uranium reactors, the AGR incorporated new materials, but required enriched fuel. The use of enriched fuel means that a smaller core (again compared to natural uranium reactors) is sufficient to reach criticality, and additionally allows higher fuel

burn-up [26]. The move towards enriched fuel and also the stainless steel cladding meant that while the quantity of waste was significantly reduced compared to the Magnox design, the resultant waste was not only of a different elemental composition, but also significantly more irradiated. The move to high burn-up fuel led to high percentage of fissile plutonium contained in the spent nuclear fuel (fuel after irradiation in the reactor). This opened up the possibility of more efficient reprocessing of the spent fuel rods from enriched uranium reactors to produce new fuel in which uranium oxide is mixed with plutonium oxide (MOX fuel) for use in light water reactors or fast reactors. The reprocessing step also alters the waste stream, as the leftover waste will no longer contain significant quantities of plutonium or uranium, so may be treated differently in disposal. While the Thermal Oxide Reprocessing Plant (THORP) was built at Sellafield specifically for that purpose, the right approach to dealing with spent nuclear fuel and plutonium is still a point of contention [27]. At this point, it is unclear whether plutonium containing spent fuel should be seen as a resource or a liability. The economic feasibility of reprocessing is largely limited by the cost of extracting uranium oxide by conventional mining, with which it has to compete.

Only a single pressurised water reactor (PWR) has been built in the UK. Sizewell B uses slightly more enriched fuel pellets compared to AGR reactors and features an even smaller core, leading to higher burn-ups compared to AGRs, although the thermal efficiency is limited by the lower operating temperatures [26]. The use of the corrosion and temperature resistant alloy Zircaloy as a cladding for the fuel was necessitated by the use of H_2O as a moderator. The use of water as a moderator was intended to provide passive safety to the design since it provides a negative void coefficient. This means that in the event of a runaway reaction, the evaporation of water would lead to a lack of moderation and thus the absence of thermal neutrons, effectively shutting down the nuclear fission reaction [26]. Unfortunately, the combination of a Zircaloy cladding and an H_2O moderator results in potential problem for both PWR and BWR designs, as the disaster at Fukushima Daiichi demonstrated, since hydrogen gas can be generated in an exothermic oxidation reaction between the zircaloy cladding and steam at temperatures exceeding 500°C. At the Fukushima BWR reactor, this led to a runaway reaction culminating in a hydrogen explosion [41].

The introduction of the PWR reactor design in the UK led to yet another different waste stream, although aside from the high zirconium content cladding, the differences were per-

Table 1.3 – Types of civil nuclear reactors built in the UK [26].

	reactor type		
	Magnox	AGR	PWR
Year*	1956	1983	1995
Reactors	26	14	1
Fuel	natural uranium (0.71 % ^{235}U)	UO_2 (3.5 % ^{235}U)	UO_2 (4.95 % ^{235}U)
Moderator	graphite	graphite	H_2O
Cladding	magnesium alloy; Magnox	20/25Nb stainless steel	Zircaloy
Coolant and pressure	CO_2 (10 bar)	CO_2 (40 bar)	CO_2 (40 bar)
Thermal efficiency	24.6 - 31.4 %	~40 %	-

* year first reactor was connected to the national grid

haps less significant as the fuel in both the PWR as well as the AGR is enriched UO_2. Details of all UK civil nuclear reactors built for power generation are summarised in table 1.3 [26].

With a greater understanding of nuclear technology and the risks involved, came more efficient generations of nuclear power plants that resulted in higher fuel burn-up, allowing and to some extent requiring ever increasing waste loading in the disposal material [18]. This has led to a decrease in the volume of HLW produced in a person's lifetime, which is now small enough to fit in the palm of a hand, as shown in figure 1.8 [17]. This not only greatly enhances waste manageability, but also reduces the volume of underground storage required and thus the cost of building a repository. With the exception of the operated by the U.S. Waste Isolation Pilot Plant (WIPP) [17, 42], only research disposal facilities are currently operated, but Sweden has applied for permission to add a deep geological repository for spent fuel at the Forsmark site, and construction of a similar facility was started at the Olkiluoto site in Finland [43].

While the amount of nuclear waste produced by reactors has been reduced as technology matured, the sheer volume of waste, as well as the large variety of different wastes make responsible disposal of nuclear waste a challenging problem.

1.5 Waste Disposal

Finding a material suitable to deal with the unwanted radioactive materials produced by nuclear reactors is challenging. Materials are required to be solid, durable, chemically stable

and suitable to incorporate the radioactive species [18]. Care must also be taken not only to consider the damaging effects of the radiation itself, but also the heating which results from the absorption of any type of radiation energy by the material. The heating is affected by the thermal properties of the waste and the surrounding layers, the intensity of radiation, and the absorbed fraction of the radiation [22]. Heating can lead to thermal expansion, thermal cracking or phase changes within the material, and intermediate storage may be required before geological disposal. This can help to mitigate the problem of excessive heating damage to the encapsulation, as ensuring sufficient heat transfer is more challenging under repository conditions without the use of active cooling concepts [22]. This is especially important in the case of glasses, which can start to devitrify (or crystallise) given enough heat [10,18].

The choice of disposal technique is an important factor which determines the suitability of a waste material. Typically more than one wasteform exists per disposal technique, such as in the case of long-term geological disposal, where the choice of wasteform will depend critically on the geological requirements, such as composition and humidity of the surrounding geology [17].

1.5.1 Liquid and Liquefied Waste

Storage of liquid or liquefied waste in storage tanks or ponds is one of the oldest "disposal" routes, but should really be considered an interim solution, as it requires constant supervision in order to continue to operate. Even within its short history, significant problems have been caused by the use of liquid storage, typically through breaches in the containment tanks.

Typically, HLW is stored as an acidic liquor that has a high concentration of fission products. It is produced by dissolving nuclear fuel rods and other highly radioactive components in nitric acid, after which a plutonium and uranium extraction step (e.g. PUREX) may be performed in a reprocessing cycle. The resultant liquid can be neutralised by the addition of sodium hydroxide [18]. The lack of stirring of this type of waste can lead to the settling of heavier elements to the bottom of the container.

Even more crude than the storage of a liquor is the submersion of radioactive material in an open pond, as was the practice in Sellafield in the 1950s and 1960s. In many of these ponds the material is completely corroded and a viscous slurry has formed at the bottoms of the

storage ponds [25]. As the ponds are open to the environment, dead animals and biological material provide an additional challenge to responsibly dealing with the waste.

1.5.2 Geological Disposal

Most countries with an established nuclear industry including the UK, are now aiming to build geological repositories for their ILW and HLW [17, 27]. Geological disposal involves the confinement of ILW and HLW wastes in large underground repositories with the aim of permanent, or at least long-term storage of radioactive wastes. The waste will be stored until such a time as it is either rendered harmless or, in the case of an open repository, until superior processing technology exists. As the development of such technology may require a long time, over which the safety of the waste and stability of the political system cannot be guaranteed, even open repositories are to be built at depths of over 500 m and are based on a multi-barrier concept [18]. In the multi-barrier concept, the waste form (e.g. a vitrified glass or a ceramic), is encapsulated inside a sealed metal canister (typically stainless steel) [27]. Several additional layers exist, depending on the geology of the repository and the requirements of the waste (e.g. in regard to pH), to prevent any leaking of radionuclides to the environment or degradation of the waste material [43].

1.5.3 Borehole Disposal

In borehole disposal, a deep hole of several kilometres is drilled into the ground, in which the waste is stored vertically (usually in drums). The upper 2 to 3 km of the borehole are then backfilled with concrete or a similar filler material to plug the hole. While research is being carried out in this field, so far no country has opted for this disposal option [44].

1.5.4 Other Disposal Routes

More exotic disposal routes, such as the storage of waste at the bottom of the ocean or a launch of HLW into space have been proposed, but little research has been done in these areas due to economic feasibility, the involved risks and challenges, particularly when the large volumes of waste are concerned [44].

1.6 Common wasteforms

Following is a brief overview of the commonly used materials in the disposal of nuclear waste. As each disposal form has different characteristics, as well as strengths and weaknesses, it is important to choose the right material and optimise it for the specific waste stream that is to be disposed of.

Ceramics

Ceramic wasteforms typically rely on the substitution of cations by similarly sized radionuclides into a crystalline host material. The most widely used example is the Australian Synroc ceramic [45], which includes a number of phases comprising zirconolite, a hollandite-like phase, perovskite, and titanium oxides, and more, which can achieve a typical HLW waste loading of about 20 % [22]. The major advantage of Synroc ceramics is that the composition of the component phases can be altered to suit the waste stream. Its excellent thermal properties mean that interim storage is not strictly required in some cases. That is, it can be placed in a repository whilst still being highly heat-generating [17]. It is very durable, even at elevated temperatures of 300°C and in a humid environment and is very well suited to the disposal of plutonium stockpiles, as it can contain up to 50 % Pu by mass [18]. Whilst not yet employed industrially in the immobilisation of HLW, ceramic waste forms are a competitive option for the disposal of HLW, although they are more specific to the range of elements to be immobilised [18].

Cements

Cements are mainly used in the encapsulation of LLW and some ILW [22], as they are cheap to make and easy to process. Cements are however subject to radiolysis (the breaking of bonds by radiation), making them unsuitable for HLW [18]. Typical waste loadings are of the order of 15 - 25 %, with leach rates comparable to those observed in borosilicate glass [22].

Glasses

The first materials proposed as nuclear waste hosts and still the most widely employed are those based on borosilicate glass compositions. They have become established primarily because of their low cost and established manufacturing practices, but also the amorphous nature of the material [22]. Most of the radioactive waste exists in liquid form (i.e. the solid waste has been dissolved in acid), so that the liquid waste streams can be pumped and thus more easily processed [24]. This benefits glasses, as the liquid waste can be added either directly to the melt, or after calcination into a powder. The liquid nature of the glass melt means that the radioactive material will hopefully be spread relatively evenly in the waste form. The earliest of these glasses was based on nepheline syenite, a type of igneous rock, and used to vitrify waste at Chalk River in Canada [22]. Whilst other waste forms were also investigated, borosilicate glass was chosen as the principal waste form for highly radioactive wastes in several countries including the UK, the US and France [22].

The vitrification of HLW in borosilicate glasses is attractive, owing to the glass's ability to immobilise a wide compositional range of waste at high waste loadings and low cost. Immobilisation is distinct from other storage options, such as encapsulation in concrete, in that the majority of constituent elements are in solid solution with the glass matrix and not just merely held in a container material. Other materials for the immobilisation of HLW exist (such as ceramics), but most tend to have a narrower compositional range of waste that can be accommodated [22].

The waste host material used in the UK is a borosilicate glass of composition given in table 1.4. The waste and glass frit are mixed and processed in induction furnaces at the Windscale Vitrification Plant for subsequent storage in stainless steel cans [24]. The low processing temperatures avoid volatilisation of radioactive isotopes, but also increase the chances of incomplete dissolution of certain waste phases and elements within the glass. The structure of these glasses will be discussed at a later stage, when validating the simulation results (see section 3.1). Unfortunately, the variability in the waste stream composition and process limitations mean that the presence of insoluble crystalline phases within the glass melt cannot be avoided. The basic principle of these interfaces was investigated in a previous work by Rushton [46], where a deviation from the bulk distribution of alkali network modifiers is de-

scribed close to specific interfaces. As the effect of alkali species is examined further in this report, it becomes clear that a better understanding of these interfaces might lead to improved diffusion control of highly mobile species, such as ruthenium and caesium, which are part of the long-lived radioactive elements that occur in the waste-stream.

Table 1.4 – Major components of the UK's Magnox waste glass composition [47].

Composition / wt.%					
SiO_2	B_2O_3	Na_2O	Al_2O_3	CaO	ZrO_2
55.3 %	11.3 %	11.3 %	3.4 %	5 %	1.6 %

Another crucial factor in the long-term safety of nuclear waste glasses is the corrosion resistance of the glass. While glasses are often assumed to be resistant to corrosion, the long-term stability of glasses in extreme environments can be problematic, particularly in the presence of water or humidity [48]. The main aim of this work is the development of models suitable to accurately describe and investigate these glasses and to improve their performance as waste hosts. This will involve investigating alternate compositions, in particular the addition of zinc oxide (ZnO) to glass compositions. The durability and the mobility of alkali species will be of particular interest, as many of the incorporated radioactive elements are alkaline and the glass itself will potentially need to withstand corrosion for thousands of years.

Glass composite materials

In addition to solely relying on the chemical incorporation of radionuclides into a glass, it is also possible to use glass crystal composite materials (GCMs) in which the glass is further used to physically encapsulate embedded crystalline particles [49]. GCMs are considered as potential wasteforms for particularly hazardous isotopes that have been separated from other waste materials (e.g. ^{129}I separated from SNF) [50]. For example, $La_2Zr_2O_7$ pyrochlore crystals can be encapsulated in a hot pressed lead silicate glass matrix to immobilize actinides [51]. These elements would otherwise be difficult to deal with, due to their tendency to phase segregate from conventional glasses. Another major advantage of GCMs is that they tend to offer low processing temperatures (below 1000 K) [49].

The use of non-silicate glass systems is possible with this type of material, which can make it

easier to dispose of other problematic elements such as halogens, which have low solubility in conventional nuclear waste glass compositions in addition to being highly volatile at the processing temperatures required for these glasses [52]. To deal with this type of waste, a sodium aluminium phosphate (NaAlP) glass-ceramic composite has been proposed by Michie *et al.* [53] which has similar mechanical properties to borosilicate glass, but can be processed at lower temperature and more readily incorporates halide-containing waste.

Glass-ceramics

Glass-ceramics are similar to GCMs, in that they contain both a crystalline and amorphous phase. Glass-ceramics are derived from a base glass in a separate heat treatment phase, which causes small, randomly oriented crystallites to nucleate heterogeneously within the glass matrix due to the addition of nucleating agents (such as TiO_2). This leads to an isotropic material with well-controlled mechanical properties, making it an attractive choice for use in nuclear waste disposal. First developed in the 1950s by Stookey at Corning Glass Works [18], they often have exceptionally low coefficients of thermal expansion. This led to their use as substrate for space telescopes and domestic cooking surfaces [10]. They also have high melting points compared to normal glasses, and their already part-crystalline nature makes devitrification less of an issue.

In an effective wasteform, the durability of the least durable component poses the limiting factor [18]. Glass-ceramic waste forms such as $CaTiSiO_5$ titanite in an aluminosilicate matrix have been developed, particularly in Canada and Germany [22]. The combination of two different materials, means it can incorporate smaller cations, actinides and other fission products by substitution of calcium and large cations such as caesium by immobilisation in the glass phase.

While glass-ceramics have yet to be implemented as an actual wasteform, the process may rely on facilities and techniques already used in the vitrification of borosilicate glasses, making them potentially attractive in the future [18].

1.7 Glasses in Electronic Devices

The use of glass as an advanced engineering material is not limited to nuclear waste. In fact, the same principles of understanding and engineering the network structure of glasses can also be applied in other fields. Instead of trying to inhibit the movement of ions through the glass, as is the case in nuclear waste for example, it may be desirable to actively promote fast ionic transport of alkali species for uses in lithium ion batteries or electrochromic devices.

Glass has a number of attractive properties for uses in electrochemical devices. Firstly, it is often transparent, which is very often a requirement, especially in electrochromic devices. Secondly, it is usually easy and cheap to produce and mold glasses into a variety of shapes. Even thin films of less than 100 µm thickness are possible, and allow for roll-to-roll processing of glasses. Thirdly, glasses have superior durability and mechanical stability compared to most polymers and can operate at high temperatures or in oxidising conditions.

1.7.1 Electrochromic Devices

An electrochromic device is one which can alter its colour through the migration of ions after a charge has been applied. For example, the glass pane separating the passengers and the driver in the latest German ICE trains can be switched between opaque and transparent, as shown in figure 1.9 [11]. In order to achieve this effect, three different materials are layered between conductive layers (indium tin oxide (ITO) is commonly used for its transparency combined with electric conductivity):

Ion storage material

The ion storage material is similar to the materials used in lithium ion batteries, with the added requirement of having to be transparent. The purpose of this material is to store the ions (usually Li) in the “off” state.

Electrolyte

The transparent electrolyte is needed to provide a conduit for the ions to flow through. As these devices are transparent, it is also important to match material properties such as thermal

expansion coefficients and refractive indices with the ion storage material as well as the electrochromic layer.

Electrochromic layer

This layer is where the chemical reaction in the "on" state and takes place, starting as soon as a voltage is applied. The most commonly used material for this purpose is WO_3 prepared as a transparent thin film, which under an applied voltage can react with lithium to form a compound of deep blue colour [11]:

$$WO_3 + x\,(Li^+ + e^-) \longrightarrow Li_xW_{(1-x)}W_xO_5$$

The change in colour is prompted by a change in the oxidation state from W^{VI} to W^V. This gradual colour and transparency change is shown in figure 1.9.

Figure 1.9 – An electrochromic window slowly changes colour when a voltage is applied, as a chemical reaction in the WO_3 containing electrochromic layer progresses. Image taken from [11].

Glasses may be useful in these devices, as they could be used as an ion conducting electrolyte that is transparent, provides mechanical stability even in a thin film and is inert with respect to both the electrochromic material, as well as the ion storage material.

1.7.2 Lithium Ion Batteries

Due to the very small atomic mass of Li^+, lithium based materials are very attractive both in terms of gravimetric storage density (low mass per volume), as well as volumetric energy density (high charge per volume). Lithium ion batteries rely on the transfer of charge from an anode material (e.g. graphite) to a cathode material (e.g. $LiCoO_2$), via a conductive electrolyte which separates the two.

A common problem with these devices however is the high reactivity of Li^+ ions, which can lead to unwanted reactions between the electrolyte (usually a liquid organic electrolyte combined with a fabric separator layer) and the electrodes. Over continued charge/discharge cycles, this leads to a loss in storage capacity of the battery, as the resistance to ionic conduction increases as a result of the chemical reactions.

Glasses could potentially be used to circumvent this problem of degrading performance, by either replacing the electrolyte and separator altogether, or being used as a thin-film electrode coating which prevents degradation by providing a passive layer [20].

1.7.3 The $LiF.AlF_3$ system

The $LiF.AlF_3$ system has been proposed as an ionic conductor of lithium and a surface coating in Li-ion materials [20,21,54]. Pioneering work on a material of this composition was carried out by Oi and Miyauchi in the 1980s [54–56], investigating the use of $LiF.AlF_3$ glasses in electrochromic devices. They postulated, that the preparation of a thin film from the gaseous phase could lead to amorphous structures that would otherwise be unattainable.

In their work, they prepared a $LiF.AlF_3$ thin film by vapour deposition of LiF and AlF_3, which exhibited ionic conductivities in excess of those of LiF or AlF_3 by themselves. For a film of 0.8 µm thickness, they measured a conductivity of 10^{-4} S m^{-1} at room temperature. Highest conductivities were achieved experimentally when the LiF to AlF_3 ratio was close to 50 %. The resulting structure was found to be amorphous, containing AlF_3 octahedra, in which a central Al^{3+} ion is coordinated by six F^-. Lithium cations provide the necessary charge balance. The material was patented in 1983 [56] for use as an ionic conductor or within electrochromic displays. More recently, the material has been investigated as a potential surface coating on lithium ion battery electrodes [20]. No theoretical research on this material has been carried out thus far, making this an intriguing material to study using the method of molecular dynamics (MD) technique, discussed in more detail later in this thesis.

2 Methodology

This chapter will provide an overview of the simulation and analytical techniques that form the basis of this thesis. An overview of the unique challenges involved in modelling glasses will be presented, after which the different steps of the simulation will be described in order. Where appropriate, details of how these techniques were applied to obtain the results presented in later chapters are given.

2.1 Theory of Glass Simulation

When a mixture of certain molten oxides is cooled sufficiently quickly, a metastable glass phase can be formed [9]. This is the usual way in which most commercial glasses are produced from their component oxides and requires a cooling rate in the order of tens of degrees per minute, depending on the glass and its current temperature and surroundings. Even this relatively fast cooling process poses a significant problem for the time scales accessible with computer simulation techniques and current computer performance, due to the large number of possible interactions between atoms.

2.1.1 Molecular Dynamics - A Classical Approach

Principally, there are two different approaches to modelling materials. The traditional Newtonian (or classical) mechanics approach, describes the movement of bodies influenced by a system of forces. In the special case of classical atomistic simulations, this translates to atoms being subjected to a number of forces. Atoms are treated as point charges that are under the influence of a system of forces. The other option is a quantum-mechanical based method, such as the commonly used density functional theory (DFT) [57], where electrons are not simple point charges but are rather treated as an electron cloud. The size of such quantum-mechanically modelled systems however, is limited by current computing technology to tens or hundreds of atoms, and therefore currently not suitable for glasses, whose amorphous structure can not be adequately expressed within such a small system.

The molecular dynamics (MD) method [58] is a classical modelling technique used as the principal method of investigation to simulate a variety of different glass compositions over

a range of temperatures. It is also used to simulate ionic diffusion, as well as the effects of radiation damage on glasses using primary knock-on atoms (PKA) [59] to initiate a cascade of collision events.

MD is used in this work to derive glass structures from a high-temperature melt. Whilst MD is a very efficient technique that allows for the study of much larger systems than *ab initio* techniques [60], it can still only emulate real systems. For example, the speed at which a simulated glass melt has to be quenched usually exceeds real-world cooling rates, which can be as low as $0.1\,\mathrm{K\,s^{-1}}$ [16], often by several orders of magnitude [61]. As will be elucidated in the following chapters, model glasses which closely resemble experimental observations can nevertheless be obtained by a simulated melt-quench procedure. The typical procedure used to obtain model glass structures consists of five distinct steps:

I. Determining Interatomic Potentials Potentials are a mathematical construct describing the van der Waals [62], covalent and electrostatic interactions between the different ions, which can be derived by fitting to a set of material parameters (e.g. unit cell volumes of crystal phases, density, etc.) derived empirically from experimental data or from other simulations (e.g. DFT [57]). This step is often unnecessary if suitable potentials already exist or can be easily adapted to suit the system to be studied.

II. Set-up of Simulation A simulation box of the correct shape to match the experimental material density at room temperature is randomly filled with ions of the required composition for use with the MD code.

III. The Melt The system is heated well into the liquid regime, which randomises the distribution of ions. The initial atomic configuration is often chosen at random (see previous step). The high initial temperatures also tend to remove any bias inherent in the starting configuration.

IV. The Quench The glass phase is induced by rapidly cooling from the melt over a very short period of time (several orders of magnitude faster than real world melts).

V. Equilibration and Data Collection The system is allowed to equilibrate at a set temperature, which allows the atoms to assume local energy minima at the given temperature, so that data can be collected.

2.2 The Born Interpretation of Interionic Forces

In order to obtain meaningful results, the MD algorithm (see section 2.7), requires a reliable and accurate description of inter-atomic forces. Thus, the origin and underlying principles of these potentials need to be discussed.

The simplest ionic systems can be described by assuming an ionic Born crystal lattice [63]. In this model, all atoms are treated as point charges in a three-dimensional lattice. All of these point charges can interact with each other, giving rise to the total lattice energy $E_{lattice}$, or the energy to separate all the ions in the system to infinite distance. This energy can be described by the summation of all interactions between the total number of ions:

$$E_{lattice} = \sum_{i=1}^{N} \phi_i + \frac{1}{2} \sum_{i=1}^{N-1} \sum_{j>i}^{N} \phi_{ij} + \frac{1}{6} \sum_{i=1}^{N-2} \sum_{j>i}^{N-1} \sum_{k>j}^{N} \phi_{ijk} + ... \tag{1}$$

In order, these terms describe the zero energy of the ions ϕ_i, the interactions of two ions ϕ_{ij}, the interactions over three ions ϕ_{ijk} and so forth. Higher order interactions involving three or more ions are relevant in cases where large, polarisable ions negate charge transfer and covalent bonding occurs. A factor of $1/2$ and $1/6$ has to be applied, so that each interaction is only counted once. In an ionic lattice higher order interactions are usually negligible due to the close proximity of the electrons to the bonding cation. It can thus be assumed that for the short range contribution, only two-body interactions need to be considered. Some glass compositions contain small cations with high charge (e.g. Si^{4+}), which can experience significant covalent character, where it is not possible to localise charges to a point. Ideally, quantum mechanical methods would be used, but this is not feasible, as the lack of long-range order means that the simulation cell must be relatively large to give a statistically significant structure, meaning that simulation run times become impractical, where each time step may take several minutes to complete.

Generally, the inter-ionic interactions can be split into two components: the electrostatic (also known as Coulombic) interactions that dominate at long range and a short-range component.

The short-range interaction takes account of both the nuclear repulsion arising as a consequence of the Pauli exclusion principle [64], as well as van der Waals forces. Together, they give the total force acting upon each atom in a two-body description of the system:

$$\phi_{total}\left(r_{ij}\right) = \phi_{coul}\left(r_{ij}\right) + \phi_{short}\left(r_{ij}\right) \tag{2}$$

This force can be used in a MD code (such as DL_POLY_3 [65]) to predict the acceleration of atoms and thus the velocity and distance moved during each incremental timestep.

2.3 Long-range Interactions

Long-range interactions are dominated by electrostatic interactions between all ion pairs, and described by Coulomb's law [66] (see equation 3),

$$\phi_{Coulomb}(r_{ij}) = \frac{q_i q_j}{4\pi\varepsilon_0 r_{ij}^2} \tag{3}$$

where q_i and q_j are the ionic charges of ions i and j, separated by a distance r_{ij} and ε_0 is the permittivity of free space. By summing equation 3 for all ion pairs, their total energy contribution can be found for any size of system. Due to the periodicity in the charge distribution, this sum is conditionally convergent, meaning that the sum of charges of a spherical volume oscillates, depending on the chosen electrostatic cutoff. This problem is illustrated in figure 2.1, where the sum of charges is shown to fluctuate dependent on the area (or volume) encompassed by the cutoff.

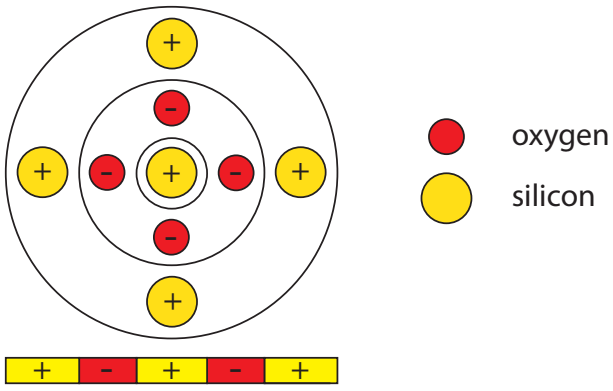

Figure 2.1 – Changes in the sum of charges, as observed for various circular cutoffs.

Solving long range interactions directly is computationally expensive, as they converge slowly with separation and need to be solved for all pairs in the system. The number of operations required scales with $O(N^2)$, where N denotes the number of atoms in the system, making very large systems without a more efficient computational mechanism unfeasible [60].

In order to allow rapid and guaranteed convergence of equation 3, the Ewald summation [67] can be employed. The Ewald technique [67] is able to incorporate periodic boundary conditions and will increase the computational efficiency to $O(N)$, by decomposing interactions into real space and reciprocal space parts, each of which sum quickly and with guaranteed convergence. The use of periodic boundary conditions employed in the simulations leads to long-range periodicity of the simulation cell. This periodicity, can be accurately described in reciprocal space by a Fourier transform. This avoids the use of a simple and less accurate truncation of the long-range interactions. For a detailed explanation of the Ewald technique, see the introductory text by Rapaport [60].

In this work, the smooth particle mesh Ewald sum (as implemented in DL_POLY_3 [65]) was used to calculate the electrostatic contribution to the calculations presented here [68, 69]. This is a modification of the original Ewald sum [67] that employs fast Fourier transforms to improve computational efficiency.

2.4 Short-range Interactions

As mentioned previously, short-range interactions are used to describe nuclear repulsion, as well as van der Waals, electron-electron and covalent forces. Some common representations of short range interaction forces $\phi_{short}(r_{ij})$ are listed below :

Lennard-Jones (simplified form) [70, 71]:

$$\phi_{short}(r_{ij}) = \frac{A_{ij}}{r_{ij}^{12}} - \frac{B_{ij}}{r_{ij}} \tag{4}$$

Buckingham [72]:

$$\phi_{short}(r_{ij}) = A_{ij} \exp\left(\frac{-r_{ij}}{\rho_{ij}}\right) - \frac{C_{ij}}{r_{ij}^{6}} \tag{5}$$

Born-Mayer-Huggins [73–75]:

$$\phi_{short}(r_{ij}) = A_{ij} \exp\left(-B_{ij}(\sigma_{ij} - r_{ij})\right) - \frac{C_{ij}}{r_{ij}^6} - \frac{D_{ij}}{r_{ij}^8} \tag{6}$$

Morse [76]:

$$\phi(r_{ij}) = D_{ij} \exp\left(-2\alpha_{ij}(r_{ij} - r_0)\right) - 2D_{ij} \exp\left(-\alpha_{ij}(r_{ij} - r_0)\right) \tag{7}$$

Pedone [77]:

$$\phi_{short}(r_{ij}) = D_{ij}\left[\left\{1 - \exp\left(-a_{ij} \cdot (r_{ij} - r_0)\right)\right\}^2 - 1\right] + \frac{C_{ij}}{r_{ij}^{12}} \tag{8}$$

All of these potentials try to represent the Pauli repulsion and the van der Waals forces as seperate terms as a function of the distance r between two ions. In the Lennard-Jones potential [70, 71](equation (4)) for example, the r_{ij}^{-6} distance term describes the attractive van der Waals forces of polarisable atoms. As the separation distance between the two atoms decreases, the electron clouds will start to overlap, leading to strong repulsion. This repulsion is the basis for the r_{ij}^{-12} term, whose high exponent makes the potential very steep and so this term only dominates the interaction at very short distances. The Lennard-Jones potential (equation (4)) in its simplified form has two interaction specific parameters: A_{ij} and B_{ij}, making it computationally efficient.

2.4.1 Buckingham Potentials

The Buckingham potential [72] (equation (5)), which is used in this work as both a reference in silicate glasses and to model ionic glasses of the lithium aluminium flouride system, is a refinement of the Lennard-Jones potential [70, 71] (equation (4)) and has A_{ij}, ρ_{ij} and C_{ij} as parameters specific to a pair of interacting ions (e.g. $\mathrm{i} = O^{2-}$ and $\mathrm{j} = Si^{4+}$). An advantage of the Buckingham potential [72] over the Lennard-Jones potential [70, 71] is the more realistic exponential function to model the exchange repulsion originating from the Pauli exclusion principle [64]. In cases of highly ionic interactions, the C_{ij}-term is negligible and set to 0, which further enhances computational efficiency. A major disadvantage of the Buckingham potential however, occurs in high energy simulations, such as modelling the nuclear-nuclear interaction, where the absolute value of r_{ij}^{-6} term becomes larger than the exponential Pauli repulsion term. This leads to the so called "Buckingham Catastrophe" [60], where atoms are

predicted to attract, rather than repel each other at very short distances (as seen in figure 2.2). The typical solution to this problem is the use of an additional repulsive potential in high energy mo

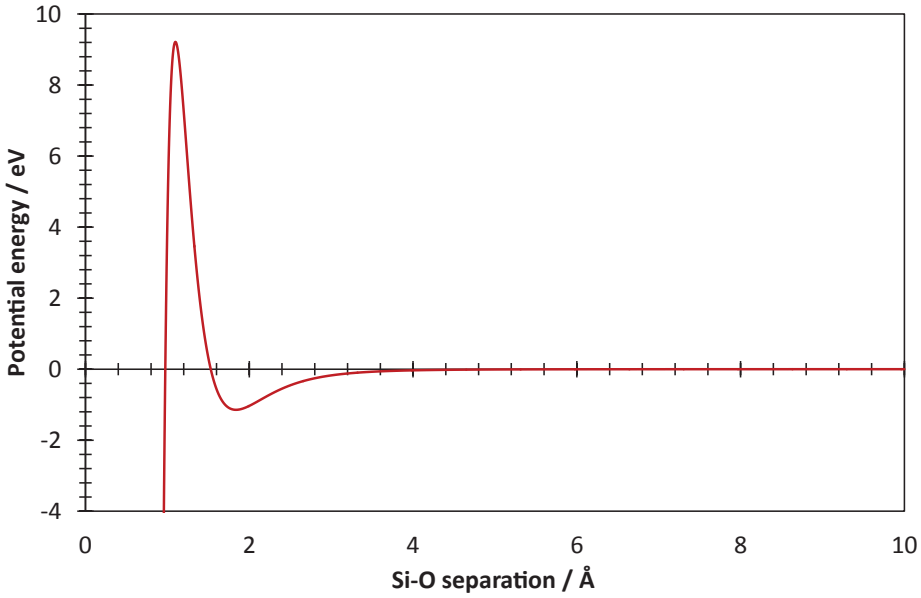

Figure 2.2 – Buckingham contribution in BKS Si-O potential.

One set of potentials specific to glasses, which is used in this work was developed by Kramer *et al.*, and they are frequently termed the Beest-Kramer-Santen (BKS) potentials [78]. They are based on the Buckingham potential (equation (5)) and have been used in several studies of silicate glasses and produce good matches to experimental data for silica glass. The BKS potential was compared to the more sodium glass specific Teter potentials, as published by Cormack *et al.* [79]. Both potentials follow the Buckingham form for two-body interactions [72] and use partial charges instead of full ionic charges. This allows more accurate modelling of the bonding behaviour in glasses, which is of mostly covalent character [77]. The full list of potential parameters used is given in tables 2.1 and 2.2 for BKS and Teter potentials respectively.

2.4.2 Pedone Potentials

The Pedone potential (equation (8)) [77] is based on the Morse potential function (equation (7)), but is designed to model oxides, silicates and silica-based glasses. The Morse potential on the other hand, was designed to deal with diatomic molecules and a long-range coulomb term is therefore not added in the total potential. Further, the Pedone potential loses

the physical meaning of the variables D_{ij}, a_{ij} and r_0, which in the Morse potential represent the bond dissociation energy, the width of the energy well and the equilibrium bond distance respectively. Instead, as the Coulomb term is explicitly included in the Pedone variant, they are treated as parameters, with the addition of a repulsive C_{ij} term to model the repulsive interactions at high temperature and pressure [77]. The Pedone potential was used in this work in the modelling of silicate glasses. The relevant parameters for the Pedone potential are listed in table 2.3.

2.5 Repulsive Potentials for High-Energy Models

The overlapping of electron clouds that occurs at close atomic separations leads to a very strong repulsive force. This force is often inadequately modelled in short-range potentials, such as the Buckingham potential. To circumvent the problem, an additional repulsive potential is often introduced and combined with the short-range potential to obtain a new potential. This additional potential has little influence on the equilibrium interactions at most temperatures, but is necessary in cases of very high energies in the simulation, such as at unphysically high temperatures (melt-quench procedure) or during radiation damage modelling.

2.5.1 The ZBL Potential

The most common form of nuclear repulsion potentials is that of Ziegler-Biersack-Littmark (ZBL) (see figure 2.3) [80]. The potential is based on the strong positive-positive repulsion that dominates when atomic nuclei are brought into close proximity with each other. This is the same potential employed in TRIM/SRIM calculations (see section 2.8.1), and is given below:

Table 2.1 – BKS short-range potential parameters.

Pair	A_{ij} / eV	ρ_{ij} / $\AA^{-1}$	C_{ij} / $(eV/\AA^{-6})$	Reference
$Si^{2.4+}$-$Si^{2.4+}$	0*	1*	0*	-
$Si^{2.4+}$-$O^{1.2-}$	18003.7572	0.205205	133.5381	[78]
$Si^{2.4+}$-$Na^{0.6+}$	0*	1*	0*	-
$O^{1.2-}$-$O^{1.2-}$	1388.7730	0.362319	$175.\bar{0}$	[78]
$O^{1.2-}$-$Na^{0.6+}$	3542.2072	0.241864	$0.\bar{0}$	[78]
$Na^{0.6+}$-$Na^{0.6+}$	0*	1*	0*	-

*These parameters effectively set the potential to 0, but allow for later addition of a nuclear repulsion term.

$$\phi_{ZBL}(r_{ij}) = \frac{1}{4\pi\varepsilon_0}\frac{z_i z_j e^2}{r}\varphi\left(r/a\right) \tag{9}$$

where z_i and z_j are the atomic numbers of interacting elements i and j, ε_0 is the permittivity of free space, e is the charge of an electron and $\varphi\left(r/a\right)$ is a screening function that tends to unity as r tends to zero. The screening function φ depends on the screening parameter a:

$$\varphi\left(r/a\right) = 0.1818\exp\left(-3.2r\right) + 0.5099\exp\left(-0.9423r\right) \tag{10}$$

$$+0.2802\exp\left(-0.4029r\right) + 0.02817\exp\left(-0.2016r\right)$$

$$a = \frac{0.8854a_0}{z_i^{0.23} + z_j^{0.23}} \tag{11}$$

In this work, the ZBL potential [80] was added to Buckingham interactions [72] with a non-zero C-term, as it prevents a Buckingham catastrophe [60], particularly in radiation damage cascades where individual ions are given enough energy to overcome the potential barrier of the Buckingham potential.

2.5.2 Splining Multiple Potentials

In order to be able to use the ZBL potential, it needs to be combined with the short-range interaction in such a way that no discontinuity or step arises in the overall potential, as this would lead to problems at the simulation stage. Simple addition of the potentials is not possible, as this would increase the energy of the potential. Instead, the potentials can be linked by

Table 2.2 – Teter short-range potential parameters.

pair	A_{ij} /eV	ρ_{ij} /$\mathring{A}^{-1}$	C_{ij} /$(eV/\mathring{A}^{-6})$	reference
$Si^{2.4+}$-$Si^{2.4+}$	0*	1*	0*	-
$Si^{2.4+}$-$O^{1.2-}$	13702.905	0.193817	54.681	[79]
$Si^{2.4+}$-$Na^{0.6+}$	0*	1*	0*	-
$O^{1.2-}$-$O^{1.2-}$	1844.7458	0.343645	192.58	[79]
$O^{1.2-}$-$Na^{0.6+}$	4383.7555	0.243838	30.700	[79]
$Na^{0.6+}$-$Na^{0.6+}$	0*	1*	0*	-

*These parameters effectively set the potential to 0, but allow for later addition of a nuclear repulsion term.

Table 2.3 – Pedone short-range potential parameters.

pair	D_{ij} / eV	α_{ij} / $\AA^{-2}$	r_0 / $\AA$	C_{ij} / $eV\ \AA^{12}$	reference
$Si^{2.4+}$-$Si^{2.4+}$	-	-	-	-	-
$Si^{2.4+}$-$O^{1.2-}$	0.340554	2.006700	2.100000	$1.\overline{0}$	[77]
$Si^{2.4+}$-$Na^{0.6+}$	-	-	-	-	-
$Si^{2.4+}$-$Li^{0.6+}$	-	-	-	-	-
$O^{1.2-}$-$O^{1.2-}$	0.042395	1.379316	3.618701	$22.\overline{0}$	[77]
$O^{1.2-}$-$Na^{0.6+}$	0.023363	1.763867	3.006315	$5.\overline{0}$	[77]
$O^{1.2-}$-$Li^{0.6+}$	0.001114	3.429506	2.681360	$1.\overline{0}$	[77]
$Na^{0.6+}$-$Na^{0.6+}$	-	-	-	-	-
$Na^{0.6+}$-$Li^{0.6+}$	-	-	-	-	-
$Li^{0.6+}$-$Li^{0.6+}$	-	-	-	-	-

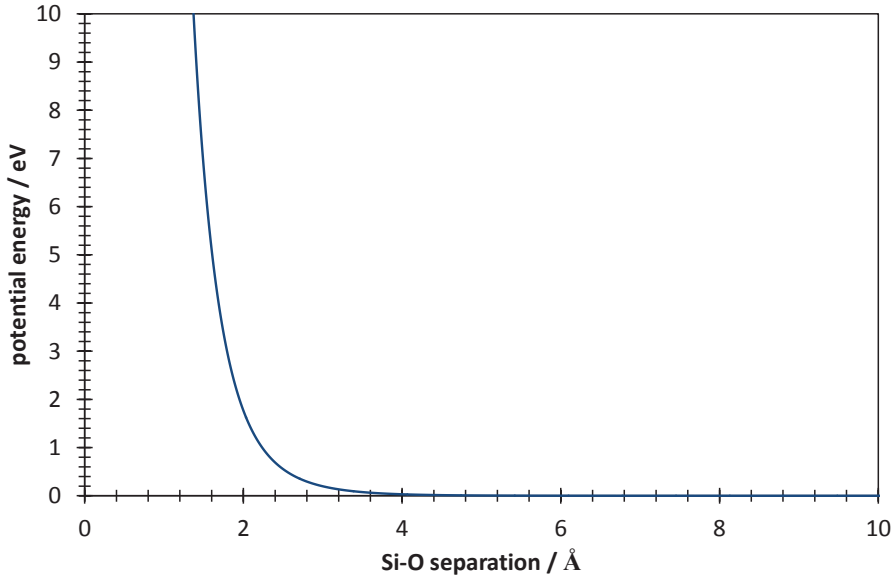

Figure 2.3 – ZBL potential for Si-O showing a steep wall in the potential at small separation.

a so called spline function, which serves to link two distinct potentials, each operating over a distinct range of separation. A stepless transition from one potential (e.g. the ZBL potential) to the next (e.g. Buckingham) is ensured by an exponential spline of the form

$$\phi_{spline}\left(r_{ij}\right) = \exp\left(\alpha + \beta r_{ij} + \gamma r_{ij}^2 + \delta r_{ij}^3 + \epsilon r_{ij}^4 + \varepsilon r_{ij}^5\right) \tag{12}$$

where the parameters $\alpha, \beta, \gamma, \delta, \epsilon$and ε are chosen such that at the start and end points x and y of the spline function, the following expression holds true:

$$\phi_{spline}\left(x\right) = \phi_{ZBL}\left(x\right) \text{ and } \phi_{spline}\left(y\right) = \phi_{short}\left(y\right) .$$

To further enhance smoothness, the first and second differentials of the slope at the start and end point of the spline potential should match those of the potential starting and ending at that point. The final functional form for a potential incorporation both a ZBL potential and a short range potential is thus given by:

$$\phi_{total}\left(r_{ij}\right) = \phi_{Coulomb}\left(r_{ij}\right) + \begin{cases} \phi_{ZBL}\left(r_{ij}\right), & r_{ij} < x \\ \phi_{spline}\left(r_{ij}\right), & x \leq r_{ij} < y \\ \phi_{short}\left(r_{ij}\right), & r_{ij} \geq y \end{cases} \tag{13}$$

2.6 Potential Parameter Derivation

Suitable potentials for the materials under investigation do not always exist or need to be adapted from a different system. In either case, it is possible to derive new sets of pair potentials from known crystal phases. In this work, static energy minimisation of crystalline phases was the tool of choice to derive the required potentials.

2.6.1 Energy Minimisation using GULP

The General Utility Lattice Program (GULP) [81] is a programme that can calculate the static crystal lattice energies, $U_{lattice}$, of crystal structures by a summation of the potential energies of all atoms. It can then minimise this energy by relaxing atomic positions under the influence

of a potential field (hence it is an example of a static lattice method). This requires it to have similar inputs to a MD simulation, the most important input being a suitable potential [81]. Where such a potential does not exist however, GULP can also fit a set of free parameters in a potential to a number of observables (such as unit cell dimensions, bulk moduli, etc.), which have usually been established experimentally.

Static lattice fitting was used extensively in this work to establish a set of potentials for use with the Aluminium-Lithium-Fluorine system. This was achieved by numerically solving equation 1, using the same Buckingham potentials (including an Ewald summation) that were later to be used in the molecular dynamics simulations. GULP was used to derive potentials for the $LiAlF_4$ glass system, by fitting several Buckingham potential pairs to the potential energy surface of several crystal structures. The investigated crystal structures were Li_3AlF_6, AlF_3 and LiF, with structural information acquired from the chemical database service [82–86]. First estimates for the potentials were obtained by choosing parameters that led to a minimum in potential energy near the experimentally observed bond lengths for that atomic pair. Only ionic interactions (see table 2.4) and the highly repulsive F-F interactions were modelled, as this were believed to have the strongest impact on the structure of the crystal. It was possible to use the F-F potential developed by Bulatov and Grimes [87], which was derived for the lanthanum trifluoride system. Due to the highly ionic character of the Li-F and the Al-F pairs, the attractive C_{ij}-parameter of the Buckingham potential was assumed to be zero, thus rendering the short-range part of the potential purely repulsive.

Table 2.4 – Types of bonding in $LiAlF_4$ glass system.

Bond	Difference in electronegativity Pauling scale	Bonding type
Li-F	3.00	ionic
Al-F	2.37	ionic
Li-Al	0.63	non-bonding

In each step of the fitting, one of the parameters of one of the potentials was varied manually, as it was found that the automatic fitting process sometimes fails to accurately account for the Phonon distribution, which can lead to negative (i.e. imaginary) phonon modes. If the resultant fit (with special regard for the lattice parameters of the unit cell) was judged to be better than previously, half the difference was added to the original value and a new parameter

was optimised. This was done to try and find the lowest energy minimum of the potential energy surface and repeated until an acceptable potential model was derived.

2.6.2 Derived Potentials for the LiF.AlF_3 system

The parameters obtained from static lattice fitting and a comparison of the quality of fit against experimentally observed unit cells of the given crystal are shown in tables 2.5 and 2.6. The F-F parameters used were those previously fitted for a lanthanum trifluoride model [87]. To encourage computational efficiency, long-range coulomb interactions beyond 10 Å were evaluated using the Ewald sum [67], with the short-range Buckingham interactions truncated at the same distance. In order to further improve the accuracy of the potential, a shell model was tested, which takes into account the polarisability of the fluorine atom, by attaching a massless charged shell to a charged core via a harmonic spring [88]. The aim of this harmonic spring in the shell model is to explicitly represent the polarisation of the electron shell of an ion [88]; an illustration of this model is presented in figure 2.4. Where the shell model was not used, formal charges were employed instead.

Table 2.5 – Derived Buckingham pair potential parameters for the LiF.AlF_3 system.

Pair i-j	A	ρ	C	reference
	eV	Å	eV Å^6	
Li^+- F^-	2575.0	0.260	0	-
Al^{3+}- F^-	1005.5	0.272	0	-
F^-- F^-*	1127.7	0.2753	15.8	[87]

*if using a shell model, q_{shell} and q_{core}, the charges on the shell and the core are -1.3776 eV and 0.3776 eV respectively. The spring constant F_{spring} was set to 24.36 eV Å^{-2} [87].

A good fit with experiment can be observed in table 2.6 with or without using a shell model, as the volume error remains below 1% in both cases. The addition of a shell for the fluorine interactions only marginally improves results in LiF and AlF_3, but slightly improves the fit to the experimental lattice parameters in the more complex α-Li_3AlF_6 structure. In the MD simulations, only the potential without a shell model was used, as the shell model is significantly more computationally expensive and limits the transferability of the potential; for little gain, as the bonding in this system is mostly ionic.

Due to the obscurity of this glass system and the resultant lack of experimental data of bulk

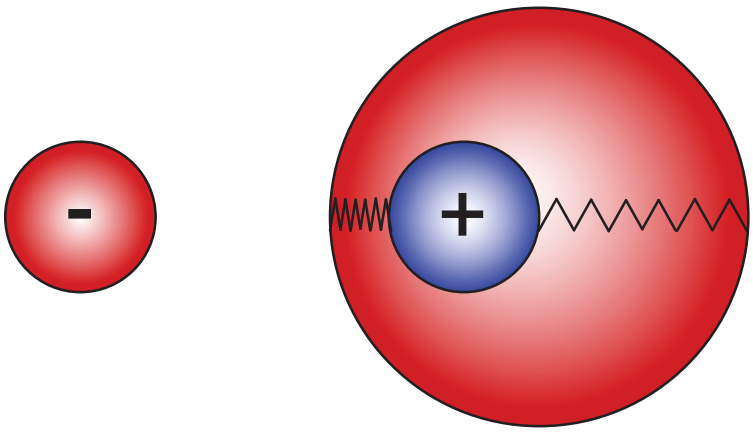

Figure 2.4 – Diagram illustrating the effects of the shell model [88], where the atom on the right is polarised by a negative charge on the left. The negative charge repels the negatively charged shell, whilst attracting the positively charged core. A spring attaches the core to the shell of the polarised atom, which is deformed due to the polarisation of the atom.

properties (such as elastic moduli or thermal expansion coefficients), no further potential validation could be undertaken. The good fit to lattice parameters across three different structures, however, does suggest a degree of transferability. The potentials should thus be suitable to predict glass formation in a wide range of aluminium-lithium-fluorides.

2.7 Molecular Dynamics Simulations

MD can be used to describe complex physical systems (in this case, the arrangement and dynamics of atoms in a glass) through Newton's laws of motion [89].

With an adequate description of inter-atomic forces, molecular dynamics allows the prediction of atomic positions as a function of time. These predictions rely on Newton's second law of motion [89] (for constant mass) solved for each particle [60]:

$$F(\vec{x},t) = m\vec{a}(\vec{x},t) \tag{14}$$

where F is the the sum of forces exerted on the atom by all other atoms in the system, t is time, m is the particle mass and $\vec{a}(\vec{x},t)$ is the acceleration vector of the atom at time t and Cartesian position $\vec{x}$. In order to allow for atomic positions and forces to evolve with time, equation 15 would need to be solved for each atom in the system.

$$m\frac{d^2\vec{x}_i}{dt^2} = \sum_{j\neq i} f\left(r_{ij}\right) \tag{15}$$

Solving this equation for anything but the simplest systems is impractical, therefore numerical integration is performed.

The velocity Verlet integration was used in all simulations here. It is a special case of the original Verlet algorithm [90], which requires the position and force at the current and previous steps to be known to predict the evolution of velocities and positions with time. The velocity Verlet algorithm on the other hand, does not require any data from the previous timestep. This allows the algorithm to be self-starting, requiring only the prediction of forces from the atomic configuration at the start of the simulation. The Cartesian position vector $\vec{x}\,(t)$ and the velocity vector $\vec{v}\,(t)$ at time t are used to predict position and velocity at time $(t+\triangle t)$, where $\triangle t$ is the timestep used. The acceleration vector $\vec{a}\,(t)$ is obtained from Newton's second law (equation 14). As the treatment of time is iterative, a smaller timestep will yield a more exact solution. The new Cartesian position vector and velocity vector are then given by:

$$\vec{x}\,(t+\triangle t) = \vec{x}\,(t) + \vec{v}\,(t)\,\triangle t + \frac{1}{2}\vec{a}\,(t)\,\triangle t^2 \tag{16}$$

$$\vec{v}\,(t+\triangle t) = \vec{v}\,(t) + \frac{\vec{a}\,(t)+\vec{a}\,(t+\triangle t)}{2}\triangle t \tag{17}$$

The MD code used for all the calculations presented herein, was DL_POLY_3 [65].

MD is a powerful tool, because the calculated properties of each atom (velocity, relative position and acceleration) can be linked to the bulk properties of the system (such as temperature, pressure and volume) by using statistical mechanics. Every step of the simulation will be a member of a thermodynamic ensemble.

2.7.1 Ensembles and Boundary Conditions

Evans [91] defines an ensemble as "an essentially infinite number of systems characterized by identical dynamics and identical state varaibles (N, V, E, or T etc.) but different initial conditions." The intensive and extensive quantities of the system do not change between the individual ensemble members sampled by MD timesteps.

If one assumes that in real systems, the atomic kinetic energies follow a Maxwell-Boltzmann distribution, then by the summation of the velocities of all the atoms in a system, the macroscopic temperature may be derived. Temperature, for example, can be calculated by using ensemble averages provided by the MD simulation instantaneously at every timestep of the simulation. Thus, the temperature of the system is kept in line with the ensemble by controlling the velocities of the atoms directly (see section 2.7.2). A MD simulation tends to sample energy minima (some of which may be metastable) for a given set of ensemble variables. By letting the system evolve over a period of time, a great number of thermodynamically likely configurations can be obtained. Assuming a long enough sampling time, the statistical average of positions with time is approximately equal to the average bulk properties of all possible structure variations to a point where they can be assumed to be indistinguishable. This is also known as the ergodic hypothesis [91]. From these sets of positions, certain properties of the system can then be extracted.

The most fundamental of the three ensembles used, is the micro-canonical ensemble. It is often referred to as NVE, as it fixes the number of particles in the system (N), the volume of the system (V), and the energy of the system (E). In a simulation this means that throughout the simulation, these three factors will not alter on average. It is the most fundamental, because unlike some of the other ensembles, it treats energy extensively, allowing the kinetic and potential energies to vary without constraints. It allows energy changes, provided that the total energy remains constant between ensemble members. It was used for equilibrium data collection where temperature control was not required.

In the canonical ensemble (NVT), the number of particles (N), volume (V) and temperature (T) of the system are fixed. It was used mainly in cases where the system is very unstable and would otherwise undergo large and highly unphysical temperature and volume changes, such as during the melt-quench of a glass composition.

The isothermal-isobaric ensemble (NPT) fixes the number of particles (N), the system pressure (P) and the system temperature (T). As volume is not fixed within the NPT ensemble, volume relaxation of the simulation cell can occur. This allows, for example, predictions of volume change due to radiation damage to be considered.

The simulated systems presented here contain of the order of 10^5 atoms. Although significant, this number is small in comparison to Avogadro's constant [92]. As a consequence, to allow a valid comparison with bulk properties, periodic boundaries were employed throughout.

2.7.2 Temperature and Pressure Control

In order to model the physical processes involved in glass formation it is necessary to control the temperature of the MD simulation using a thermostat. The equivalent mechanism for pressure is called a barostat and works along the same principles.

A thermostat scales the atomic velocities, which affects the instantaneous temperature derived from the sum of all atomic momenta (equation 18):

$$\sum_{i=1}^{N} \frac{|\vec{p}_i|^2}{2m_i} = \frac{k_b T}{2} (3N - N_c) \tag{18}$$

where $\vec{p}_i$ is the momentum of atom i, k_b is the Boltzmann constant, N is the number of degrees of freedom and N_c the number of constraints. The simplest form of a thermostat is to scale the velocities of all atoms in the system by a fixed factor to attain the target temperature. By simply scaling the velocities, energy is not conserved and thus the generated velocities are not part of the ensemble [93]. In addition, the lack of temperature oscillations can lead to locally metastable states to be sampled rather than a wider distribution of possible states, as these fluctuations may lead to a new, more stable minimum of the potential energy surface.

To produce true members of the isothermal ensembles (NPT, NVT), the concept of a time-delayed energy flux to and from an external energy buffer is required. The most common analogy for these kind of thermostats is that of a system coupled to a "heat bath" of the desired system temperature. This heat bath is used to gradually remove excess kinetic energy from the system, which is moved into an external energy buffer akin to a hot (or cold) object in a much larger bath of water, which slowly assumes the same temperature. This allows for

the rescaling of atomic energies, whilst keeping either the total momentum or the total energy (of the combination of simulation box and heat bath) constant. Equilibration occurs for a set period of time, allowing some of the energy to be transferred to or from the heat bath. In radiation damage simulations, the heat bath is only applied to atoms crossing the bounding box, as otherwise the energy introduced by a radiation event is removed too quickly from the system for damage to be adequately modelled.

Unless otherwise stated, a system-wide Berendsen thermostat [94] was used in NVT calculations. It allows more rapid convergence of the system when compared to other thermostats (such as Nosé-Hoover), making it more suitable for use during the early stages of a simulation. The Berendsen thermostat features a heat bath of a fixed temperature, but does not generate trajectories within the micro-canonical ensemble, as whilst it does conserve total momentum, it does not conserve energy [93]. For each atom, a friction term χ_{Ber} is applied to the unscaled velocity vector $\vec{v}(t+\triangle t)$ to produce the new velocity vector $\vec{v}_{scaled}(t+\triangle t)$ as follows:

$$\chi_{Ber}(t+\triangle t) = \left[1 + \frac{\triangle t}{\tau_T}\left(\frac{\sigma_{Ber}}{E_{kin}\,(t+\triangle t)} - 1\right)\right]^{1/2} \tag{19}$$

where

$$\sigma = \frac{N}{2} k_B T_{ext} \tag{20}$$

is the energy of the Berendsen thermostat [94], which depends on the degrees of freedom N of the system, the external temperature T_{ext}, which corresponds to the temperature of the heat bath and τ_T, which called the relaxation parameter and is related to the frequency of temperature fluctuations (kept fixed at 1 ps in all simulations here). Thus,

$$\vec{v}_{scaled}(t+\triangle t) = \vec{v}(t+\triangle t)\chi_{Ber} \tag{21}$$

Nosé-Hoover thermo- and barostats [95] were used in NPT simulations. The Nosé-Hoover algorithm does not adjust the velocities of the next time step directly, but rather changes the rate at which the velocity changes. This ensures that all trajectories are in line with the canonical (NVT) ensemble in the real system and the micro-canonical ensemble in the extended system.

However, unlike Berendsen [94], the lack of direct scaling retards the thermostat effect, and will lead to stronger oscillations [93]. This is not a serious problem in a system close to its thermal equilibrium. The velocity change is given by

$$\frac{d\vec{v}(t)}{dt} = \frac{\vec{a}(t)}{m} - \chi_{NH}(t)\vec{v}(t) \tag{22}$$

a first order differential equation controls the friction coefficient χ_{NH}

$$\frac{d\chi_{NH}(t)}{dt} = \frac{2E_{kin}(t) - 2\sigma}{q_{mass}} \tag{23}$$

where σ is the thermostat energy as given in equation 20, and q_{mass} is the Nosé-Hoover thermostat mass given by

$$q_{mass} = 2\sigma\tau_T^2 \tag{24}$$

which depends on the relaxation parameter τ_T (fixed to 1 ps in these studies).

2.7.3 Glass Simulations

Glasses were formed using a simulated melt-quench procedure, which mimics the thermal processes used to form a glass experimentally. To create a starting structure for the melt-quench procedure, a regular lattice was populated with the desired glass composition. This was then heated to 5300 K in the NVT ensemble to produce a randomised structure, which was subsequently cooled to 300 K in iterative steps of 500 K at (a nominal quench rate of 10 $K\,ps^{-1}$). At each step, 25 000 steps of MD were performed, with velocities being rescaling during the first 5000 steps. The system is then allowed to evolve in an NVT ensemble, with a 2 fs timestep used throughout (unless otherwise stated). In terms of the computational procedure, changing the temperature in an NVT ensemble requires the simulation to be restarted (but conserving the previous step's structure) and the velocities to be scaled to the new temperature. Once room temperature (300K) is reached, the ensemble is changed to NPT to allow the system to fully equilibrate without the volume constraint. If enough time was allowed for the system to equilibrate at each step, this change to NPT should not result in a sudden volume expansion,

but the system should converge on a density that closely matches experiment, before data is collected in the energy conserving micro-canonical (NVE) ensemble. The full set of simulation parameters are reported in table 2.7.

2.8 Radiation Damage Cascades

This section will discuss the methods and mechanisms used to simulate radiation damage effects on glasses, including both Monte Carlo and MD approaches.

2.8.1 Stopping and Range of Ions in Matter Simulations

The Stopping and Range of Ions in Matter (SRIM) software package [80, 96] was used to estimate the required box sizes for the radiation damage cascades performed, presented in the following section. SRIM is often used to determine ionic ranges in various amorphous materials. It simulates the penetration depth of ions by using a hard sphere collision Monte Carlo method and relies on the ZBL potential to calculate binary collisions in addition to electronic stopping power [80]. All cascades modelled rely on transport of ions in matter (TRIM) calculations in which a high energy (in the keV range) is assigned to an atom travelling into a non-free surface. The distance travelled by the atom before each impact is randomly based on the density and composition parameters of the material. Essentially, this means that a material in TRIM is a fully homogeneous continuum. By comparison to MD, SRIM/TRIM calculations are simpler as they do not fully account for the evolution of atomic coordinates resulting from non-impact interactions (e.g. thermal vibrations). Whilst this limits their use in the study of diffusion and structural changes, it allows for comparatively large volumes and impact energies to be studied at longer timescales.

2.8.2 Molecular Dynamics Simulations

MD simulations were used to model the effects of a PKA interacting with the glass structure in a series of elastic collisions, and causing a damage cascade. A pre-quenched glass obtained from a melt-quench (as described in section 2.7.3) was used as the starting configuration, but equilibrated at a temperature of 500K to model the elevated temperatures under repository conditions [22]. Whilst the simulations were performed in the isothermal-isobaric ensemble

(NPT) and thus had to be thermo- and barostatted in DL_POLY_3, a long relaxation parameter of 1 ns was chosen to allow the cascade to locally heat and/or melt the glass before the heat bath forces the temperature to drop. The increased relaxation parameter to periods longer than the simulation of the damage events drastically reduces the impact of the thermo- and barostat, which would otherwise drain the additional energy too quickly. The use of an NPT ensemble allows a volume expansion following the radiation damage cascade, as density changes are commonly observed in materials suffering from radiation damage [22]. The parameters used are summarised in Table table 2.8.

For each cascade, an atom of a specific type (e.g. silicon) from within the simulation box was selected at random and assigned a velocity vector of defined kinetic energy for each run and with a direction vector into the bulk. To ensure that the trajectory is captured in sufficient detail, the variable timestep feature of the DL_POLY_3 code was used. This allows the Molecular Dynamics to proceed using the standard timestep unless an atom moves more than a certain distance (0.3 Å in this simulation), which will cause the timestep to be shortened accordingly. For each cascade, 5000 of these variable timesteps were allowed before another cascade was initiated.

2.9 Structural Analysis

Several tools were used to analyse both the quality of the obtained glasses, as well as the effect of radiation damage.

2.9.1 Pair Distribution Functions

A distribution function correlates the structural information contained within the coordination environments of all atoms. It allows insights into the bond lengths and bonding environments of the different species. The Visual Molecular Dynamics (VMD) package [97] was used to view the system and generate pair distribution functions (PDFs) for various ion pairs. These distribution functions could then be broadened to allow for comparison with experimental techniques, which takes into account peak broadening due to the limitations of the equipment. This was done by convolution with the experimental instrument peak function to allow for a proper comparison and follows the method outlined by Wright [98].

2.9.2 Bond Angle Distributions

Si-O-Si bond angles and O-Si-O bond angles were calculated using the VMD package [97], as the angles obtained within the network former backbone of the glass can reveal important structural information.

2.9.3 Ring Size Analysis

An effective way of obtaining numerical data concerning the geometry of a glass is to analyse the size of network former rings. Cormack's definition of a ring in a three-dimensional structure was used [99], and only the number of Silicons in a ring was counted, with each silicon being connected to the next by exactly one oxygen. An example for a four-membered ring is shown in figure 2.5. As the simulation was finite in its dimensions, a minimum image convention was maintained to make sure the rings correctly extended across the periodic faces of the cell.

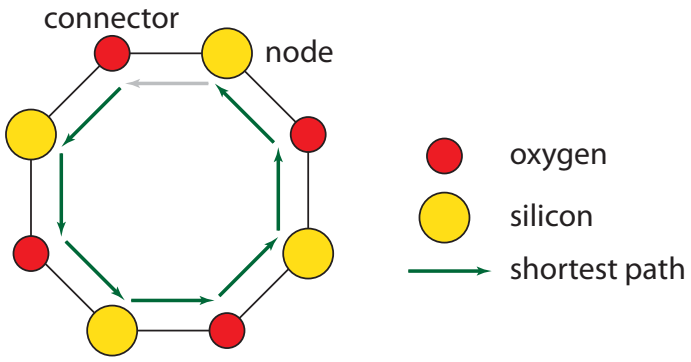

Figure 2.5 – Diagram illustrating the shortest path linking the connector back to the node for a size 4 ring.

The calculation involved the following steps:

- A node and a connector are defined (in this case silicon and oxygen, respectively)
- A cutoff distance is chosen that represents the maximum bond length of node and connector (2.0 Å was used throughout)
- A network of edges between all bonded silicon and oxygen atoms is generated

- For each node:
    - The number of bonded connectors was determined (e.g. the number of bonded oxygen atoms)
    - The number of steps in the shortest path back to the node from each of the bonded connectors, disregarding the bond itself, was determined using an unweighted Dijkstra's algorithm

The ring size, or number of nodes in each ring for each bonded connector is then given by:

$$ring\ size = \frac{1 + length\ of\ shortest\ path}{2} \tag{25}$$

Table 2.6 – Quality of potential fit against experiment [84–86], where *a*, *b* and *c* are the lattice parameters of the crystal unit cell. α, β and γ are the internal angles of the unit cell. Percentage deviations from experiment shown in brackets.

parameter	model	$Li_3 Al F_6$	$Al F_3$	Li F
Volume (Å^3)	expt.	381.62	262.08	16.326
	no shell	382.50 (0.23)	260.35 (-0.66)	16.326 (0.00)
	shell	382.15 (0.14)	262.94 (0.33)	16.326 (0.00)
a (Å)	expt.	9.5100	4.9310	2.8475
	no shell	9.4629 (-0.50)	4.9696 (0.78)	2.8475 (0.00)
	shell	9.5036 (-0.07)	4.9860 (1.11)	2.8475 (0.00)
b (Å)	expt.	8.2295	4.9310	2.8475
	no shell	8.2829 (0.65)	4.9696 (0.78)	2.8475 (0.00)
	shell	8.2400 (0.12)	4.9860 (1.11)	2.8475 (0.00)
c (Å)	expt.	4.8762	12.446	2.8475
	no shell	4.8801 (0.08)	12.173 (-2.19)	2.8475 (0.00)
	shell	4.8802 (0.08)	12.213 (-1.87)	2.8475 (0.00)
$\alpha/\beta/\gamma$	expt.	90°/90°/90°	90°/90°/120°	60°/60°/60°
	no shell	90°/90°/90°	90°/90°/120°	60°/60°/60°
	shell	90°/90°/90°	90°/90°/120°	60°/60°/60°

Table 2.7 – Simulation parameters used in DL_POLY_3.

Parameter	Units	Glass system	
		$xNa_2O.(1-x)SiO_2$	$LiAlF_4$
short range potential		Buckingham (BKS, Teter); Morse (Pedone)	Buckingham (own work)
long range cutoff	Å	12.616	10.0
short range cutoff	Å	12.616 / 4.927	10.0
ZBL spline?		yes	no
starting temperature	K	5300	5300
cooling rate	K ps^{-1}	10	10
cooling ensemble	-	NVT	NVT
timestep	ps	0.002	0.002
cooling thermostat (relaxation time)	ps	Berendsen (10)	Berendsen (10)
equilibration ensemble	-	NPT	NPT
equilibration thermostat (relaxation times)	ps	Nosé-Hoover (10, 10)	Nosé-Hoover (10, 10)
equilibration temperature	K	300	300
equilibration time	ps	200	200
data collection ensemble	-	NVE	NVE
data collection thermostat (relaxation times)	ps	Nosé-Hoover (10, 10)	Nosé-Hoover (10, 10)
data collection time	ps	2	2
data collection rate	ps^{-1}	50	50

Table 2.8 – DL_POLY_3 radiation damage simulation parameters in $xNa_2O.(1-x)SiO_2$ type glasses.

Parameter	Units	
starting temperature	K	500
Na_2O content	mol %	20 / 30
PKA energy	keV	10
PKA species		Silicon
equilibration ensemble	-	NPT
equilibration thermostat (relaxation time)	ps	Nosé-Hoover (10, 10)
equilibration time	ps	20
PKA ensemble	-	NPT
PKA thermostat (relaxation time)	ns	Nosé-Hoover (1, 1)
time per PKA	ps	5

3 Validation of the Glass Model

In this section, the theory of glass structure will be discussed, followed by a section outlining the structure of the simulated glasses and how they compare with experiment. Finally, predictions will be made of how radiation damage can affect structure and properties.

3.1 The Theoretical Structure of Silicate Glass

Before the simulated glasses can be discussed, it is important to consider the current theories of glass structure and those glass properties that may be obtained experimentally. The traditional definition of a glass is that of an "inorganic product of melting, which when cooled without crystallisation, assumes a solid state" [10]. Rather than being periodic in its structure as would be expected for a crystalline phase, a lack of long-range structure is retained from the disordered melt. This is reflected in an early theory of silicate glasses: the random network theory, which was first proposed by Zachariasen, and proposes that silica glasses are made up of corner-sharing tedrahedra [9]. The original Zachariasen drawing (shown in figure 1.3) only shows a two-dimensional structure. Each of these tetrahedra consists of an sp^3 hybridised silicon atom, covalently bonded to four oxygen atoms, with an internal O-Si-O angle of 109.5° [100]. The silica tetrahedra may twist about the bridging oxygen bonds, leading to the variations in the Si-O-Si bond angles. Hence, silicon bonds are specified in all three dimensions, whereas oxygen bonds are specified in only two dimensions, leaving one degree of freedom that provides the basis for the lack of long range order [101].

In this model, the overall structure is affected by three types of components: network formers, network modifiers and intermediates. Network formers make up the backbone of the glass. In the case of silicate glasses, silicon (Si^{4+}) is the network forming cation responsible for creating a network of linked tetrahedra. Another important network former is boron (as boric acid), which is commonly found in nuclear waste glasses and can form its own network.

The network can be locally distorted or broken up by network modifiers, such as the alkalis sodium or lithium (usually added in their oxide forms), which add additional ionic oxygen (O^{2-}) to the system. For each ionic oxygen added, one Si-O-Si bond is broken, with both the ionic oxygen and the existing bridging oxygen (BO) forming non-bridging oxygen (NBO), charge balanced by the monovalent cation (e.g. Na^{+}). The energy difference between the two

states of oxygen can be shown experimentally by deconvolution of the O_{1s} binding energy distribution peak as measured by x-ray photoelectron spectroscopy [101].

Intermediates, such as aluminium, can act as both network formers and network modifiers and improve thermal shock resistance and mechanical behaviour. Not only are they typically added in their oxide forms, providing ionic oxygen, they also have high coordination numbers (between six and eight), allowing for bond flexure and adding void space [101].

The role and distribution of network modifiers in particular, including the alkalis sodium and lithium, has been the focus of attention for a number of reasons. Network modifiers not only affect important properties, such as the melting temperature, glass transition temperature, mechanical strength, but they also interact with each other [102]. According to Zachariasen's random network theory, alkali ions are statistically distributed throughout the polymerised structure, and due to their positive charge, increase the separation between the network forming cations [9].

An advancement on this theory was made, however, with the modified random network theory proposed by Greaves [103]. He argues that, rather than having a uniform, random distribution in the glass, network modifiers have a tendency to cluster in a manner to form narrow channels throughout the glass structure (see figure 3.1). The presence of these channels is thought to have a profound effect on the properties. Crack propagation in glasses for example, is theorised to be preferential along these weaker modifier channels [104]. This could be detrimental to the performance of nuclear waste glasses, as the swelling inside an enclosed space may cause cracks along alkali rich layers, potentially promoting not only the migration of radionuclides along these channels to the surface thereby being prone to leaching, but also leading to a local dissolution of the glass [105].

Another factor that affects properties such as alkali diffusivity, electrical conductivity and viscosity is the so called Mixed Alkali Effect (MAE), which describes a large deviation from additive behaviour when more than one alkali is part of the glass composition [102]. In materials that exhibit additive behaviour, the bulk properties are a composite of the respective bulk properties of the constituents, weighted by their concentrations. In a composition containing two alkalis however, there is a large deviation from what would be predicted by the additive rule. The effect will be most pronounced when a 50:50 ratio is reached. In lithium-sodium glasses, this has been shown experimentally to reduce the electrical conductivity by

several orders of magnitude, and lower the glass transition temperature significantly [107]. A schematic of this effect is shown in figure 3.2. T_g values of glasses are typically between 775 K (soda-lime glasses) and 1475 K (amorphous silica) [108], so the mixed alkali effect can significantly reduce the glass transition temperature.

The experimental study of both the modified random network theory and the origins of the mixed alkali effect have been difficult, however, as both are highly localised. Structural analysis of glasses in general is difficult to perform experimentally, as the lack of periodicity means that a great variety of local atomic structures may yield similar observed bulk properties. In this field, it is therefore useful to perform computer simulations. Assuming the model replicates the experimentally observable bulk properties, a computer model can provide insight into features and effects such as alkali clustering, which can not be analysed experimentally. Even though all atomic positions are known in a simulation, it is still possible to obtain the correct bulk properties from an incorrect structure. Care must thus be taken when analysing and comparing data from simulations and experiment.

3.2 Structural Validation of the Model

Having introduced the common structural features of all silicate glasses, the simulated glasses can now be compared to experiment. The Pedone [77], BKS [78] and Teter [79] potentials will be compared and contrasted, to reach a conclusion on the predictive quality of each potential.

3.2.1 Density Comparison

The volume of a glass is affected by the degree of polymerisation, and hence the bond density [101]. Crystalline materials reduce their energy and volume by forming bonds; as glasses exhibit more disorder and higher volumes, they represent a higher energy state. The bulk properties will then be determined by the energy state of the material. A simple and effective way of judging the ability of a set of interatomic potentials to reproduce real bulk properties is thus to compare the density fit of modelled compositions to experiment. In order to obtain the best possible densities, a cutoff comparison was performed between a short (4.927 Å) and a long (12.616 Å) short-range cutoff. The cutoffs are based on the regression optimisation of Pedone's potential by Pota *et al.* [109], which tried to isolate the effects of various simulation

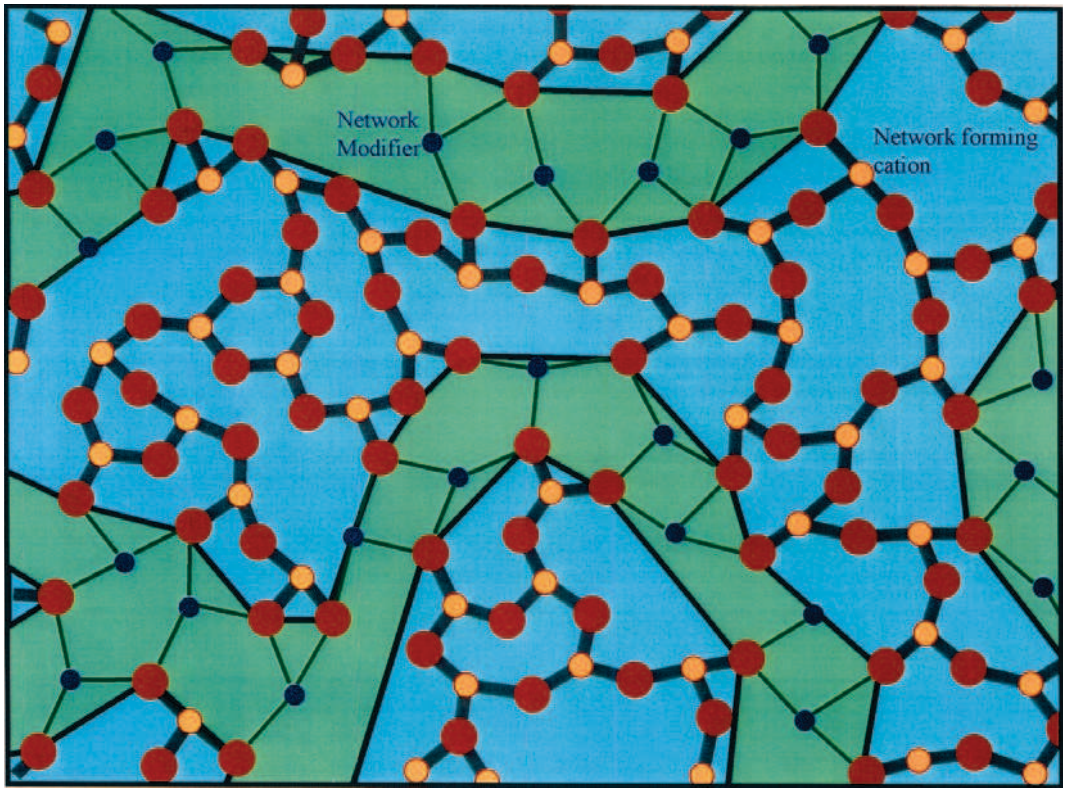

Figure 3.1 – The modified random network structure proposed by Greaves. Image taken from Greaves [106].

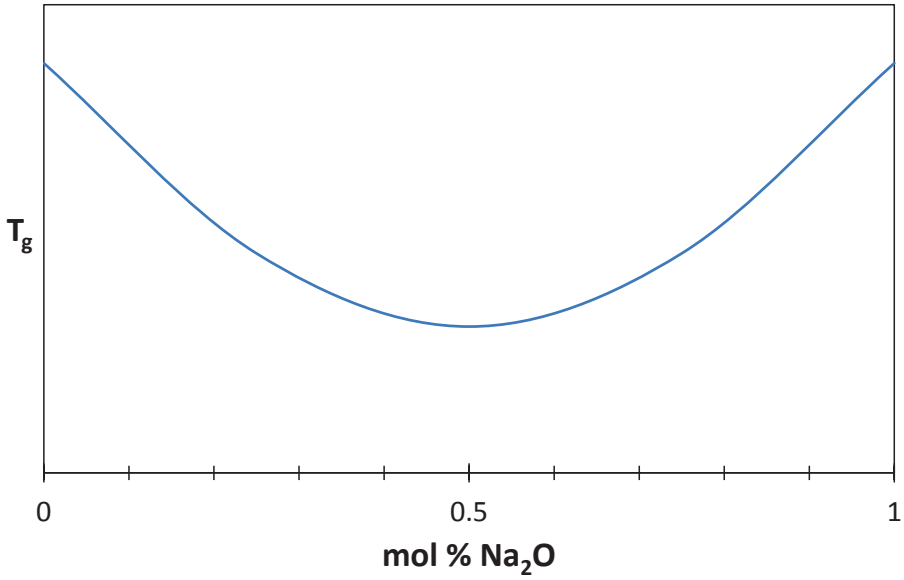

Figure 3.2 – Schematic of the mixed alkali effect observed in the glass transition temperatures of sodium lithium silicate glasses.

parameters and determine the optimum parameters where the closest match to experiment is achieved. Tables 3.1 and 3.2 compare the densities obtained for simulated glasses of various compositions to experimentally observed values for short and long cutoff values. Experimental densities were taken from Shackelford [110].

Table 3.1 – A comparison of simulated densities based on Pedone, BKS and Teter potentials for a silicate glass of composition $xNa_2O.(1-x)SiO_2$ with a short-range potential cutoff of 4.927Å and experimental densities [110].

potential	Na_2O x	exp. density [110] g cm^{-3}	sim. density g cm^{-3}	density deviation %
Pedone	0.2	2.383	2.388	0.227
	0.3	2.459	2.458	0.026
BKS	0.2	2.383	2.254	5.395
	0.3	2.459	2.237	9.037
Teter	0.2	2.383	2.361	0.924
	0.3	2.459	2.405	2.202

Table 3.2 – A comparison between simulated densities based on Pedone, BKS and Teter potentials for a silicate glass of composition $xNa_2O.(1-x)SiO_2$ with a short-range potential cutoff of 12.616Å and experimental densities [110].

potential	Na_2O x	exp. density [110] g cm^{-3}	sim. density g cm^{-3}	density deviation %
Pedone	0.2	2.383	2.561	7.453
	0.3	2.459	2.630	6.945
BKS	0.2	2.383	2.441	2.436
	0.3	2.459	2.449	0.420
Teter	0.2	2.383	2.536	6.432
	0.3	2.459	2.597	5.603

With density errors of only 0.026% and 0.227%, the Pedone potential is best suited to a short cutoff length. The short-cutoff is desirable in order to run large simulations. However, chosing a longer cutoff, Pedone potentials predict values that are 7.453% and 6.945% too large, compared to only 2.436% and 0.420% achieved by BKS. This suggests that a significant part of the overall potential arises from the forces between the two cutoff lengths in both BKS and Pedone potentials.

Ideally, the short-range interatomic forces tend to zero at or before the short-range cutoff distance. Any residual energy predicted by the potential will lead to a step at the cutoff. If no

Table 3.3 – Cutoff forces in the short-range potential of Si-O.

cutoff Å	force at cutoff eV Å^{-1}		
	Pedone	BKS	Teter
4.927	0.004687	0.011372	0.004657
12.616	0	0.000016	0.000006

Table 3.4 – Cutoff forces in the short-range potential of O-O.

cutoff Å	force at cutoff eV Å^{-1}		
	Pedone	BKS	Teter
4.927	0.016085	0.010139	0.013215
12.616	0	0.000021	0.000023

measures are taken to correct this, this would lead to a discontinuity in the potential function and hence an infinite force at the cutoff separation. This occurs for any residual energy and is independent of the magnitude of the predicted cutoff energy. To prevent this, the DL_POLY_3 code tails the energy to zero at the cutoff, avoiding the problem of a discontinuous function but still introducing a potentially unphysical region to the pair potential. The resultant potential forms the basis of the internally tabulated potential energies and the corresponding forces (the first derivative of the potential energy gradient between two points) internally. This tail correction is necessary, but leads to a sudden change in gradient in both the forces and energies near the cutoff and may impact the quality of results.

From the comparison of residual forces at the cutoffs given in tables 3.3 and 3.4, it can be seen that the residual forces are small, and that there exists a residual even at the long cutoff, so that a longer cutoff does not avoid the truncation of the potential. The long cutoff residual is so small however, that numerical errors due to the finite accuracy in the way the potential tables are derived could be responsible.

Plots of the Si-O potential energy and the O-O potential energy as a function of distance may further help to illustrate differences between the potentials (see figures 3.3 and 3.4). The Pedone potential features a smaller equilibrium separation in the Si-O potential (i.e. its minimum occurs at lower value of r_{ij}). In theory, this could be balanced by a more repulsive

O-O potential, but the forces at or near the O-O equilibrium separation are very similar for the BKS and Pedone potentials. Another possible explanation for this discrepancy is the fit to different structures during the potential derivation, which specifically involved glasses in Pedone's potential derivation.

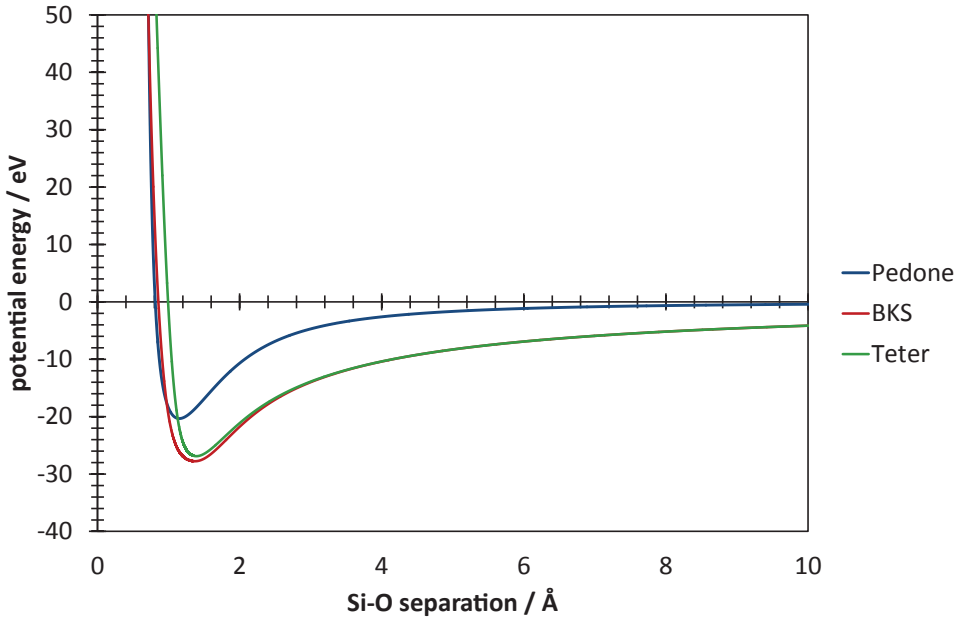

Figure 3.3 – Si-O potential parameter comparison, including electrostatic potential.

The Na-O potential features the same trend as seen for the Si-O potential. The differences in equilibrium separation of the different potential pairs may impact the transferrability of the potential set to different compositions. Whilst the density error varies little for the two probed compositions, the prediction accuracy of the BKS is very composition dependent, even at long cutoffs.

The density error and consequently the volume error will become especially important when radiation damage simulations are performed and the resulting volume change is investigated. The indifference to compositional changes for the Pedone potential might suggests that it is more reliable in possible local composition changes as the result of radiation damage. On the other hand, the repulsive terms are rather different for the Pedone potential and follow a different format than the ZBL potential that was splined onto the Buckingham terms and is

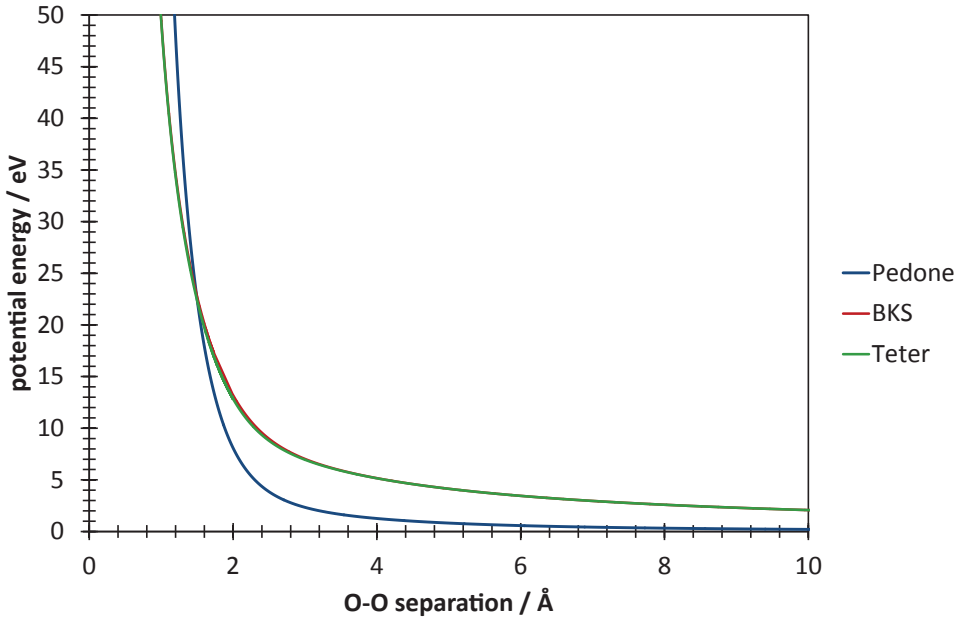

Figure 3.4 – O-O potential parameter comparison, including electrostatic potential.

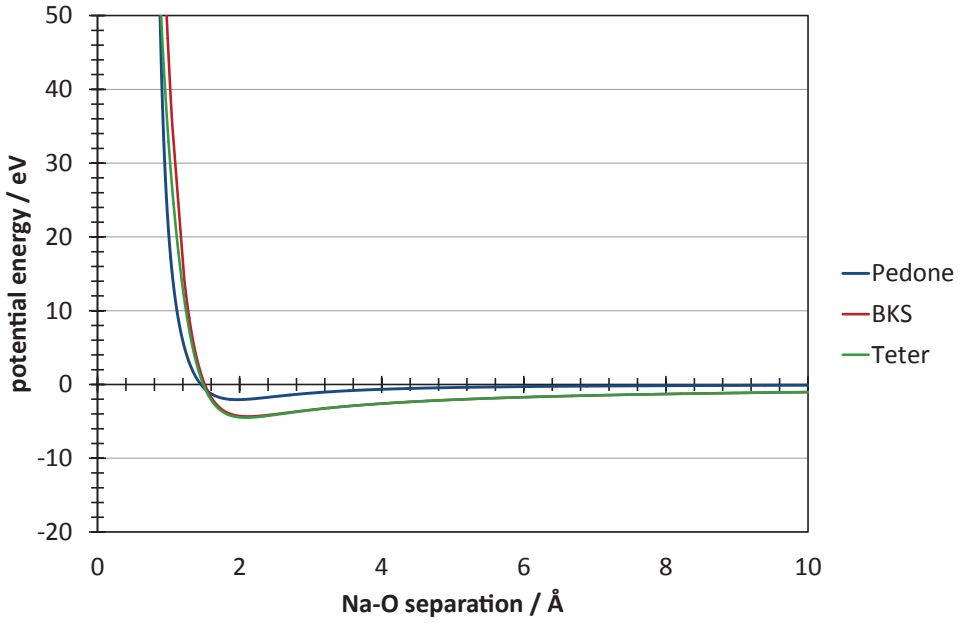

Figure 3.5 – Na-O potential parameter comparison, including electrostatic potential.

used to model nuclear repulsion in the SRIM/TRIM code [80].

Given the good density match and compositional transferability of the Pedone potential at short cutoff lengths, it will be employed later in this thesis, despite the steps observed in the interatomic potential functions. The BKS potential, although a longer cutoff is needed for accurate results, features a different potential form, and can be easily combined with a ZBL potential, so that it will be a useful comparison tool in any further radiation damage work. The Teter potential offers no significant advantages and will not be taken forward beyond this chapter.

3.2.2 Distribution Functions

A visualisation of a structure obtained from an MD simulation is presented in figure 3.6. Whilst the visual inspection of MD is relatively simple with advanced visualisation software, such as VMD, it is also important to compare structures quantitatively [97]. For this purpose, the structure of a glass can be numerically expressed in the form of distribution functions (see chapter 2.9.1 for more information). These are readily obtained from simulation as well as experimental neutron diffraction and X-ray spectroscopy, allowing for validation of model structures against experiment. Figure 3.7 shows a comparison of the total correlation functions of experiment and simulation. The simulated pair distribution functions were convulated with the instrument function relevant to the experimental data with which a comparison was to be made. This instrument function depends on the experimental real space resolution, which is limited by the scattering factor Q_{max}. In so doing, peaks within the distribution function were broadened in a manner consistent with the resolution of the experimental data, thus rendering experiment and simulated results to be more comparable [111].

Likewise, a comparison of the results obtained using the three potentials is presented in figure 3.8. From first inspection, it is apparent that all the potentials are very similar. However, in the course of this section it will become clear that the potentials do differ in certain features, which is not reflected by simply referring to a distribution function.

A number of distinct peaks are observed in the experimental and simulated total correlation function. Each peak effectively represents a bond length distribution of a particular pair of atoms. In general, there seems to be a good fit of the simulated peaks with experiment,

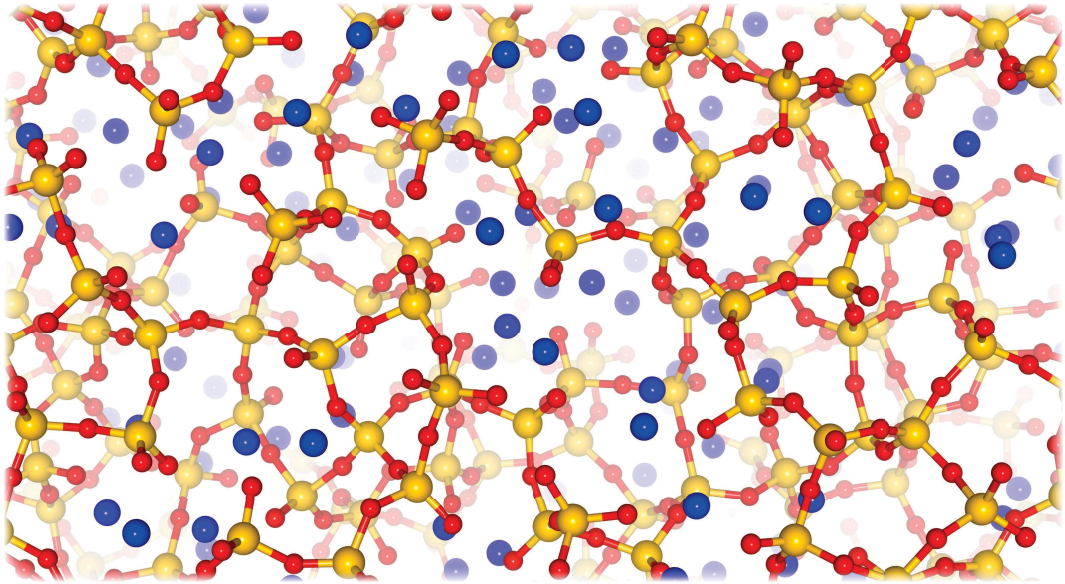

Figure 3.6 – Amorphous glass network modelled using Pedone potentials (n.b. bonds crossing the image plane are not shown). Silicon atoms are shown in yellow, oxygen in red and sodium in blue.

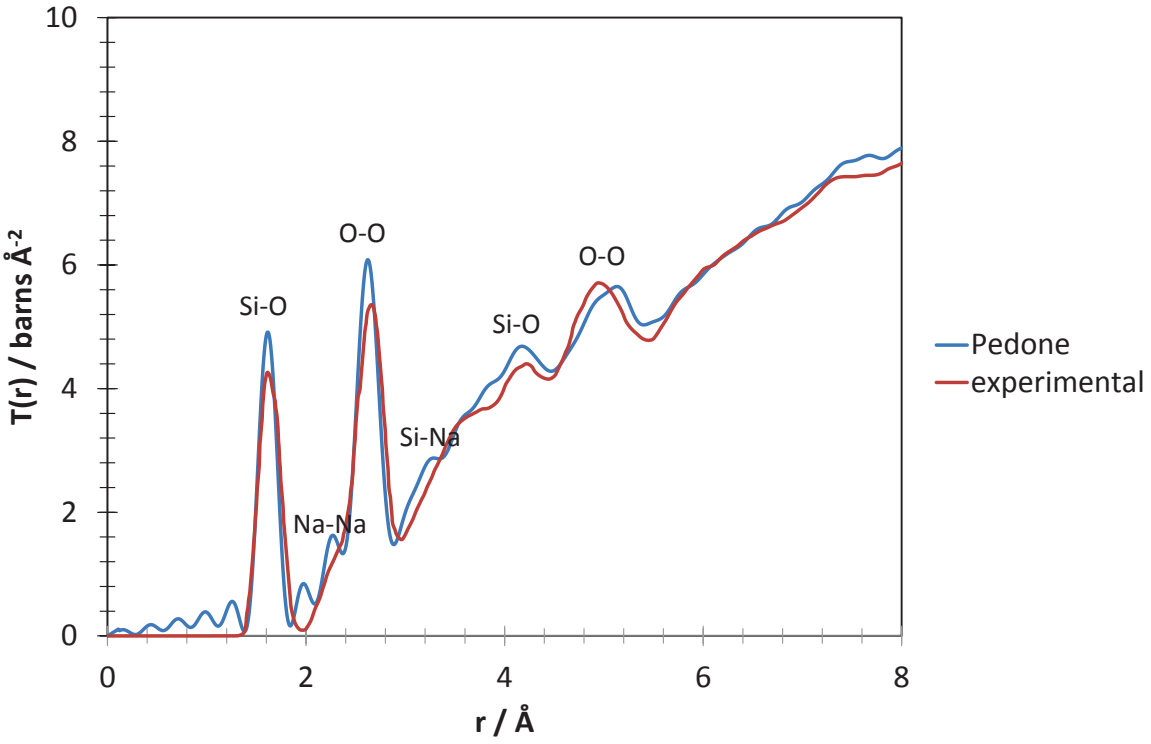

Figure 3.7 – Broadened simulated total correlation function compared to neutron diffraction data by Wright *et al.* [112] (Q_{max} = 22.88Å) for a glass containing 30 mol% Na_2O. Neutron data digitised from Yuan and Cormack [113].

especially for the first coordination shell peak positions.

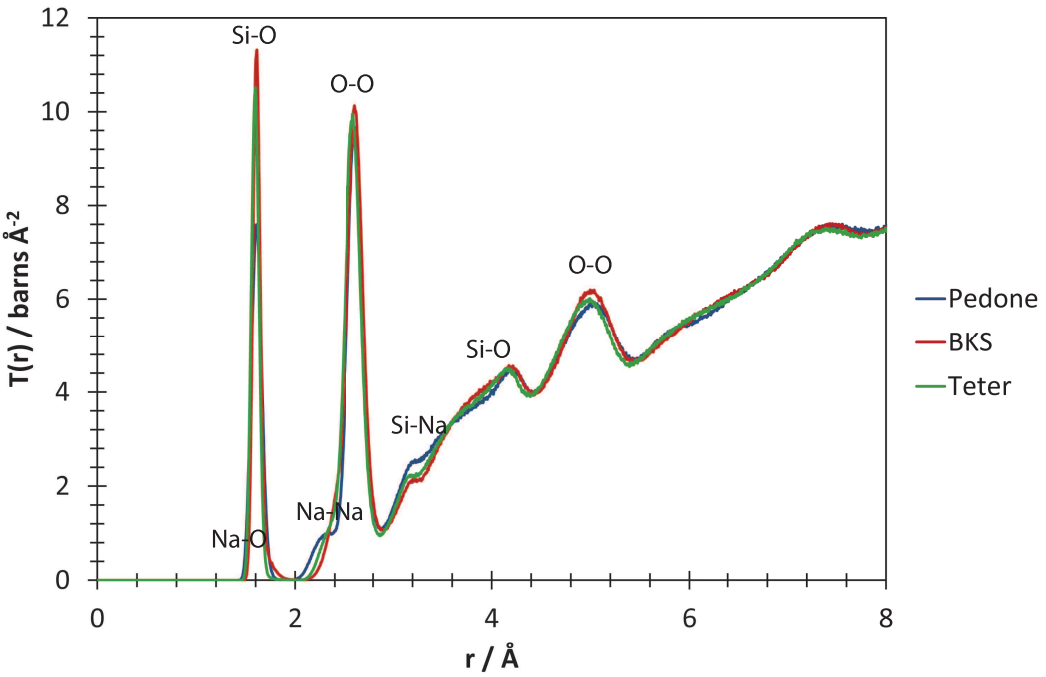

Figure 3.8 – A comparison of total correlation functions using the same simulation procedures and a short-range cutoffs of 4.927 Å for Pedone [77] and 12.616 Å for BKS [78] and Teter [79] potentials respectively.

3.2.3 Bond Angle Distribution

The O-Si-O bond angle distribution is a good indicator of how well a potential set describes the basic building blocks of the glass, namely the SiO_4 tetrahedra. Theoretically, this angle should be 109.5°, and any deviation will result in distorted tetrahedra. The simulated bond angles are presented in figure 3.9. All three potentials show a distribution about a peak at 108.5°, suggesting that the tetrahedral structure is only very slightly distorted. This distribution is responsible for the width of the first and second Si-O and O-O peaks in the distribution function. The full width at half maximum is 11.9°, 12.0° and 12.2° for Pedone, BKS and Teter potentials. This is lower than the bond angles predicted in vitreous silica reported as 14.0° elsewhere [114]. A possible explanation is that the removal of bond constraints through depolymerisation of the glass network actually enables the silicon oxygen tetrahedra to reach more optimal configurations.

The overall distribution matches the theoretical bond angle, and is indicative of the tetrahedral structure that dominates silicate glasses. Only the BKS potential deviates from theory, and

shows a second peak at an angle of only 88.5°. This indicates the presence of a defect within the glass, most likely an octahedron, which has internal bond angles of 90° and 180°.

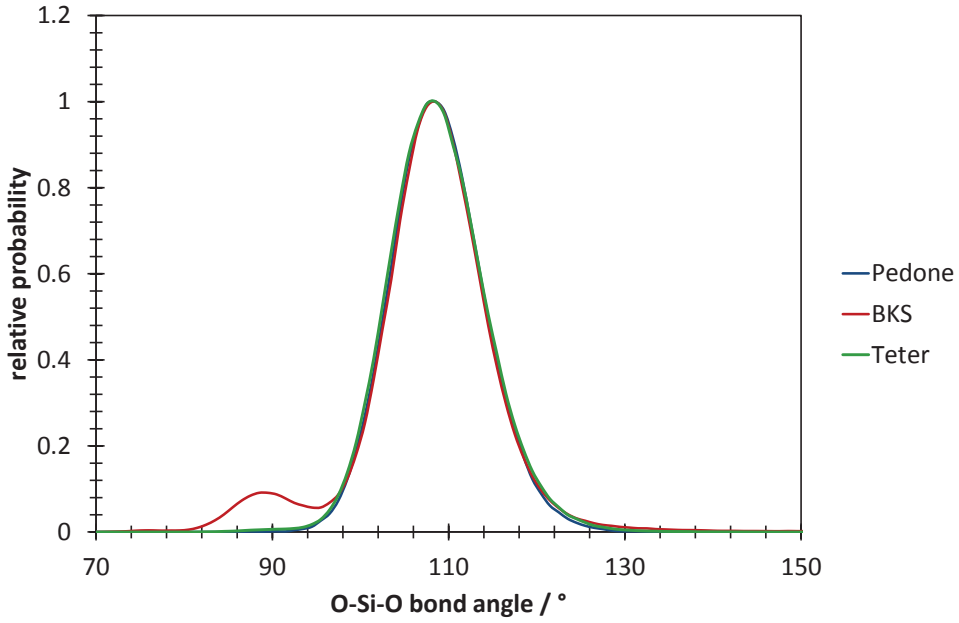

Figure 3.9 – O-Si-O bond angles in 30 mol% Na_2O glass

Si-O-Si bond angles have been proposed as an important structural feature that affects in particular the mid range order of glasses [114, 115]. As can be seen in figure 3.7, there is a shoulder in the experimental distribution function at 3.7 Å, which is missing from the simulation result. This shoulder is caused by the mid-range, second coordination shell Si-O bonds. The discrepancy is related to the broad Si-O-Si bond angle distribution (see figure 3.10) that is observed in the simulations performed. The variation in bond angle distributions determined by different experimental techniques such as X-Ray diffraction (XRD), nuclear magnetic resonance, or Hard XRD (HXRD), make it difficult to judge whether this shoulder should exist or not. Unlike neutron diffraction, HXRD for instance does not show any shoulder at this separation [115]. The peak bond angles observed were 149.5°, 146.5° and 148.5° for Pedone, BKS and Teter potentials respectively. This is similar to the experimentally observed bond angles formed in quartz (see Vashishta *et al.* [116] for a summary of crystalline SiO_2 phases), which has a bond angle of 143.7° in the alpha phase and 150.9° in the high temperature beta phase. The higher angle compared to α-quartz is due to the presence of non-bridging oxygens

caused by sodium depolymerisation.

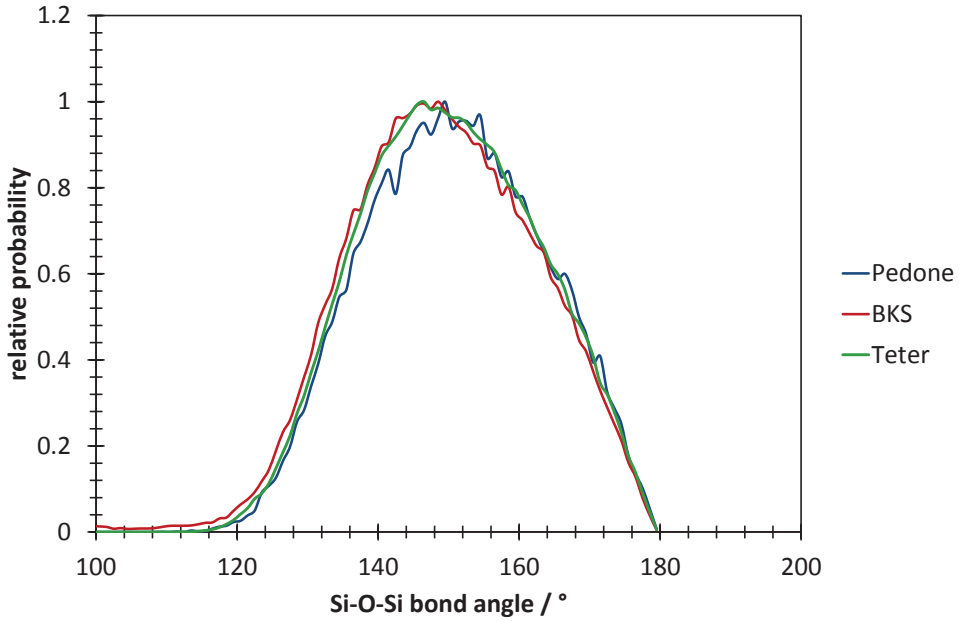

Figure 3.10 – Si-O-Si bond angles as obtained by the different potentials for a glass containing 30 mol% Na_2O. Cutoffs are 4.927 Å for Pedone [77] and 12.616 Å for BKS [78] and Teter [79] potentials.

3.2.4 Network Connectivity

Although the simulated melt-quench procedure attempts to mimic the thermal processes that may be used to produce a glass in the laboratory, the relatively short time spans accessible by MD mean that the simulated quench rate is about several orders of magnitude faster than real cooling rates [61]. It has been shown however, that in particular the coordination defects in the simulated structure are related to the quench rate employed [61].

The inter-connectivity of silica tetrahedra contributes to properties such as corrosion resistance. In a fully polymerised silicate glass, every silicon would be surrounded by four oxygens, each bonded to another silicon, the same way that silicon is coordinated in quartz. In Q_n notation, this is referred to as a Q4 structure. With the addition of sodium however, sodium atoms position themselves between the oxygen atoms at the corners of these tetrahedra, breaking the Si-O-Si bond and leading to the formation of NBOs; the more sodium atoms present,

the more oxygens that do not form a bridging bond between two silicons. This leads to Si ions surrounded by only three bridging oxygens, and thus a structure containing Q3 species. Lower Q structures can be reached if more sodium is present, until none of the tetrahedra are linked, referred to as Q0 structure.

The average Q structure of the glass is called the network connectivity, and can be easily calculated by knowing the relative compositions of network formers and modifiers and the number of bridging bonds that are destroyed for each unit of network former added. In the case of soda, one such bond is broken for every unit added, leading to a theoretical network connectivity of 3.143 in a 30 mol% Na_2O sodium silicate glass.

As the sodium atoms are not distributed evenly in glasses (as proposed by the modified random network theory [103]), lower Q structures than compositionally expected can be formed. Using molecular dynamics, these structures can be modelled and analysed. The Q speciation of a soda silicate glass is given in figure 3.11. The different potentials show significant differences. Whilst Pedone and Teter potentials predict that Q3 tetrahedra predominate, BKS potentials predict mostly Q4 tetrahedra and even some Q5 species. The prediction of Q5 species has been shown to be cooling rate dependent, and indicates the presence of edge sharing tetrahedral defects corresponding to higher cooling rates [61] in simulated BKS glasses. Experimentally, Q5 silicon defects are not observed by magic angle spinning (MAS) NMR, and a 30 mol % Na_2O glass is found to consist of mostly Q3 species, with a lower proportion of Q4 silicons and a very low content (below 10%) of Q2 species [114, 117]. This supports the distribution predicted by Pedone potentials but is in disagreement with the prediction using BKS potentials.

The overall average network connectivity is 3.145 using Pedone potentials, 3.306 using BKS and 3.16 using Teter potentials; thus both Pedone and Teter compare favourably to a theoretical value of 3.143. The presence of edge-sharing tetrahedra predicted by the BKS potential is probably erroneous, and indicates a different distribution of alkali ions, leading to more Q4 and Q5 tetrahedra as well as more Q1 and even Q0 tetrahedra. These defects are associated with large clusters of sodium atoms, surrounding a dangling branch of the silica network.

The Pedone potentials seem to predict a structure in which most tetrahedra have only one NBO, best reflecting the current knowledge of glasses from magic-angle spinning (MAS) nuclear magnetic resonance (NMR) spectroscopy studies [118]. The BKS potential predicts a

fundamentally different structure, which conflicts with these experimental observations. The Pedone potentials seem to predict a structure in better agreement with experiment for these types of glasses.

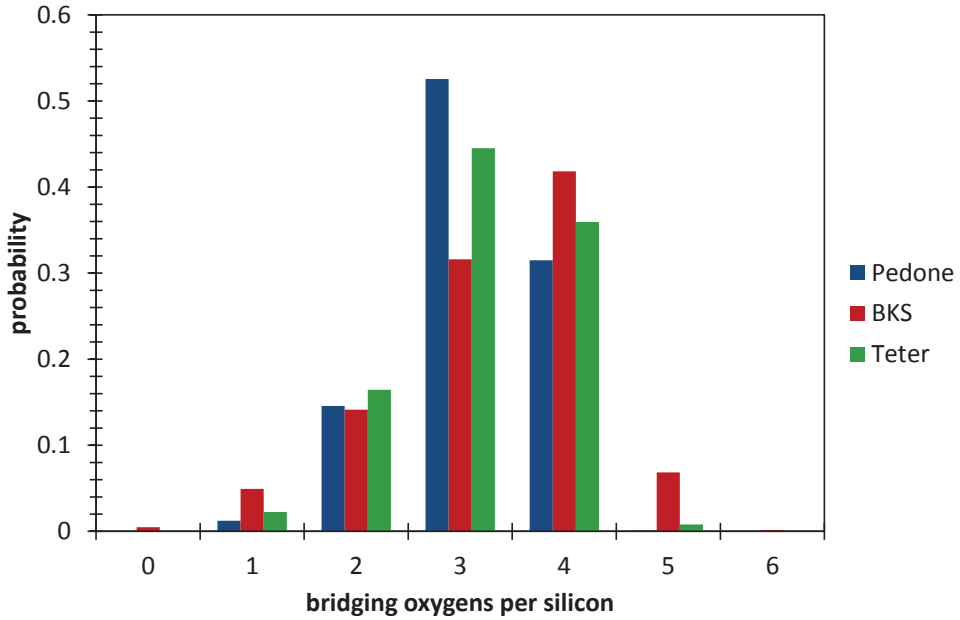

Figure 3.11 – Q speciation of Silicon for different potentials in a glass containing 30% Na_2O.

3.2.5 Ring Size Distribution

The network connectivity of the glass also influences another structural feature: the ring size distribution, which was calculated as described in section 2.9.3. It gives an impression of the "openness" of the glass structure, as larger rings may surround low density areas of the glass. Again, figure 3.12 shows the differences between the potential sets. The BKS distribution is shifted to the left, owing to the higher network connectivity and is another indication of a different distribution of alkalis throughout the glass. By comparison to simulations made using the Pedone potentials, Teter potentials predict ions showing a slightly larger variation in ring sizes than the other potentials (see figure 3.12), which may indicate more clustering of alkali ions, responsible for these large rings.

As will be discussed in the next section, radiation damage cascades may follow preferential

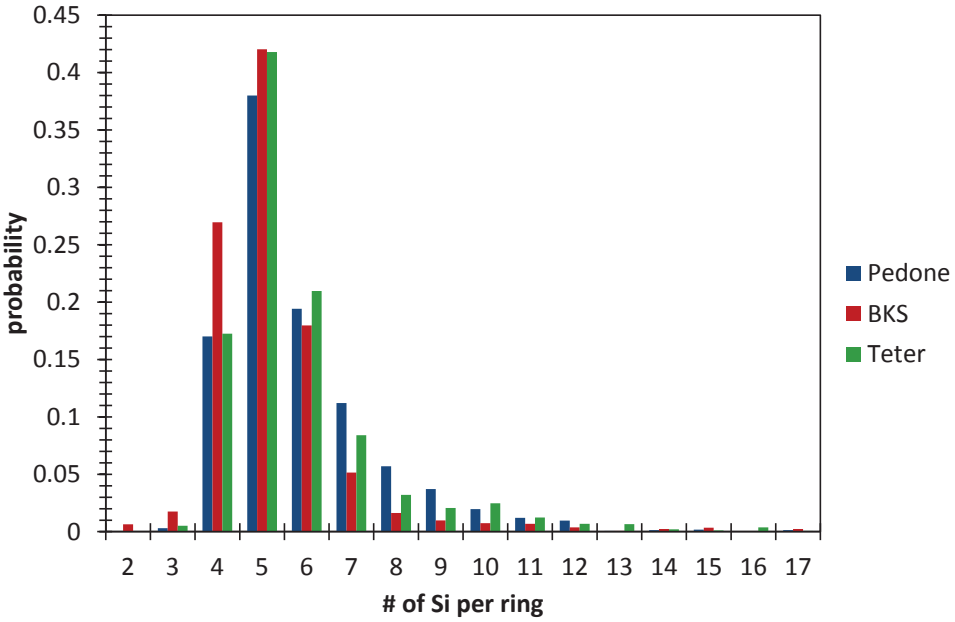

Figure 3.12 – Ring size distribution obtained by different potentials in a glass containing 30% Na_2O.

pathways through the structure, and most collisions occur with rigid areas of the glass network, involving a tight network of silica tetrahedra. Larger rings may be able to bend more easily, absorbing more energy before any bonds are broken. Equally, the spatial distribution of higher-than-average ring sizes may serve as an indication of paths and distances travelled by each PKA, as collision with the network could be responsible for smaller rings to be broken instead of larger and potentially more flexible rings.

Ring size analysis is a useful tool that can be utilised to predict and explain many of the network modifying and radiation damage effects occurring in glasses.

3.2.6 Predictive Quality of the Potentials

Several differences were observed between the potentials. For example, the BKS potential was the only potential to predict a number of defects, that manifested themselves in the O-Si-O bond angle distribution, network connectivity and the ring size distribution. The Pedone potential seemed to be the most consistent with theory and experiment and are repulsive at

low separations, which is required for radiation damage modelling where atoms can have high instantaneous energies. Nuclear repulsion can be incorporated into the BKS potential via a potential spline.

Given the good agreement with both glass theory and experiment, all of these potentials, and the Pedone potential in particular should be able to make good predictions on the influence of radiation damage and the resulting evolution of glass structure. As there is no turning point at close separations in the Pedone potential and the force at small separation is already very large, splining an additional repulsive term onto the potential was not deemed necessary.

3.3 Radiation Damage

The use of glasses as nuclear waste materials requires them to maintain their structure under repository conditions for thousands of years. These conditions include both the decay of radioactive elements within the glass matrix, as well as the elevated temperatures that these decays cause. As discussed previously, glasses are not in thermodynamic equilibrium due to their inherent entropy. This leads to the problem of devitrification by which the glass can lower its energy by becoming more and more crystalline. This process is limited only by kinetics, so that any process leading to an increase in the kinetic energies of the atoms within the glass (and hence the local temperature) accelerates the process of devitrification. Indeed, given sufficient time at elevated temperature there is a tendency for glasses to devitrify completely and become crystalline. Indeed, most glasses will crystallise if heated to a sufficiently high temperature [10].

Conversely, atomic displacements within glasses are likely to be less detrimental, as there are no interstitial or substitutional defects in amorphous structures and so healing of the network may be easier to achieve. It is therefore interesting to investigate the actual structural changes that are predicted to result from radiation damage.

3.3.1 Damage Modelling

Two primary radiation damage mechanisms exist: ionisation damage and damage due to nuclear collision. The source of this damage is primarily α-decay of incorporated elements. High energy α-particles produced by these events however, have such small mass, that they

will deposit the majority of their energy by ionisation, which is outside the scope of this model. The energy of α-decays is in the MeV range, with the majority of this energy associated with a high velocity α-particle. Despite this high overall energy, the low mass high speed α-particle does little local damage, due to the disparity in nuclear masses between the α-particle and the remaining ions in the glass. The overall displacive energy of this particle is thought to be as low as 6% of the overall displacive energy resulting from an α-decay [30], and is usually not modelled in MD studies of radiation damage [119–122]. The primary damage mechanism is then by elastic collisions originating from the much larger, heavier and slower α-recoil ion, even though it only has kinetic energy of about 100 keV. This recoil ion is the physical origin of the energy imparted to the primary knock-on atom (PKA), whose effects will be modelled hereafter.

Within a commercial HLW glass, approximately 10^{18} α-decay events per gram accumulate over the first 10 years of life [22]. This leads to a theoretical displacive energy of about 10^{20}keV per year per gram. In line with the primary knock-on atom technique (see section 2.8), only one atom initially carries all the additional kinetic energy. It transfers this energy in a series of elastic collisions, called a cascade. This is visualised in figure 3.13 (a). The high energy PKA is seen to quickly collide with a number of silicon and oxygen atoms. Just after this collision, only a very few atoms have been displaced by more than 5Å from their original positions, as shown in figure 3.13 (b). However, the kinetic energy is quickly dissipated in a series of further collisions, until eventually the recoil energy is spread throughout the system. The spread of this energy is not even however, as figure 3.13 (d) shows. Rather, each of the high energy recoil ions from the initial high energy collisions has transferred its energy to an area of the system in a series of sub-cascades. This leads to localised damage concentrated in high displacement density areas.

Delaye and Ghaleb investigated the morphology of these cascades using MD simulations, particularly the degree of polymerisation along the trajectory [119]. PKAs that meander through a highly de-polymerised sodium channel will cause less damage and lose less energy than when travelling through a highly polymerised, network former heavy region [119]. Most of the depolymerisation damage is, however, recovered within the first 5 ps, as has been shown in simulations of 16 keV cascades in silicate glasses [123].

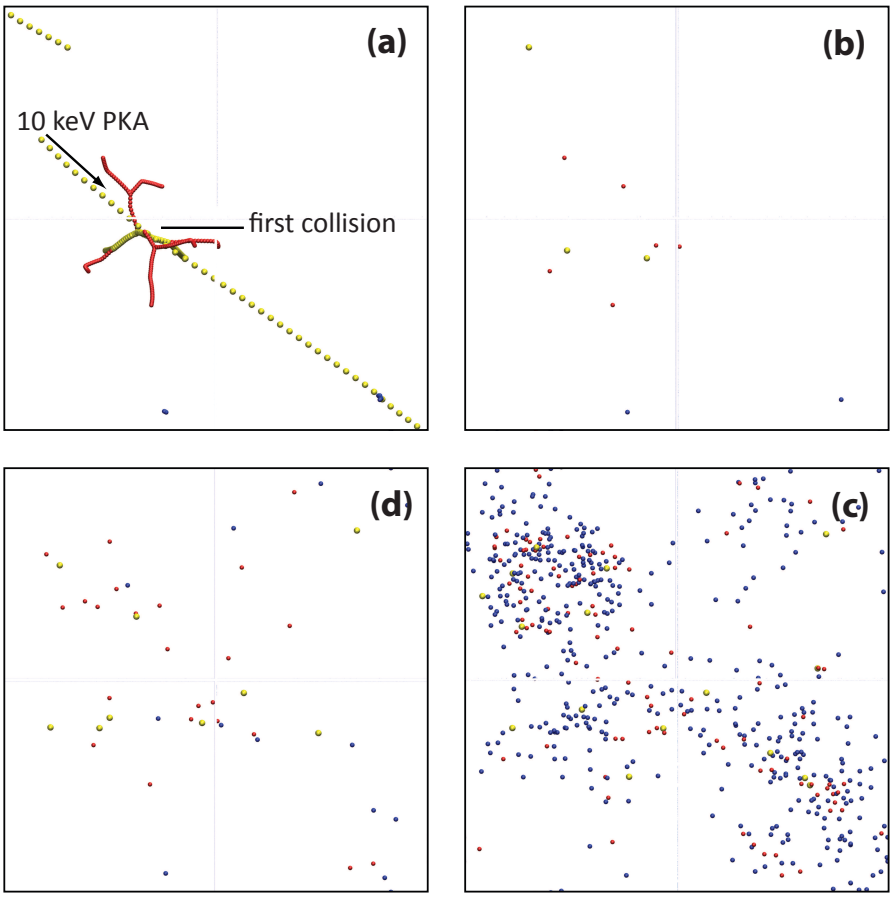

Figure 3.13 – The evolution of a 10 keV silicon cascade in $0.3Na_2O.0.7SiO_2$ glass showing only atoms that have been displaced by more than 5Å. The initial Silicon PKA impacts several other oxygen (red) and silicon (yellow) atoms and causes several secondary cascades over the first 50 timesteps (a), while the smaller sodium atoms (blue) are intially mostly unperturbed. This leads to a steady increase in the number of displacements, as seen after 50 timesteps (b), 100 timesteps (c) and 250 timesteps (d).

3.3.2 Radiation Damage Induced Volume Changes

Swelling is an effect that has been observed in nuclear waste glasses [22]. Swelling is the volume change that results from a number of simultaneous processes including thermal expansion, gas build-up, water uptake and structural changes within the material such as devitrification, which will form the basis of the following analysis.

As has been shown, the radiation damage caused by elastic collisions is highly localised. It is thus interesting to determine the effect on the bulk properties due to the localised damage. As seen in figure 3.14, the volume expansion is remarkably linear. It is to be expected that the rate of volume expansion will eventually decrease, given longer time intervals between cascades and higher irradiation doses, due to the limited number of NBOs that can be formed. Bureau *et al.* [124] observed this effect in their modelling of damage cascades in sodium borosilicate glass. The observed structural change included an increase in the number of 3-coordinated borons (as opposed to 4-coordinated borons), NBOs and percentage of network modifying sodium atoms with increasing irradiation energy. It should be noted that even without a prolonged annealing period the overall swelling in both cases is very small, suggesting good radiation resistance of the glass.

Table 3.5 – Volume changes observed for a 10 keV Silicon PKA without recovery. Potential cutoffs were chosen as 4.927Å for Pedone and 12.616Å for BKS potentials.

potential	irradiation energy	BKS		Pedone	
% Na_2O	keV g^{-1}	20	30	20	30
no. of cascades		% volume change			
none	0	0	0	0	0
1	3.723×10^{20}	0.00046	0.000925	0.001639	0.003224
10	3.723×10^{21}	0.00842	0.01532	0.030624	0.05021
20	7.446×10^{21}	0.01722	0.033374	0.062065	0.089405
50	1.861×10^{22}	0.04818	0.084594	0.173638	0.214464

Considering that the inflicted radiation damage is equivalent to a cumulated dose between 10 years for a single cascade and 100 000 years (10^{19} cumulative α-decays), the observed volume expansions are minimal, regardless of the potential used. The most profound effect observed, was the rise in system temperature from 500K to 1500K during the cascade. Whilst this will decline quickly during recovery, the temperature might decrease below the glass transition temperature before the reconstruction of the glass matrix is complete, resulting in residual

expansion.

Given the high energies that have been imparted on the system and the unphysically high dose, the actual effect on the bulk properties of the glass have been minimal. This underlines the effectiveness of glasses as a nuclear waste material.

3.3.3 Structural Changes

The change in atomic structure may not necessarily be represented in the bulk properties. To determine any radiation effects on the atomic structure, comparisons between the network connectivity and the ring sizes before and after damaging the glass are compared.

Figure 3.15 shows significant change in the distribution of Q species, which now assumes a more Gaussian shape. The network seems to be broken up, as is suggested by the increase in Q1 and Q2 species and the decline in Q3 and Q4 species. Overall network connectivity has dropped from 3.145 to 2.538 indicating significant depolymerisation of the glass network. This change in network connectivity has also affected the average ring size, which has increased from 5.85 to 7.99. The change in the ring size distribution (figure 3.16) shows that the most heavily affected rings are those of relatively short lengths containing 4 to 6 Si atoms each. These rings represent something structurally similar to silica's crystal polymorphs. This suggests that most of the collisions happened within the highly polymerised and thus stiffer parts of the glass, whereas those areas which had a more open ring structure, allowing more flexure, remained largely unaffected. Post irradiation, some very large rings exist, which is likely to indicate a change in the cluster morphology and the formation of larger alkali clusters, affecting alkali diffusivity. These large rings are, however, likely to disappear to some extent as the glass network re-polymerises during a period of recovery.

Despite the lack of change in the overall volume, the significant influx of energy leads to a distortion of the glass structure and a higher energy state. This increase in internal energy is facilitated by a less polymerised structure, with many NBOs being formed, leading to a lower network connectivity and substantially larger rings. This may have a significant detrimental effect on the immobilisation of some elements, leading to diffusion out of the glass host material. The high energy configurations may also lead to irreversible structural changes (such as nucleation and crystal growth) during the recovery period.

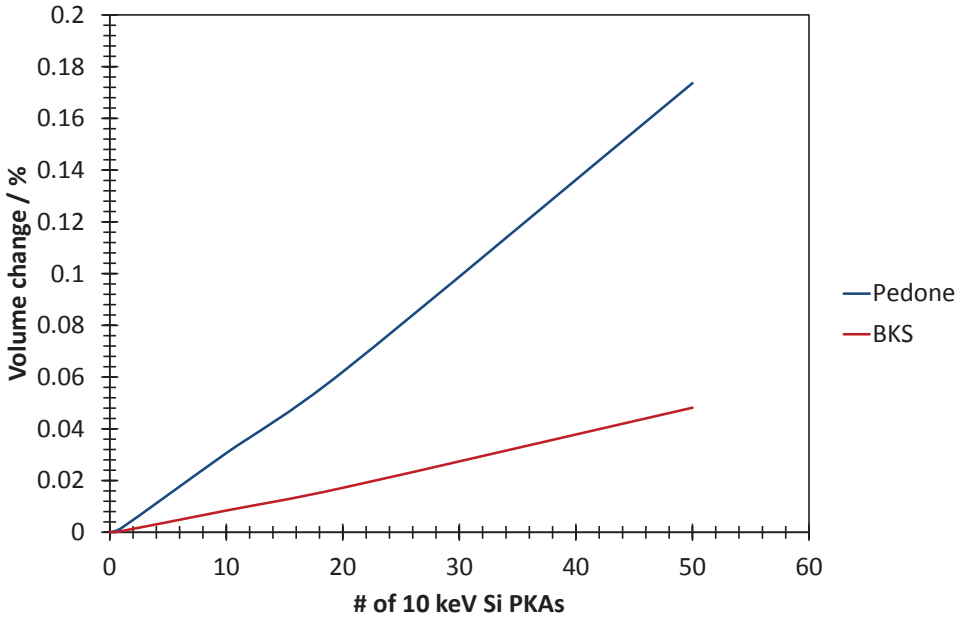

Figure 3.14 – Volume swelling of a $0.2Na_2O.0.8SiO_2$ glass impacted by 10 keV silicon PKAs.

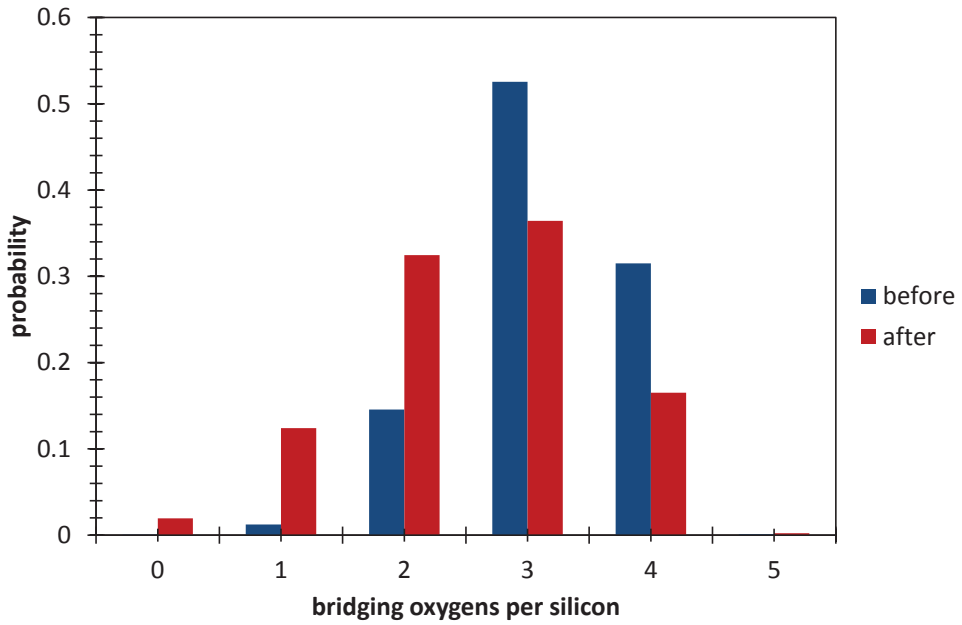

Figure 3.15 – Changes in Q speciation of silicon after 50 10 k eV cascades in a glass containing 30% Na_2O, modelled using the Pedone potentials [77].

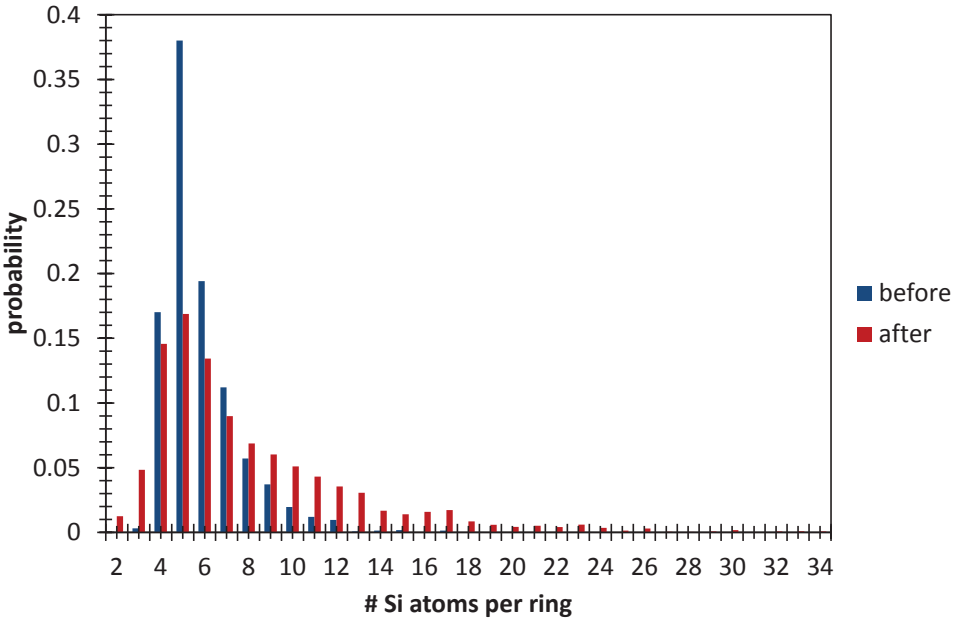

Figure 3.16 – Changes in the ring size distribution after 50 cascades of 10 k eV kinetic energy each in a glass containing 30% Na_2O, modelled using Pedone potentials [77].

4 Zinc in Nuclear Waste Glasses

The work in this chapter is based on the publication titled "Predicted Mechanism for Enhanced Durability in Zinc Containing Silicate Glasses" in the Journal of the American Ceramic Society [125].

A key aspect in the disposal of nuclear waste in general and high level waste (HLW) in particular, is the durability of the wasteform. The UK's current plan [23, 27] is calling for the permanent disposal of vitrified waste in a deep geological repository, as has been discussed earlier (see Section1.5). To ensure the long-term storage safety of the waste in such a repository, a number of natural and engineered barriers are to be put in place, which are necessary to prevent the release of radioactive elements from the repository. The barriers include the wasteform itself, the waste container, a metal overpack where appropriate, a buffer/backfill material (e.g. cement or clay) and the natural barrier (i.e. the bed rock). One of the major concerns in repository design is water and humidity ingress, as they can corrode or otherwise damage most of the protective materials [42].

Part of the reason why glasses are chosen as the host matrix and indeed for storage of any number of liquids and chemicals is their resistance to corrosion [42]. When dealing with timescales in the hundreds and thousands of years however, even glass corrosion becomes an issue, as glasses are thermodynamically metastable. This favours phase changes over long periods of time at elevated temperatures. The metal containers are designed with eventual failure in mind, meaning that the final engineered barrier in a repository is the waste host material itself. In order to minimise the leeching of radionuclides into the environment, it is important to optimise the glass' resistance to water corrosion [105]. This resistance is also called *glass durability* [10]. The following chapter explains how and why replacing some of the silicon oxide in the current glass composition with zinc oxide can improve glass durability by causing fundamental structural changes in the glass.

4.1 Zinc Oxide Addition to Glasses

Zinc oxide is sometimes used in glass making as it reduces the coeffient of thermal expansion that improves resistance to thermal and mechanical shock [10]. It also has a high refractive index, which makes it important in optical glasses, or as an additive to improve the colour

and clarity of glasses in general [10]. It's high refractive index can also be used to enable the glass to act as an opacifier [126].

4.1.1 Zinc Oxide Crystal Structure

Zinc oxide occurs naturally as a mineral, usually in the hexagonal Wurtzite structure (figure 4.1). An alternative form of zinc oxide is found in the zincblende structure (figure 4.2). In both cases, the Zn ions are coordinated by four oxygen ions with which covalent bonds are formed in a tetrahedral structure. The tetrahedral structure in both structures is a result of sp^3 hybridisation [127], as Zn only has two valence electrons. At high pressures of about 10 GPa, it is also possible to crystallise ZnO in the rocksalt structure [128] (figure 4.3), where zinc centres are found in octahedra [127]. Due to the polar nature of the Zn-O bond, the planes of zinc and oxygen ions are charged. Unlike other materials, this effect is not compensated for by a surface reconstruction [129].

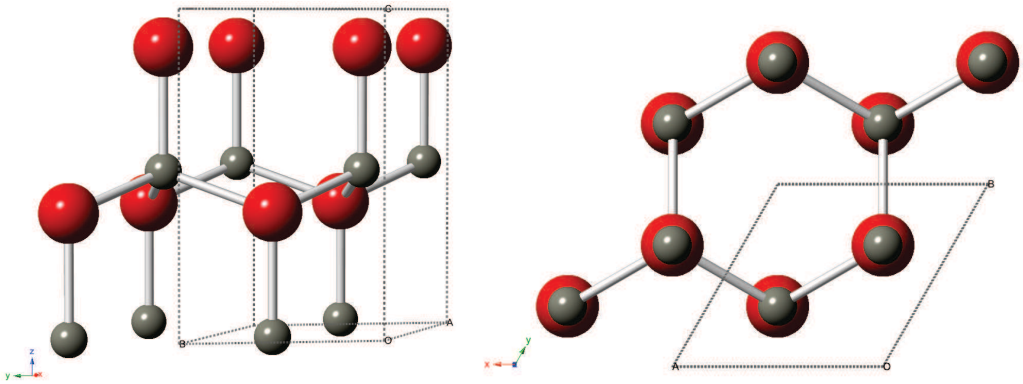

Figure 4.1 – The hexagonal ZnO Wurtzite structure, where oxygen is shown in red and zinc in grey.

4.1.2 The Glass Forming Role of ZnO

The exact role performed by ZnO in the glass is a point of continuous contention. One approach to determining the role of an oxide in glass formation is to consider the relative strengths of the cation-oxygen bond. Dietzel's field strength criterion [130, 131] estimates the bond energy based on the valency of both cation and anion and the ionic radii of the two. If the bond has high energy, it is indicative of a glass former, whilst bonds of lower or very low energy are defined as glass modifiers or intermediates respectively. The field strength of

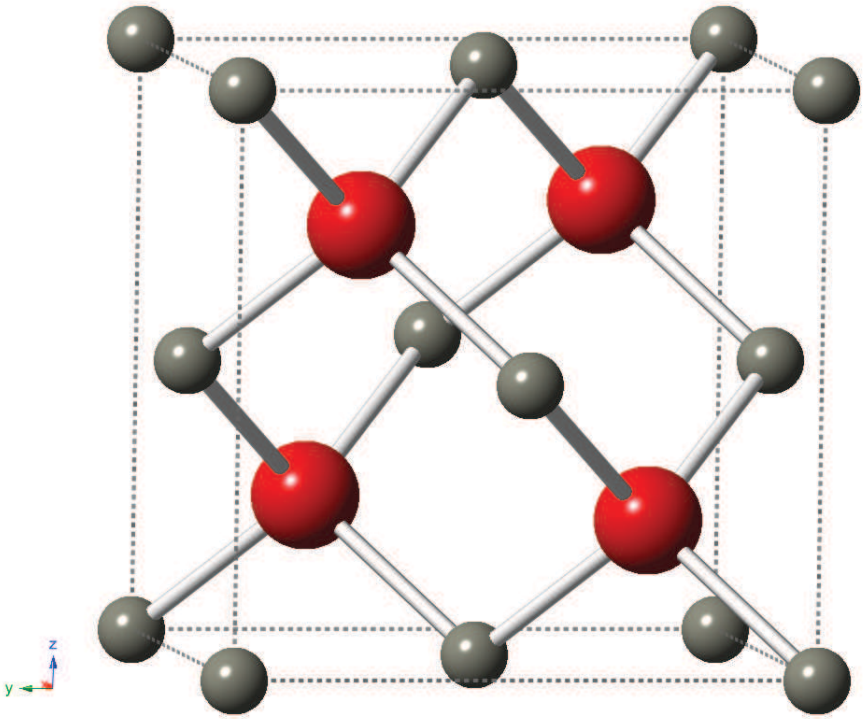

Figure 4.2 – The ZnO zincblende structure, where oxygen is shown in red and zinc in grey.

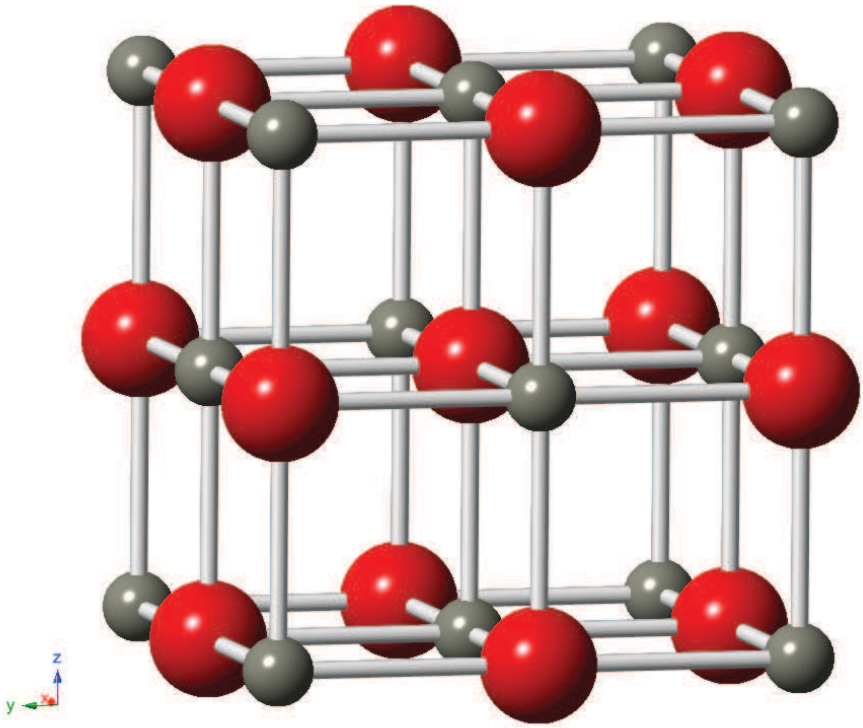

Figure 4.3 – ZnO in the rocksalt structure, where oxygen is shown in red and zinc in grey.

a cation is related to the Direct Coulomb interaction [66] and given by [130]:

$$F = \frac{z_c}{(r_c + r_a)^2} \tag{26}$$

where z_c is the valency of the cation (e.g. zinc) and r_c and r_a are the ionic radii (in Å) of the cation and anion (oxygen) respectively. Using the ionic radii provided by Shannon [132], the field strengths of the various oxides present in the glasses to be examined can be calculated and are shown in Table 4.1. The field strength (see equation 26) is typically given as a unitless number that roughly correlates to the role of the oxide in the glass as follows [133]:

- Glass Formers: field strength > 1.3
- Glass Modifiers: field strength < 0.4
- Intermediates: 0.4 ≤ field strength ≤ 1.3

Table 4.1 – Dietzel Field Strengths of Relevant Glass Oxides based on ionic radii by Shannon [132].

Oxide	Cation			Anion			Field Strength
	Type	C.N.	r_c [132] / Å	Type	C.N.	r_a [132] / Å	$z_c/(r_c+r_a)^2$
SiO_2	Si^{4+}	IV	0.26	O^{2-}	II	1.35	1.54
ZnO (tetrahedral)	Zn^{2+}	IV	0.6	O^{2-}	IV	1.38	0.51
ZnO (octahedral)	Zn^{2+}	VI	0.74	O^{2-}	VI	1.4	0.44
Na_2O	Na^{+}	IV	0.99	O^{2-}	VIII	1.42	0.17

Based on the Dietzel field strength model and the values presented in table 4.1, ZnO falls into the range of a network intermediate, both in its tetrahedral as well as in octahedral form. It should be noted however, that the strict coordination numbers provided here closely match crystals, but that coordination numbers in glasses can differ greatly between sites. Further, a comparison of field strengths can provide some indication into the structural effect of any intermediates present, whose role may change depending on what other oxides are present. While the Dietzel field strength model gives an indication, other opinions as to the role of ZnO in the glass exist. Nelson [134] argues that ZnO in silicate glasses acts as *"a quasi-molecular*

complex in which the transition metal ion is coordinated by non-bridging oxygens and which may result in local rearrangement of the glass structure". He distinguishes this from a classic network former role in that there is no substitution into network sites and no polymerisation of transition metal polyhedra in general. Minser [135] on the other hand claims that ZnO is simply a network modifier, based on his observations from Raman spectroscopy. Clearly, the issue of role of ZnO is a sensitive one, and is likely to be highly dependent on the composition.

4.1.3 Durability Changes due to Zinc Addition

A number of experimental studies have been performed to study the effect of ZnO on a wide range of glass compositions and in a variety of applications [47, 136–141]. The focus of most of these studies has been to determine the effect ZnO has on the corrosion rates of glasses. Several tests were performed by British Nuclear Fuels Limited where ZnO was added to the complex British waste glass composition (a 25 wt% waste loaded borosilicate glass composition) [140, 142]. Ramshaw *et al.* [142] note that whilst a replacement of only 1 wt% SiO_2 with ZnO was enough to reduce devitrification in the nuclear glass, more than 8 wt% can lead to phase separation in borosilicate glasses. In a test using the same processing conditions and temperatures as are used in the UK for waste vitrification, a replacement of only 3 wt% ZnO for SiO_2 in the waste glass composition led to a decrease in leach rates, particularly in the hazardous elements Mo and Cs [142]. To avoid phase separation whilst maximising the benefits, ZnO is often added alongside CaO, which has a similar effect on the glass [140]. A big incentive to investigate the use of Zn in the nuclear waste industry in particular, is that the addition of ZnO lowers the viscosity of the glass and increased the melter yield by up to 5 % [140]. This provides two major benefits in addition to the expected durability improvement:

1. The increase in yield indicates that more of the calcined powder is molten and dissolves into the fluid. This is important, as the undissolved radioactive solids otherwise gather at the bottom of the melters and need to be removed periodically and disposed of separately [18].

2. The replacement of 8 wt% SiO_2 with 2 wt% CaO and 6 wt% ZnO led to a significant decrease in the viscosity of the glass, which should allow for a lowering of the processing

temperature by 65 to 140 °C [140].

In addition to the benefits of enhanced durability of the waste product, the lowering of the processing temperatures is expected to decrease the corrosion rates associated with the melter crucible [140]. The potential benefits of adding ZnO to silicate glasses in general and to nuclear waste glasses in particular are an enhancement in corrosion resistance and a potential reduction in the processing temperatures due to a decrease in melt viscosity.

Cassingham *et al. [47]* investigated the structure of simplified nuclear waste glasses with added ZnO by x-ray absorption spectroscopy. Their data shows that ZnO, in the composition on which the following MD study is based (70 mol% SiO_2, 10 mol% ZnO and 20 mol% Na_2O), occurs in four-fold coordination. This conclusion was reached after comparison of x-ray absorption near-edge structure analysis (XANES) data of various glass compositions with hemimorphite ($Zn_4Si_2O_7(OH)_2{\cdot}H_2O$) in which Zn assumes a tetrahedral coordination with oxygen. Further, it was observed that ZnO_4 tetrahedra are participating in network formation and linked to nearby SiO_4 tetrahedra. While this represents a significant improvement in understanding the behaviour of Zn in silicate glasses, it does not provide an explanation for the enhanced durability behaviour observed, giving rise to the MD study presented in this chapter.

4.2 Model Zinc Glass Structure

In order to understand the change in durability in zinc-containing glasses, the first step is to establish any differences between the glasses on a molecular level, before analysing their effect on the material properties. In the following discussion we will compare the structure and properties of a sodosilicate glass with a zinc-containing glass, in which 10 mol% SiO_2 have been replaced with 10 mol% ZnO. The typical structure of a sodosilicate glass illustrated in figure 4.4 and has been obtained by performing a model melt-quench from 5300 K (see Chapter 2 for details of this procedure). The composition of the simpler sodosilicate glass is 80 mol% SiO_2 and 20 mol% Na_2O. In order to assess how Zn affects the structure, another zinc-containing glass of composition 70 mol% SiO_2, 10 mol% ZnO and 20 mol% Na_2O was prepared by the same method presented in chapter 2 and is shown in figure 4.5.

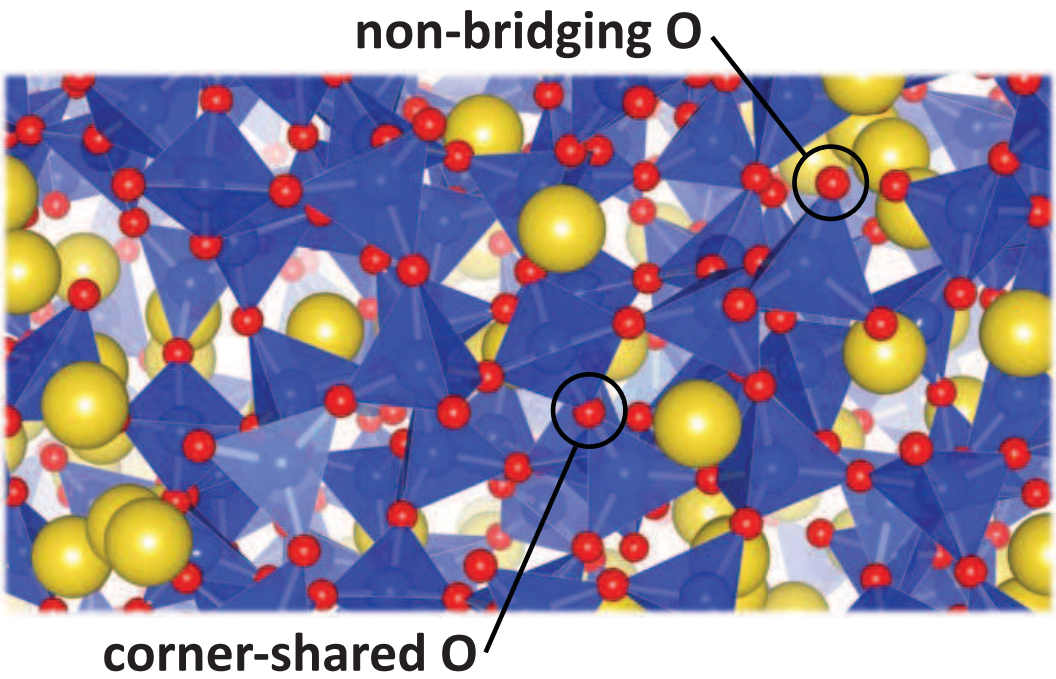

Figure 4.4 – Modelled sodium silicate glass with 20 mol% Na_2O. Si shown in blue, O in red, and Na in yellow.

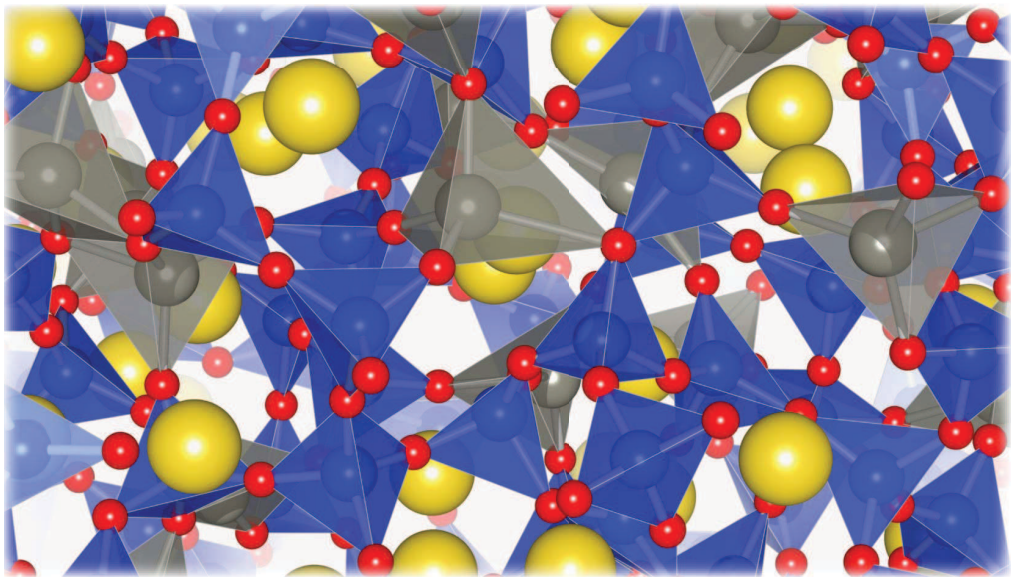

Figure 4.5 – Modelled zinc sodium silicate glass with 10 mol% ZnO and 20 mol% Na_2O. Si shown in blue, Zn shown in grey, O in red, and Na in yellow.

4.2.1 Modelling of the Glass

The glasses were generated from an 8000 atom melt-quench using the potentials formulated by Pedone *et al.* [77,143], which are tabulated in table 2.3. During each step of the quench, the volume and temperature are constrained (NVT ensemble) to match the experimental sodium silicate glass density of $3.383\,\mathrm{g\,cm^{-3}}$ [110]. The glass was then cooled in steps of 500 K with 50 ps of simulation time for each temperature and a timestep of 2 fs with the Berendsen thermostat [94]. The final equilibration run at 300 K was performed in the microcanonical ensemble (NVE), where 200 ps of dynamics with a Nosé-Hoover thermostat [95,144] (10 ps relaxation time) were performed.

Despite extended equilibration times of 50 ps at each step of the quench, the net potential energy of the glass was still fluctuating at room temperature, suggesting a structure which is not well equilibrated. This is not surprising, given that the quench time in the simulation is about 10^{12} times faster than in a real quench [61] owing to computational limitations. The end result could suggest a higher fictive temperature to which the glass structure corresponds. In other words, an unphysical high-temperature glass structure is frozen and kinetically stabilised at room temperature. In order to remove this effect, an additional set of simulations was performed: the temperature was increased to 1800 K in the constant pressure ensemble (NPT) by increasing the temperature in steps of 50 K, with 100 ps of dynamics at each temperature. Afterwards the temperature was brought back down to 300 K at the same rate. By releasing the volume restraint, which was necessary to facilitate the fast quench given computational limitations, the glass is allowed to re-equilibrate. The temperature of 1800 K was chosen to raise the temperature of the glass above the glass transition temperature (about 1500 K in fused quartz and significantly lower with added modifiers [110]). Above the glass transition temperature, the glass turns into a viscous material, where the high vibrational energy allows the silica chains in the glass to slip past one another, allowing for a reduction in the total energy of the system.

This repeated heating and cooling cycle led to a convergence of initial and final volume of the glass and the total potential energy of the system decreased, confirming permanent changes in the structure. The volume changed with temperature for consecutive cycles, until the difference between the initial and final volume was negligible (less than 0.1 %). The final densities

obtained after the cycling procedures were 2.38 and 2.59 g cm^{-3} for the sodosilicate and zinc sodosilicate glasses respectively, which compares well to the experimental values of 2.38 and 2.62 g cm^{-3}.

4.2.2 Structure of the Glass

The simulated structures of the sodium silicate glass composition and the zinc-containing glass are shown in figures 4.4 and 4.5 respectively. Just as in the standard sodium silicate glass, the network in the zinc-containing glass is made up of corner-sharing SiO_4 tetrahedra, linked together by bridging oxygens (BOs), with some non-bridging oxygens (NBOs) present due to sodium acting as the network modifier. Interestingly, the Zn ions readily incorporate themselves into the glass networks by forming ZnO_4 tetrahedra, linked to other zinc and silicon tetrahedra. Figure 4.5 further shows, that on average, the zinc tetrahedra are slightly larger than their silicon counterparts, due to the difference in Zn-O and Si-O bond lengths. This effect can be quantified by comparing the average volumes of SiO_4 and ZnO_4 tetrahedra, defined by the positions of surrounding oxygen ions, which are 0.497 Å^3 and 0.913 Å^3 respectively. The net effect of this difference in size appears to be a small distortion of the glass network in the vicinity of zinc tetrahedra.

The pair distribution function (PDF, see section 2.9.1) of the ions present in both simulated glasses is shown in figure 4.6 and gives a more quantitative description of the structure, particularly for the first coordination sphere. The PDF in this case is simply a standard radial distribution function of the form:

$$g(r) = \frac{dn(r)}{4\pi\rho_0 r^2 \delta r} \tag{27}$$

where $g(r)$ is the radial distribution function describing the probability of a pair of atoms being found at separation r, ρ_0 is the average number density of the system, δr is the bin size (i.e. the thickness of the shell between r and $(r + \delta r)$) and $dn(r)$ is the number of atoms found in that shell. The PDF describes a relative probability of different interatomic distances for a given set of ions. For example, a g(r) of 4 for a given distance means that it is four times more

likely to find a pair of ions at this separation than in a homogeneous distribution with the same density. Consequently, the bigger and more defined the spikes in a PDF are, the more ordered the material is. Most crystals thus have very defined peaks, even at longer distances, whilst glasses tend to have very broad peaks and approach the average (a value of 1) much faster for larger separations, due to the lack of long-range ordering.

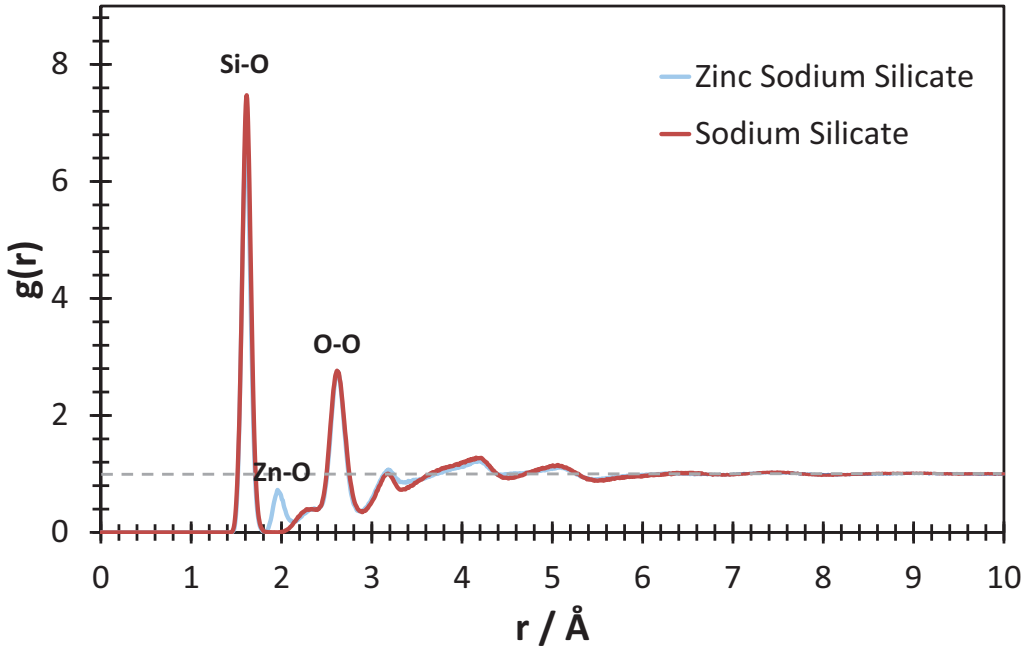

Figure 4.6 – PDFs of the sodium silicate (red) and zinc sodium silicate (blue) glass compositions.

When analysing the PDF shown in figure 4.6, it is found that the largest peak in both glasses occurs at 1.617 Å due to the Si-O bond. This value is close to the experimental Si-O bond length of 1.625 Å, obtained from neutron scattering data by Zotov *et al.* [145] for a glass of the same composition. Interestingly, the size and shape of the Si-O peak is almost identical in both glasses. Thus, the addition of ZnO does not appear to have a noticable effect on the first coordination shell of Si-O. The second major peak in the sodium silicate base glass corresponds to the O-O bond length at 2.61Å. Additionally, a Zn-O peak is seen at 1.96 Å in the zinc-containing composition. A bond-length of 1.95 Å has been observed experimentally for tetrahedral ZnO_4 in the same composition [47]. The O-O peaks are also identical between the two glasses, indicating that ZnO assumes the same role and a very similar tetrahedral configuration in the glass as the main network former SiO_2. Figure 4.5 shows how ZnO_4 tetrahedra are incorporated into the network of linked SiO_4 tetrahedra. As a network intermediate [24],

zinc has the ability to act both as a network former or network modifier, dependent upon composition [25]. For the composition considered here, tetrahedral coordination, indicative of a network former, is found throughout the structure. None of the zinc ions were found to have six-fold coordination, which is more indicative of a network modifier. A look at the partial PDFs for each pair of ions, as shown in figure 4.7 reveals that the main differences between the two glasses appear to be in interactions involving Na, or otherwise past the first coordination shell. The data gathered from these partial interactions and experimental values from the literature are summarised in Table 4.2.

Table 4.2 – Simulated Glass Structures at 300 K. Average bond lengths given in Å and angles in degrees.

	Units	Base Glass		Zinc Glass	
		sim.	expt.	sim.	expt.
ρ	$g\,cm^{-3}$	2.38	2.38[a]	2.59	2.62[e]
r_{Si-O}	Å	1.617	1.625[b]	1.616	1.62[c]
r_{Si-NBO}	Å	1.559	1.589[b]	1.561	-
r_{Si-BO}	Å	1.625	1.650[b]	1.619	1.58–1.63[c]
r_{Zn-O}	Å	-	-	1.969	1.95[d]
r_{Na-O}	Å	2.30*	2.45[b]	2.30*	2.4–3.4[c]
r_{Na-Na}	Å	3.00*	3.42[b]	3.05*	-

* position of first peak is given instead of an average bond length
[a] Reference [110]
[b] Data from Zotov and Keppler [145]
[c] Data from Hesse *et al.* for crystalline $Na_2ZnSi_3O_8$, in which all oxygen atoms are bridging [146]
[d] Data from Cassingham *et al. [47]*
[e] Estimate based on empirical model by Fluegel [147]

The PDFs revealed that some notable structural changes seem to be occuring in the mid-range, beyond the first coordination shell of the ions. In this region, the distribution and network structure of the tetrahedral base units of the glass are defined. Figure 4.8 shows how three individual ion pairs make up the convoluted first peak in the zinc sodium silicate glass. The Zn-Zn peak is small compared to both the Si-Si and the Si-Zn peaks. This can be explained by the different number of valence electrons in Zn ions compared with Si. When Si^{4+} is surrounded by four bridging O^{2-}, each oxygen ion is contributing one electron to its bond with the central Si ion, establishing charge balance. A Zn^{2+} ion on the other hand will lead to a net charge of 2- on the tetrahedral unit. This necessitates Na ions near the zinc tetrahedra to

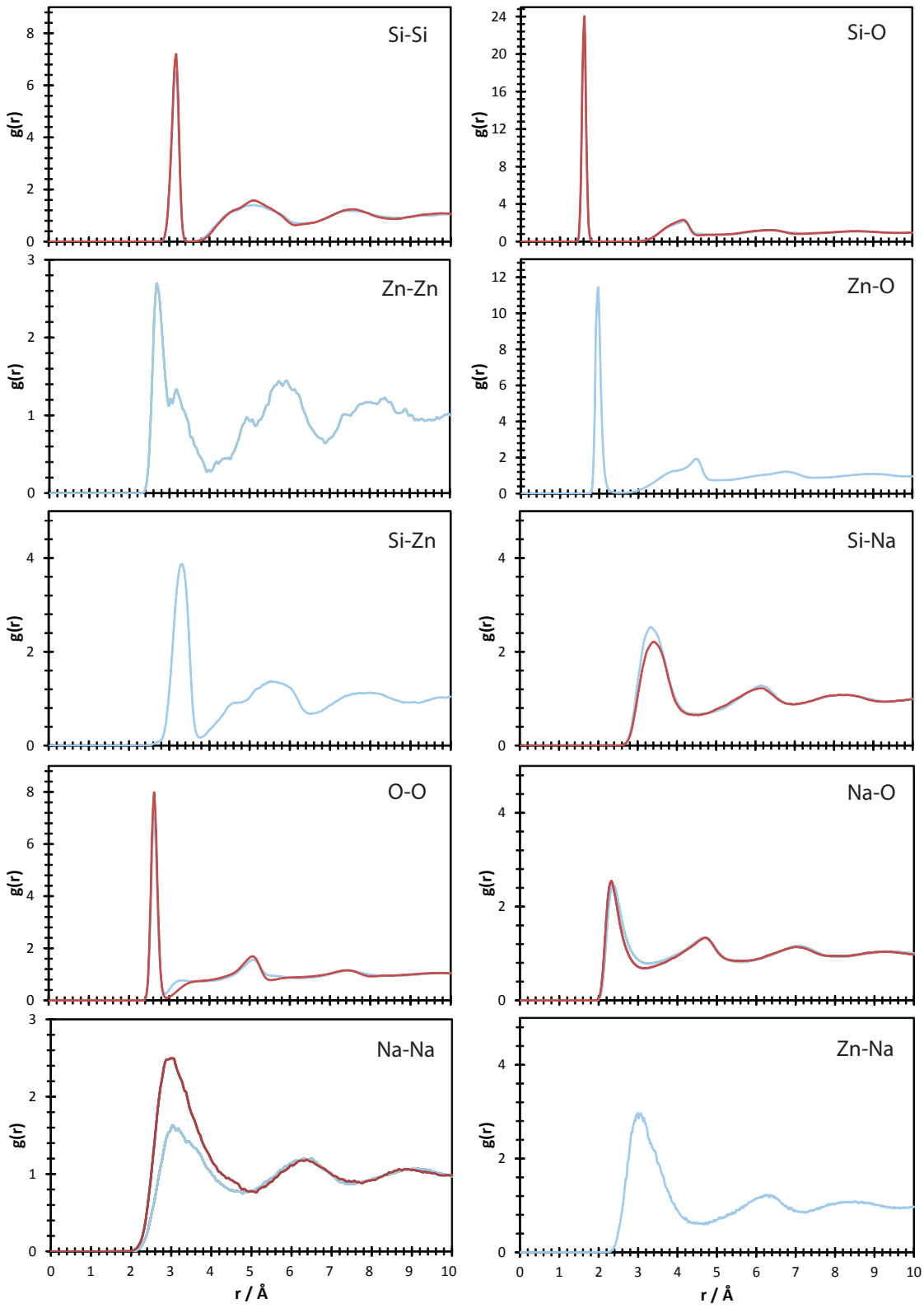

Figure 4.7 – Partial PDFs of the simulated sodium silicate (red) and zinc sodium silicate (blue) glasses.

act as charge balancers, and also means that it is energetically unfavourable for Zn ions to be in close proximity, even if all oxygen ions are bridging and thus only contribute half their charge. The effect of this repulsion is that the Zn ions are spread out throughout the glass, separated by SiO_4 tetrahedra, leading to the notable Zn-Si peak. Another, less favourable mechanism of overcoming the charge problem of ZnO_4 tetrahedra is the formation of edge-sharing Zn ions, where two O ions are shared between two Zn ions, instead of just one as in corner-sharing. These edge-sharing O ions are, however, still bridging to other tetrahedra though (usually SiO_4), which means that the net charge of an edge-sharing Zn_2O_6 unit is only 2- compared to 4- in a corner-sharing Zn_2O_7 unit. This makes it easy for edge-sharing zinc tetrahedra to be charge-balanced by a single Na ion, when two would be necessary in corner sharing. The preference for edge-sharing zinc tetrahedra means that the dominant edge-sharing peak Zn-Zn separation is only 2.7 Å followed by a secondary corner-sharing peak at about 3.2 Å. This compares to about 3.1 Å for the (corner-sharing) Si-Si bond.

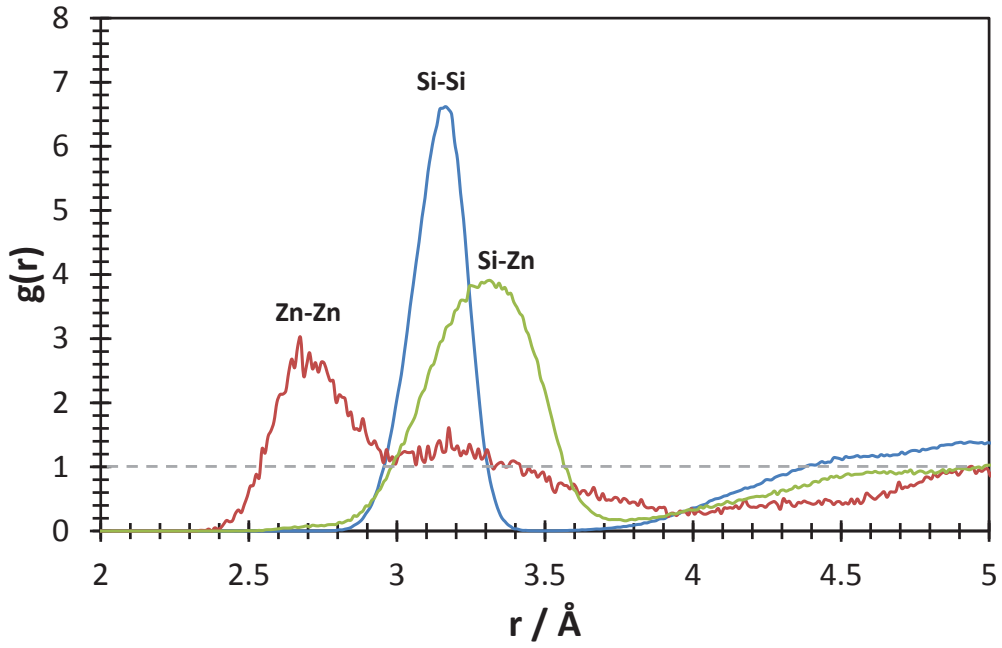

Figure 4.8 – PDFs of the convoluted peak seen in figure 4.6 at 3.2 Å for the zinc sodium silicate glass.

The net charge on zinc tetrahedra also inhibits the formation of NBOs in zinc tetrahedra, as this would lead to additional Na ions having to be in close proximity of the Zn ions for charge-balancing purposes. This effect is shown in the Q(n) distribution, which is a measure of the number of bridging oxygen ions surrounding each network former (i.e. Si and Zn ions)

within a given cutoff distance [133]. A perfect silicate structure (whether glass or crystalline) should therefore be expected to be made up of only Q4 tetrahedra (i.e. a four-coordinated Si, surrounded by only BO). Table 4.3 shows the coordination environment for a cutoff at 2.6 Å from the network-forming ion. This cutoff value was chosen to be at the minimum between the first and second coordination shell in the PDF (shown in figure 4.6).

Table 4.3 – Q(n) speciation of Si in the two simulated glasses. A cutoff value of 2.6Å was used in each case. Q(n) of Zn is given in brackets.

	Base Glass / %	Zinc Glass / %	Base Glass (Expt.)* / %
Q1	0.23	0	0
Q2	6.24	1.77 (0)	3
Q3	36.7	22.0 (5.50)	48
Q4	56.6	76.3 (91.5)	50
Q5	0.28	0 (3.00)	0

* Experimental NMR data, see [117]

Most of the Si ions in both glasses are either in Q3 or Q4 coordination. In the zinc-containing glass however, a shift is seen towards a more polymerised network as the Q4 fraction increases relative to the base glass whilst Q2 and Q3 fractions decrease accordingly. While oxygen ions are shared between four tetrahedra in crystalline ZnO, they are only ever shared between two tetrahedra or not shared at all in the glass. As SiO_2 contains twice as many O ions per mole as ZnO does, the replacement of SiO_2 with ZnO will reduce the amount of O ions available per tetrahedron. ZnO as a network intermediate oxide thus acts in the opposite way to adding an alkaline network modifier such as Na_2O and decreases the oxygen to network former ratio rather than increasing it.

The rate-determining factor in the steady-step corrosion of glasses is the dissolution of the polymerised network [48] and thus the breaking of Si-O and Zn-O bonds. Other factors being equal, glass containing fully corner-sharing Q4 tetrahedra is expected to be more corrosion resistant, as more bonds need to be broken to fully dissolve the network. The local bonding environment of the network formers, is however not the only factor which affects corrosion resistance. Effects occurring in the intermediate-range structure also need to be considered. The distribution of alkali can play an important role here, through the formation of alkali clusters or channels [22].

4.3 Effects on Alkali Clustering

The ring size distribution is a common metric which helps in the analysis of the intermediate-range structure [10,99]. The ring size analysis method and the metric applied here has already been discussed previously in section 2.9.3. The smallest ring formed by each tetrahedron is presented in figure 4.9. The modified random network theory [103] (see chapter 3.1) predicts large rings of network formers encompassing areas of high alkali concentration, due to an uneven distribution of alkali ions into channels and clusters. It can therefore be expected that the apparent shift towards smaller ring sizes upon zinc addition coincides with a different distribution of alkali ions in the glass. An attempt of visualising this effect was made in figure 4.10, where the alkali ions appear to be more evenly spread throughout a zinc containing glass compared to the base glass. Although both glasses contain 20 mol% Na_2O, the base glass features a large network of sodium channels, where local clusters of Na ions commensurate with large rings containing six or more tetrahedra. By comparison, the distribution of sodium ions is more homogeneous in the zinc-containing glass, leading to smaller ring sizes. As this is a purely visual and qualitative analysis, a quantitative analysis is necessary and provided hereafter.

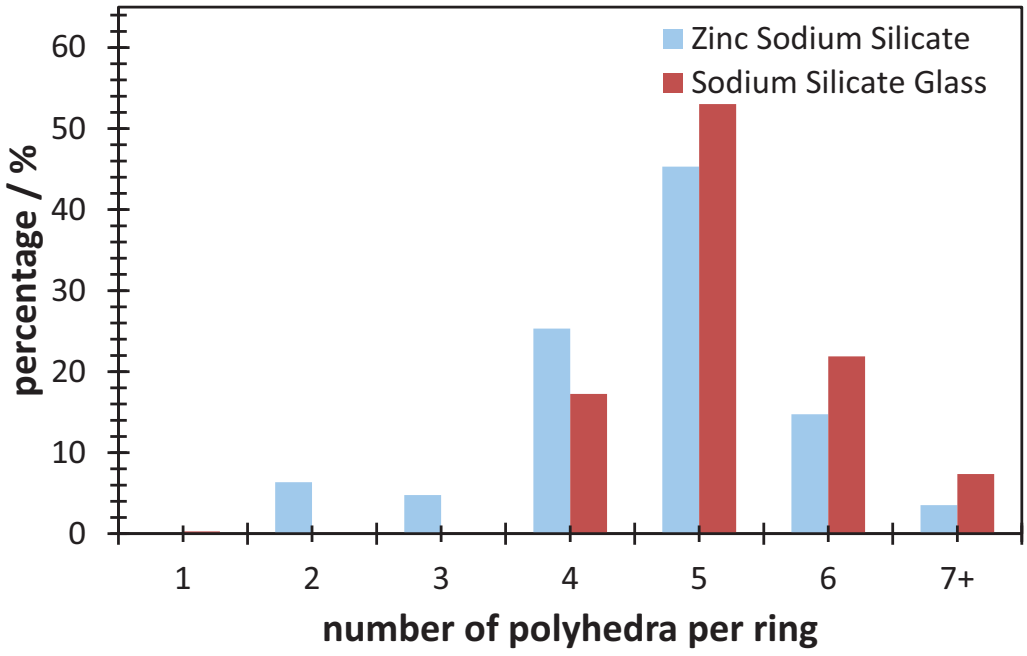

Figure 4.9 – Ring size distribution showing a higher proportion of large rings in the sodium silicate glass (red) compared to the zinc sodium silicate (blue) glass.

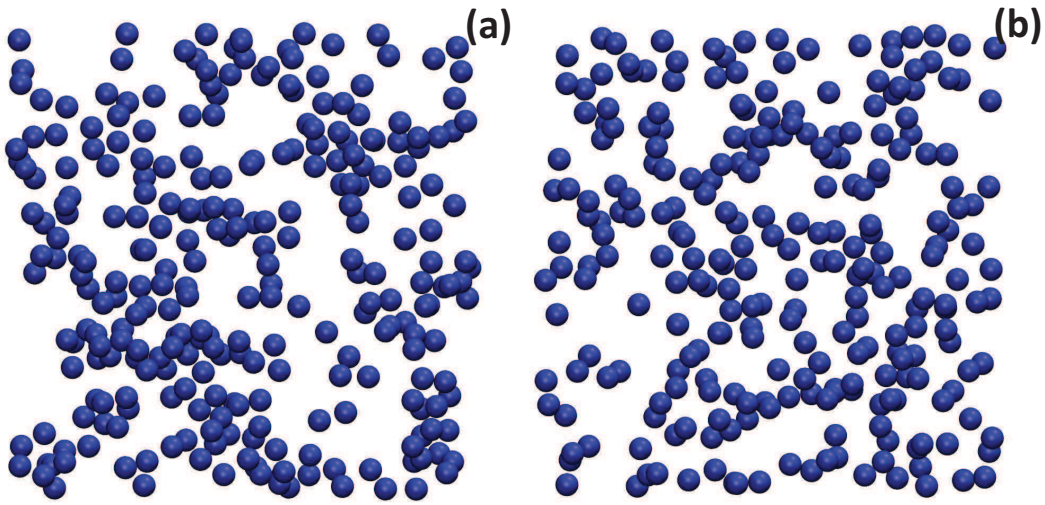

Figure 4.10 – 12Å thick slices through the simulation boxes of sodium silicate glass (a) and zinc sodium silicate glass (b), showing the distribution of an equal proportion of sodium atoms.

4.3.1 Defining Clusters

The Na-Na PDF (see figure 4.7) reveals that there is a lower probability for sodium ions to be in close proximity in a zinc containing glass. In order to further assess the changes to the aggregation of Na effected by the addition of ZnO to the glass composition, the Na cluster sizes in both glasses need to be measured. A cluster is defined as a contiguous set of atoms where each atom is within a fixed cutoff distance of another atom of that type within the set. A graphical represention of this algorithm is seen inset into figure 4.11: six points representing alkali atoms have overlapping cutoffs and are therefore defined as a cluster (outlined in blue); the additional single point on the other hand lies outside the cutoff of the clustered atoms and is therefore defined as isolated. As the results of this method are sensitive to the cutoff distance chosen, there may be a level of ambiguity in the obtained cluster sizes. It is therefore necessary to conduct a sensitivity analysis in which this effect is considered; for each of the glasses figure 4.11 shows the fraction of Na atoms within the largest cluster versus the cutoff distance used in the cluster size calculation. Choosing a sensible cutoff is important, as a cutoff that is too small leads to all Na ions to be considered isolated, because the first Na-Na peak in the PDF is not sampled. It might be appealing to pick a cutoff coincident with the first minimum after the first coordination peak in the Na-Na distribution. Such a cutoff length (~5 Å) is too long however, as all Na atoms are then included in a single cluster, disregarding situations

where Na atoms are separated by a chain of network formers. It follows that neither extreme is representative of the physical reality of Na clustering in these glasses. Consequently, the Na cluster sizes need to be used for a primarily qualitative comparison of Na aggregation in zinc and not zinc-bearing glasses. Figure 4.11 nevertheless shows a very consistent trend in the range between 3 and 5 Å; the largest cluster within the base glass composition is always larger than in the zinc sodium silicate glass. This further supports the hypothesis of a more homogeneous Na distribution with a lower degree of clustering when ZnO is added to the glass composition.

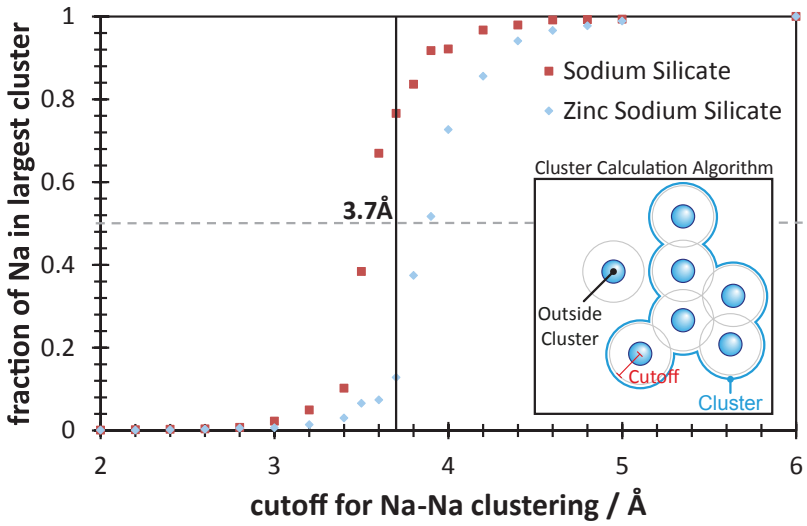

Figure 4.11 – Na-Na cutoff sensitivity on the size of the largest cluster observed in the glass.

The cutoff was chosen at 3.7 Å, where the difference between the base glass and the zinc sodium silicate curves in figure 4.11 is greatest. We can use this cutoff to establish the clustering environment of Na ions by counting the number of immediate Na neighbours, as presented in Fig 4.12. From a theoretical standpoint, for a three-dimensional cluster to exist, there need to be Na ions with more than two neighbouring Na ions. Conversely, two neighbours would indicate a string or channel, while a single neighbour would indicate either an isolated pair or the end of a string of atoms. The conformation of the modifier network is important for the diffusion dynamics. The dominant migration mechanism for alkali ions in many glasses is that of concerted hopping of a number of adjecent atoms [104, 148]. In these glasses, a path or channel of adjacent alkali ions is required for migration to occur. Figure 4.12 shows how the zinc containing glass contains mostly Na ions, which have either one or two neighbours.

Given the high concentration of sodium in the system, this is consistent with a somewhat even distribution, where a number of short channels and isolated modifiers exist. In fact, the number of isolated Na ions is nearly three times as high as in the base glass. The clusters in the sodium silicate glass tend to be generally larger, as each sodium ion sees between two and four other ions. This helps to explain the larger agglomerates of 10-20 sodium atoms seen for example in the bottom left of figure 4.10 (a). It is worth noting, that the length of the cutoff chosen does not grossly alter the relative shape of the distribution shown in figure 4.12, but merely shifts it towards a higher or lower number of neighbors for larger and smaller cutoffs respectively.

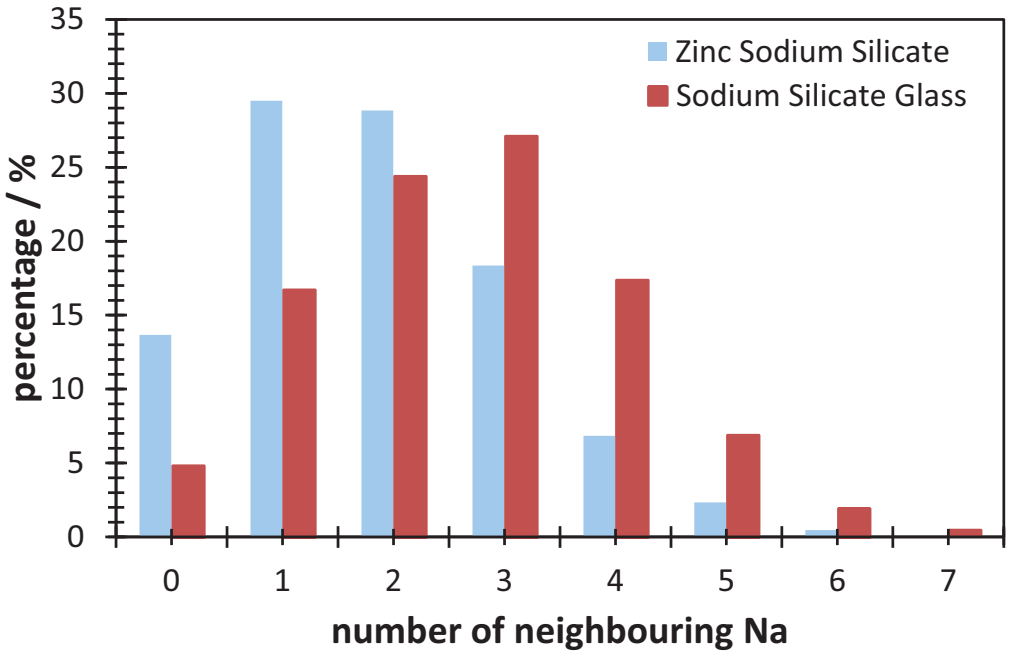

Figure 4.12 – Distribution of the number of neighbouring Na ions within 3.7 Å of a Na ion.

ZnO addition is therefore related to a significant change in the cluster size distribution as illustrated in figure 4.13, which was plotted using the same cutoff value of 3.7 Å. In the zinc sodium silicate glass, Na ions are distributed into smaller clusters compared to the extensive clustering found in a pure sodium silicate glass. In the case of nuclear waste glasses, the impact of such structural differences may significantly alter the performance of the waste form in a corrosive environment. The accumulation of sodium ions in large clusters could lead to local regions more prone to dissolution through ion exchange, as corrosion may preferentially target those areas of the glass rich in alkali. In the case of large clusters, this could then lead

to an increase in the surface area available for further corrosion. A more than 90% decrease in the surface area of a zinc-containing bioglass after 48 hours of soaking in an aqueous solution compared to the base glass was previously reported by Lusvardi *et al. [141].* Depending on the size and shape of the weakened area, localised corrosion may also lead to mechanical cracking and fracturing of the glass along alkali rich channels [106]. A glass with added ZnO may therefore be expected to perform better in a corrosive environment, at least in part due to the abscence of more extensive sodium clusters. This is a bulk effect and thus in contrast to other investigations such as that of Lusvardi *et al.* [141] who attribute the improvement in durability with added ZnO to changes in sodium ion configurations on the glass surface.

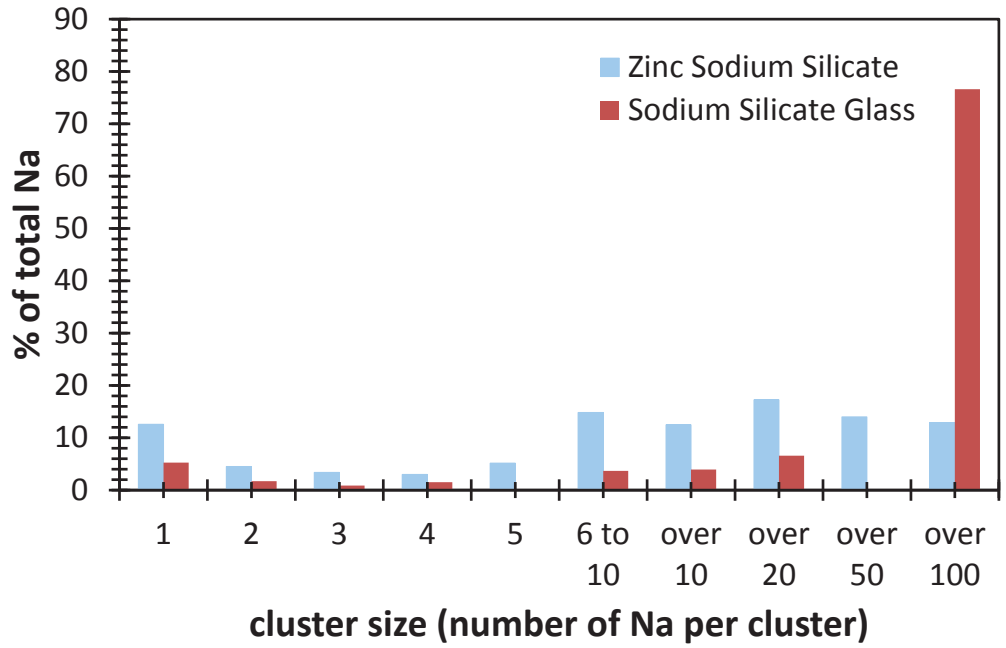

Figure 4.13 – Sodium clustering as expressed by the number of Na ions per cluster for a 3.7 Å Na-Na cutoff.

5 Lithium Conducting Fluoride Glasses

The work on which this chapter is based was published under the title "Predicted structure, thermo-mechanical properties and Li ion transport in $LiAlF_4$ glass" in the Journal of Non-Crystalline Solids [21].

The rise of electric cars and portable electronics brings with it a series of material challenges [149]. A key issue in the design of such devices is finding a suitable way to provide the electrical energy on the move. While on-board generation of electricity from solar power, fossil fuels or even hydrogen is possible, the most common solution is the use of batteries. The large amount of energy that is needed in a small and light-weight package, limits the selection of suitable materials. Lithium and its compounds are key in the making of portable batteries [150].

The popularity of lithium compounds in battery applications is largely due to lithium's low atomic mass (it is the third lightest element), leading to a very high *gravimetric charge density* (i.e. the charge that can be stored per unit of mass). Li ions are also very small, which means that a lot of charge can be stored per unit volume, often referred to as the *volumetric charge density*. Unfortunately, Li-based batteries are not without their flaws: a major concern is the high chemical reactivity of lithium. Elemental lithium reacts violently with water, and even the compounds used in batteries (such as $LiCoO_2$) are often highly reactive and not stable at elevated temperatures. This can lead to durability issues and safety risks. In January 2013, for example, the entire fleet of Boeing 787 "Dreamliner" aircraft were temporarily grounded by the U.S. Federal Aviation Administration, due to a fire caused by overheating of the on-board Li-ion battery [151, 152].

An additional problem with Li-ion batteries, which is relevant to many consumer electronics is associated with the charge/discharge cycles of Li-ion batteries over their lifetimes. The high reactivity of lithium compounds often leads to the formation of a solid electrolyte interphase (SEI) that is formed at the anode by reductive decomposition of the electrolyte, particularly at elevated temperatures [150, 153]. The formation and build-up of the SEI over continuous charge/discharge cycles can inhibit the migration of charge carriers across the interface, thereby degrading the maximum capacity of the battery over time. A possible solution to this problem is the use of a surface-modifying coating, which provides passive protection of the

anode [20, 150, 154, 155]. Amorphous coatings in the LiF.AlF_3 system have been proposed as a candidate material for such a coating, as they can be deposited in very thin layers (~200nm) by thermal evaporation [20]. This system had already been investigated in the 1980s for applications in electrochromic devices, as the resulting glass combines Li-ion conductivity with optical transparency [54, 56, 156]. For a glass and thin-film material, the cationic conductivity of $LiAlF_4$ is fairly high, reported to lie between 10^{-6} and $10^{-4}\,S\,m^{-1}$ at room temperature, depending on the ratio of LiF to AlF_3, with best results observed at close to a 1:1 ratio [54,156].

In this section molecular dynamics (MD) simulations of $LiAlF_4$ glasses are presented, in the hopes that a better understanding of the structure will enable safer and more durable Li-ion batteries or better performing Li-ion conducting materials for electrochromic devices. Interatomic potentials to model these glasses are derived from related crystal phases and are then used to make predictions of the structure and properties of such glasses.

5.1 Related Crystal Structures

In order to obtain sensible interatomic potentials for a new system with very little existing observations of structures or properties, a common approach is to use related crystal structures as a basis for the interatomic potentials [60]. Three crystalline phases which are relevant to this investigation exist, which contain the same set of elements that are found in the glass: LiF, AlF_3 and α-Li_3AlF_6. While it may seem expedient to only consider the α-Li_3AlF_6 crystal structure (of which the α-modification is the most stable at room temperature and pressure [82, 157]), basing the potential model on several structure improves the transferability of the model [60, 81]. Apart from these three phases, a crystalline phase of composition $LiAlF_4$ was claimed to have been found by Garton and Wanklyn in 1965 [158]. They note however, that "because of the small particle size due to rapid quenching of the vapour, the diffraction lines were broad and faint." They further note that the very small quantity (~100mg) of compound easily decomposes upon which it loses 18% of its volume [158]. It seems possible that they inadvertantly analysed the local structure of a glass of composition $LiAlF_4$, which would explain why they were only able to obtain the compound in rapid quenches, and why the diffraction lines were so broad and faint. Glasses tend to have lower densities due to non-periodicity of the bonds, which would explain why a volume decrease of 18% was observed when the $LiAlF_4$ phase decomposed (or perhaps crystallised) into Li_3AlF_6 and AlF_3

phases [158].

5.2 Interatomic Potential Derivation

In order to describe the interatomic forces in the glass, a Buckingham potential was fitted to the aforementioned crystal structures of LiF, AlF_3 and α-Li_3AlF_6 using the GULP package [81]. Further details on the Buckingham potential and the derivation of the pair-potentials can be found in sections 2.4.1 and 2.6.

5.3 $LiAlF_4$ Model Glass Structure

Having previously established a suitable set of interatomic potentials for this system (see Table 2.5 in Chapter 2.6), the modelled glass structure can be obtained with the help of MD simulations and the DL_POLY_3.10 code [65]. A melt-quench approach from a high temperature of 5 300 K in the constant volume (NVT) ensemble was chosen, with the temperature being iteratively decreased by 250 K at a time and 50 ps of dynamics performed at each temperature. Initially, the high starting temperatures necessitate the volume to be fixed, for as discussed earlier, the unphysically fast quench rate would leave insufficient time for the glass volume to adjust to the new temperature. After the system had reached 300 K, a further 100 000 time steps (200 ps) of MD steps were performed, but in a constant pressure ensemble (NPT). Finally, data were collected over a final run performed in the constant volume and energy (NVE) ensemble for 5 000 timesteps. To facilitate fast temperature convergence during the quench, a Berendsen thermostat [94] was used (relaxation parameter 10 ps), but exchanged for a more accurate Nose-Hoover thermo- and barostat [60, 95, 144, 159] (relaxation parameter 2 ps) when switching to the NPT ensemble. Releasing the volume constraints by moving from an NVT ensemble to NPT and NVE ensembles in order, leads to better results, as the glass is allowed to expand or contract during the NPT stage, while the total energy of the system is conserved during the NVE stage, which removes the influences the thermo- and barostat might have. Ideally, by fixing the starting volume and then releasing it at room temperature, a good density estimate can be achieved. It is worth noting that the timescales accessible in MD are severely limited by system size and current computational resources. Even though only a small system of 8 000 atoms was considered here, the simulated quench takes only 1 ns. The

melt-quench procedure should thus not be seen as a model of a real world quench, but rather as an expedient way of arriving at stable glass structures that resemble real glasses given the limit of current computational resources. Further information about the melt-quench method can be found in Chapter 2.7.3.

The fast cooling rate of the melt-quench procedure may introduce artifacts in the strucutre, because a high-temperature structure is kinetically stabilised down to room temperature, leading to high fictive temperatures [160]. To counteract this problem, the simulated glass was re-heated to 1 800 K in the NPT ensemble and back to 300 K in 50 K steps, with 100 ps of MD performed at each temperature. This annealing procedure was repeated five times, when the difference in density between the initial and the final structure was below 0.2 %. By gradually increasing the energy of the system, atomic rearrangements which were kinetically inhibited at 300 K become possible again. The total energy per atom averaged over the final 2 000 steps was -11.92 eV.

5.3.1 Network Structure

A view of the final simulation snapshot and a close-up of the obtained structure after the melt-quench and annealing procedures are shown in Figures 5.1 and 5.2 below. The amorphous $LiAlF_4$ material is shown to exhibit a cross-linked network structure, typical of glasses (see Chapter 1.2). The amorphous $LiAlF_4$ structure features a cross-linked network of corner sharing aluminium fluoride octahedra, where the aluminium is coordinated by six fluorines. This type of network is typical for a glass, as is the observation that Al-F bonds are broken in several places coincident with nearby Li cations. This is indicative that the addition of lithium fluoride has a network modifying effect on the glass and causes the depolymerisation of F-Al-F bonds, as the presence of ionic fluorine can charge-balance non-bridging fluorines in the AlF_6 octahedra. There does not appear to be any long-range structure, as would be expected from a glass. Short-range ordering is present, however, as is evident from the presence of mostly regular octahedra. Some of these octahedra appear to distorted, however, and even a small number of tetrahedral defects can be observed. The density calculated for this structure is 2.582 g cm^3, which compares favourably to a density of 2.81 g cm^3in α-Li_3AlF_6, the closest comparable crystalline composition. Both structures contain corner-sharing AlF_6 octahedra, although these are not cross-linked in α-Li_3AlF_6, but surrounded by Li ions. As is common

in glasses, the lack of long-range order leads to a more open structure and thus lower density [13, 101]. Another comparable crystal is cryolite (Na_3AlF_6), a naturally occuring mineral of translucent appearance [82, 161]. As is the case with α-Li_3AlF_6, alkali ions (sodium in the case of cryolite), prevent the formation of bridging F ions. Of course, unlike cryolite, the predicted $LiAlF_4$ structure lacks long range order.

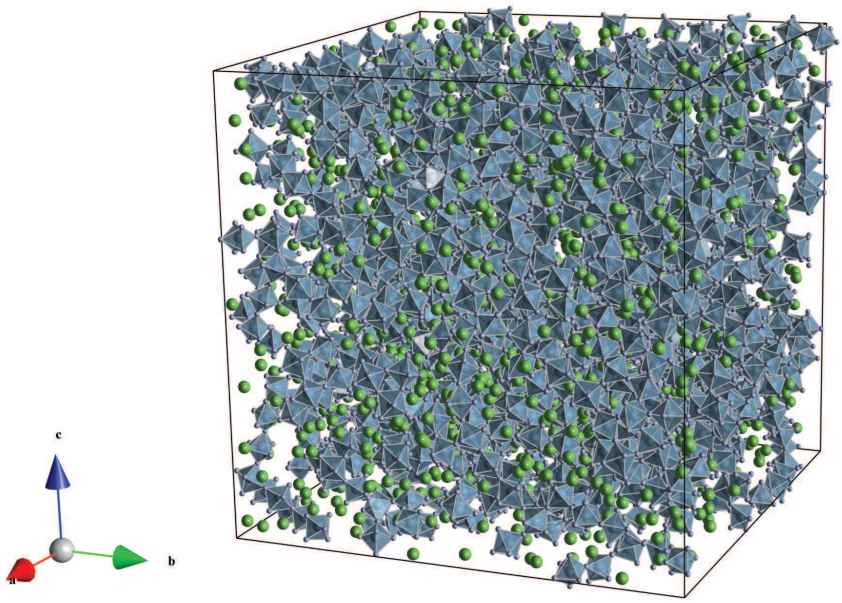

Figure 5.1 – Full simulation box view of $LiAlF_4$ glass consisting of 8 000 atoms.

5.3.2 Radial Distribution Functions

A more quantitative description of the glass structure and the lack of long-range order is available through the cumulative PDF of the glass, plotted in Figure 5.3. For the modelled composition, it shows little order beyond the first coordination shell. The lithium peaks in particular appear to be very shallow, suggesting the Li ions are only very losely bound. This suggest a high internal energy in the glass and could possibly partly explain the excellent diffusivity of lithium ions that has been observed experimentally [54, 156]. In contrast, the Al-F interaction produces a relatively narrow first peak, due to the network of octahedra in the glass.

For comparison, PDFs of crystalline Li_3AlF_6 and AlF_3 are shown in Figures 5.4 and 5.5 respectively. In the glass, the first glass peak occurs at 1.73 Å and is caused by the formation of octahedral AlF_6. The presence of such octahedra are also reflected in the next peak at 2.43 Å,

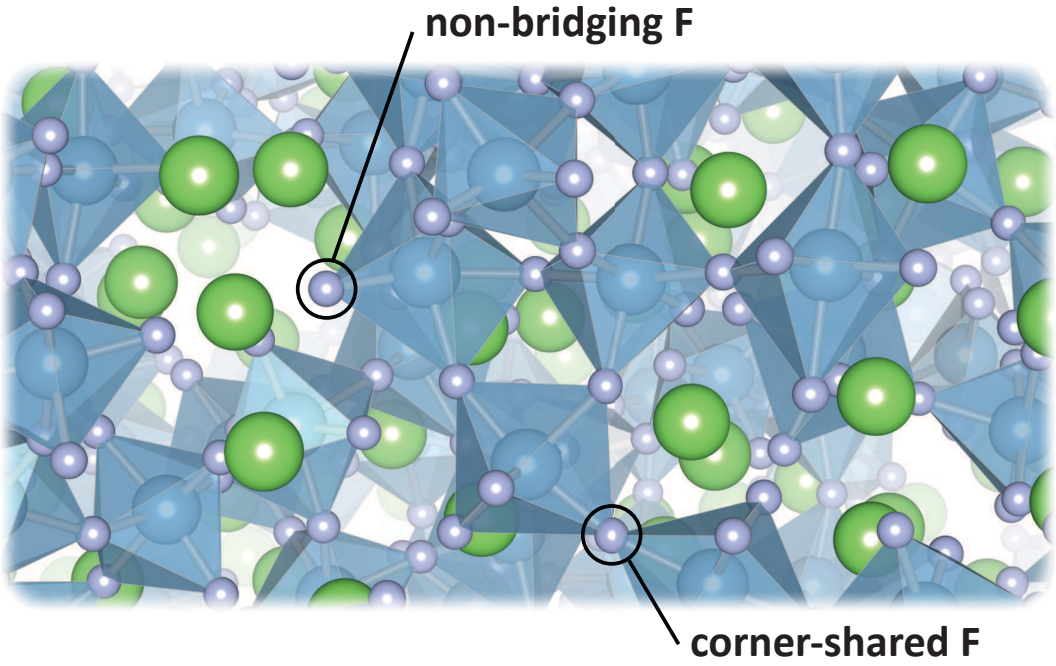

Figure 5.2 – Simulated aluminium-lithium-fluoride glass of composition $LiAlF_4$. Aluminium fluoride octahedra are shown for clarity.

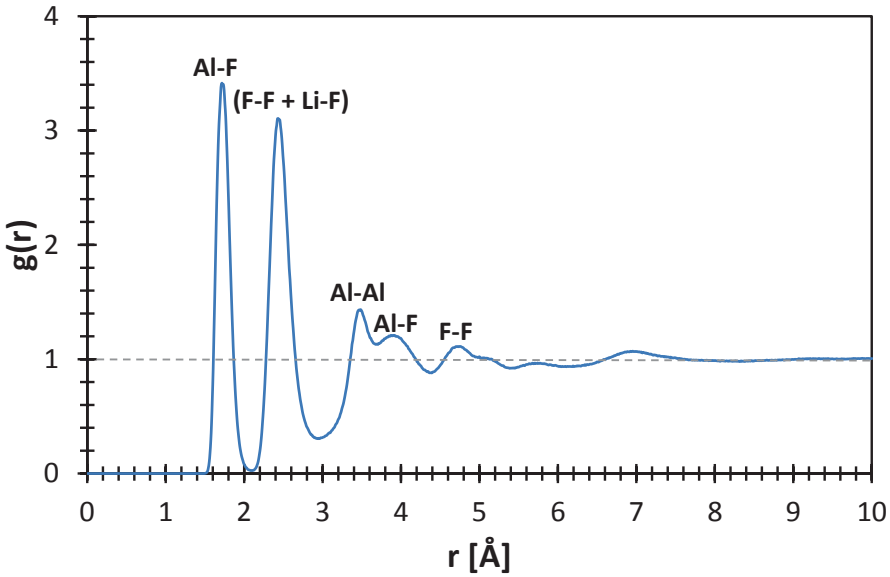

Figure 5.3 – Total pair distribution function of simulated $LiAlF_4$ glass at 300 K.

corresponding to the first F-F coordination shell. A small degree of assymetry of this peak is caused by a convolution of a bigger F-F peak with a considerably smaller and broader Li-F peak in the Li-F PDF at 2.46 Å (not shown separately).

At first glance, the total PDFs of the $LiAlF_4$ glass and the α-Li_3AlF_6 crystal appear to be very similar. Contributing to this similarity is the mobility of lithium in both structures, leading to a lack of defined Li peaks. Only a closer look at the Al-Al interaction (shown in Figure 5.6), reveals the lack of corner-sharing in the crystal structure. While Al-Al peaks beyond the first coordination shell peak at 3.48 Å are very shallow in the glass, there are a number of pronounced peaks in the crystal, including a double peak at 5.54 Å and 6.26 Å, caused by tilting and shifting of the octahedra.

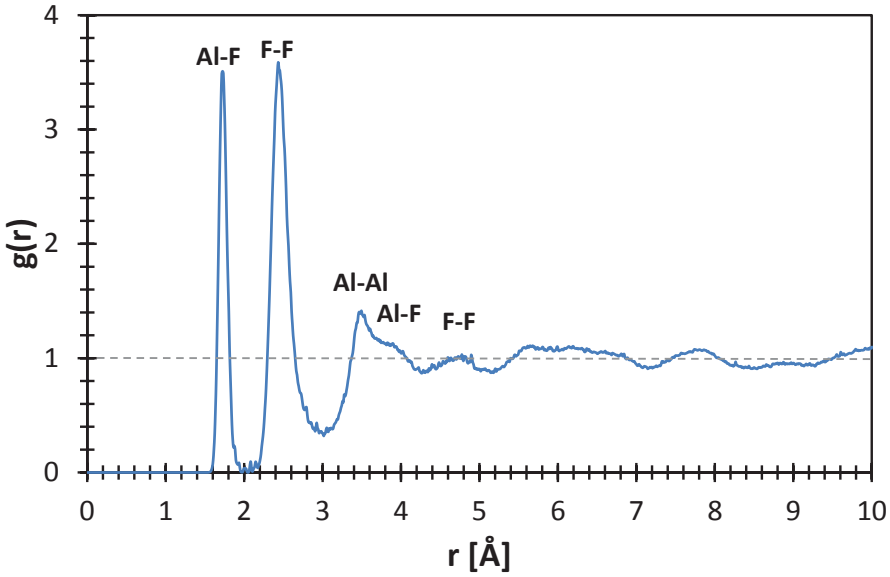

Figure 5.4 – Total pair distribution function of crystalline α-Li_3AlF_6 at 300 K.

The first peak arising from the Al-F interaction in the α-Li_3AlF_6 and AlF_3 PDFs occurs at 1.73 Å, just as it does in the glass. With the abscence of structural defects in the crystal structures, Al-F peak broadening is mostly caused by thermal vibrations, leading to peak widths at half peak height of 0.12 Å and 0.11 Å in the Li_3AlF_6 and AlF_3 crystal structures respectively at a simulation temperature of 300 K. The glass model on the other hand shows almost double the peak width at half height at 0.20 Å. The origin of this disparity is the additional disorder in the

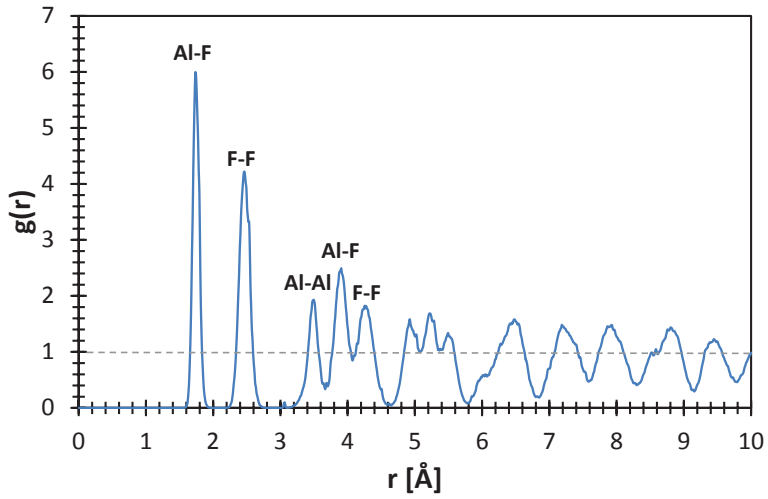

Figure 5.5 – Total pair distribution function of crystalline AlF_3 at 300 K.

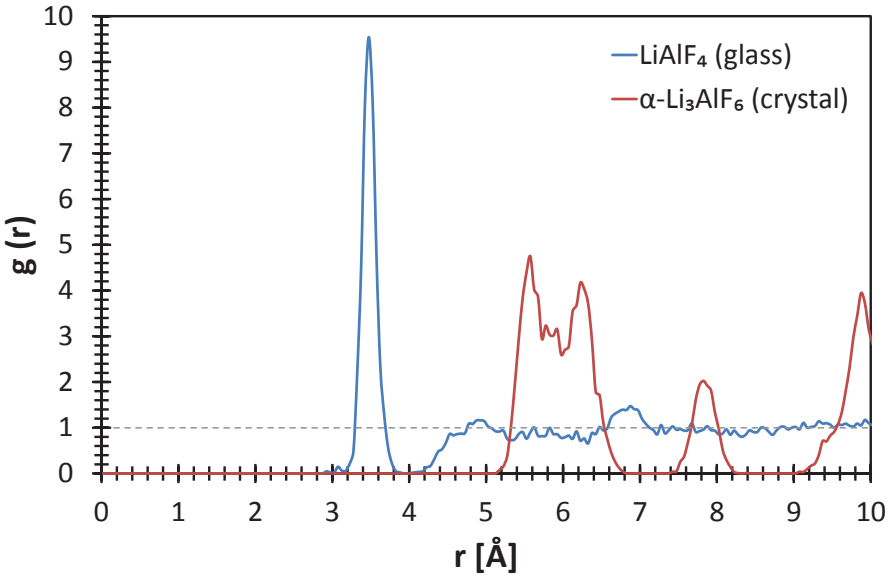

Figure 5.6 – Simulated pair distribution function of Al ion interactions in crystalline α-Li_3AlF_6 and $LiAlF_4$ glass after MD equilibration at 300 K.

glass phase. Differences between Al-F peak widths in the glass and crystals are thus attributed to bond length distortions in the AlF_6 octahedra, which occur in the variable and non-regular "defective" environment of the glass. Despite the slight peak broadening in the glass, the Al-F peak position and height in the glass is consistent with the presence of regularly shaped AlF_6 octahedra.

5.3.3 Bond Angle Distributions

The presence of regularly shaped AlF_6 octahedra is further supported by the F-Al-F bond angle distribution shown in Figure 5.7 showing a full width at half height of 11.0°. The centre of this peak is at 91.7°, which is slightly higher than the octahedral angle of 90°. A slight deviation from the perfect angle is caused by the presence of five-coordinated polyhedral defects, which furthermore contribute to the asymmetry of the peak. The polyhedral distortion also more generally contributes to broadening of the Al-F peak at 1.73 Å in the glass (see Figure 5.3) compared to the same octahedral peak in the crystals (Figures 5.4 and 5.5). A secondary peak in the F-Al-F bond angle distribution at 173.3° corresponds to a minimum in the F-Al-F internal angle along the axes of the distorted AlF_6 octahedra.

While lithium does appear to be assuming a network modifying role in the glass, this is not necessarily the case. The formation of LiF_6 octahedra has previously been observed in a synthetic Simmonsite structure (Na_2LiAlF_6) [161], which is itself very closely related to the cryolite crystal structure. LiF_6 octahedra were, however, not observed in the $LiAlF_4$ glass structure, and their presence would have led to a narrow and defined F-Li-F bond angle peak in Figure 5.8. The first small peak in the in the F-Li-F distribution occurs at 59.2°, and can be attributed to lithium atoms that are located near the edge of an AlF_6 octahedron. Assuming a triangle is formed between the fluorine edge and a nearby lithium, is with the edges of the triangle defined by the equilibrium separations of F-F and Li-F (2.43 Å and 2.46 Å respectively), this is the angle given by the sine rule. The second, very broad peak of much higher intensity is caused by the much more likely phenomenon in which Li ions are situated between corners of AlF_6 octahedra, where they are breaking an Al-F-Al bond and act as charge balancing species.

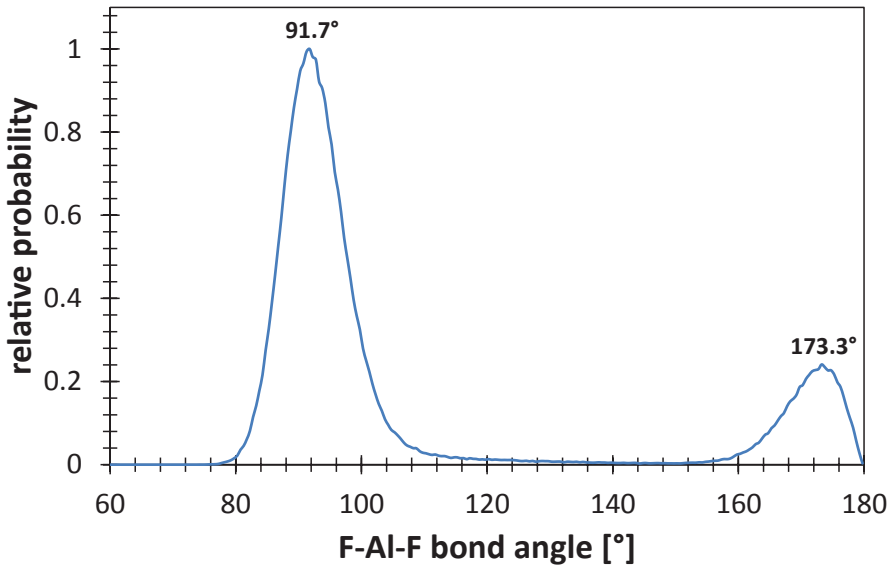

Figure 5.7 – Calculated F-Al-F bond angle distribution in $LiAlF_4$ glass after MD equilibration at 300 K.

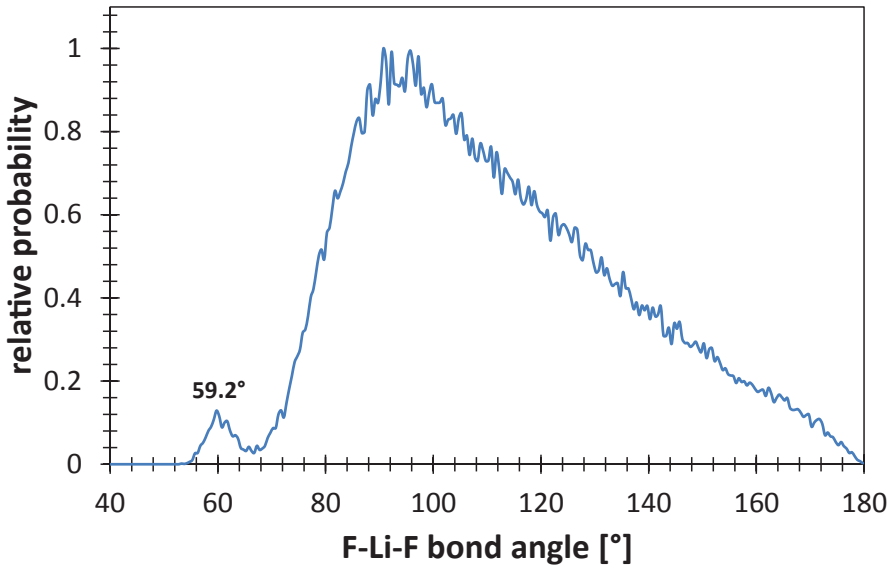

Figure 5.8 – Calculated F-Li-F bond angle distribution in $LiAlF_4$ glass after MD equilibration at 300 K.

5.4 Network Connectivity Analysis

The connectivity of the glass network is repsonsible for many key properties of glasses, as it largely accounts for the differences in structure and energy between glasses and crystals [101, 108]. Generally, in glasses only the short-range structure is well defined, whereas structure in the intermediate-range remains a topic for discussion [162, 163]. A manifestation of a glass structure is the observed lack of long-range order. The local environment of Al ions can be characterised by the coordination number and the so called Q(n) distribution.

5.4.1 Coordination and Q(n) Distribution

The coordination number is simply a count of surrounding F ions within a cutoff distance of 2.2 Å from each Al ion. This cutoff represents the first Al-F coordination shell and is defined by the first minimum in the PDF reported in Figure 5.3. While 96.8% of Al ions were found to be 6 coordinate, some 5 coordinate Al defects remained (3.2%).

The Q(n) distribution [133] on the other hand (shown in Figure 5.9), provides a count of the number of bridging fluorine ions within the first coordination shell - as such it provides a measure of the interconnectivity between the AlF_x (usually AlF_6) polyhedra. The high average network connectivity number of this glass, 3.94, indicates a highly polymerised network (note, this approaches the maximum connectivity of four exhibited by pure SiO_2 glass). Of course, AlF_6 octahedra possess six potential bridging F ions, rather than the four bridging oxygen ions of SiO_4 tetrahedra. Figure 5.9 shows that relatively few AlF_6 octahedra are fully connected to other octahedra. Nevertheless, the coordination data and Q(n) distribution are consistent with earlier comments concerning Figure 5.2, describing the glass as primarily corner sharing AlF_6 octahedra.

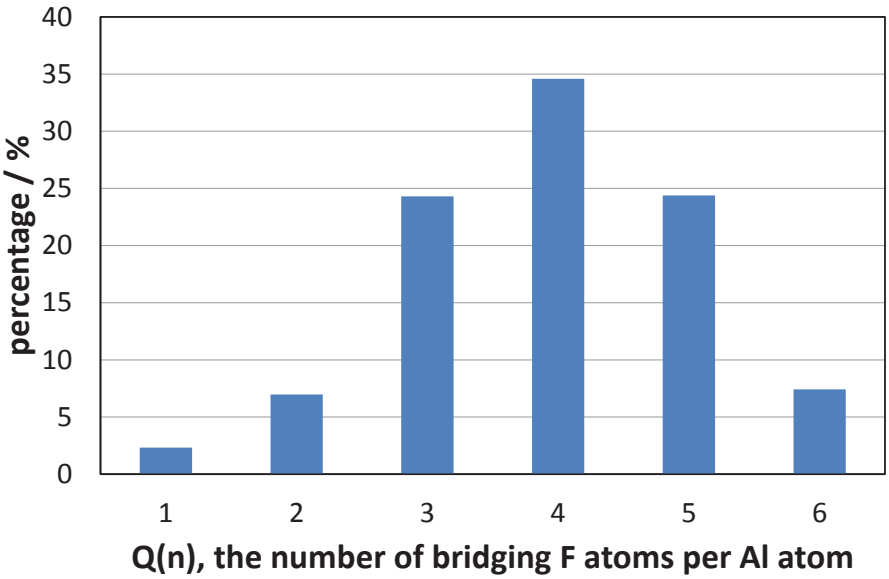

Figure 5.9 – Bonding environment of Al ions in $LiAlF_4$ glass at 300 K as identified by Q(n), the number of bridging fluoride ions between AlF_6 octahedra (cutoff 2.2 Å).

5.4.2 Ring Size Analysis

Ring size analysis (see Chapter 2.9.3) is a common tool to discuss the intermediate-range structure of glasses in more detail [99, 100]. The ring size in this case is defined as the number of octahedra incorporated in the smallest ring that can be formed for each Al ion, by forming a closed loop involving only bridging F ions and bonded Al ions. A typical four-membered ring is shown in Figure 5.10. As can be seen from the values presented in Figure 5.11, the majority of rings are three- or four-membered. This is in contrast to the broad distributions seen in silicate glasses, which usually also have a more open network structure dominated by four- to six-membered rings [100].

Figure 5.11 indicates that there are a small number of octahedra which are not part of a ring (labelled: not in ring). These are still part of the network however, as there are no octahedra without any bridging F ions (see Figure 5.11). Rather, they are members of branch structures, small open ended chains, similar to sidechains in polymers. There are a signficiant number of four-membered rings. These locally resemble small portions of a two-dimensional AlF_6 corner-sharing sheet either side of which charge compensating lithium ions sit. Due to

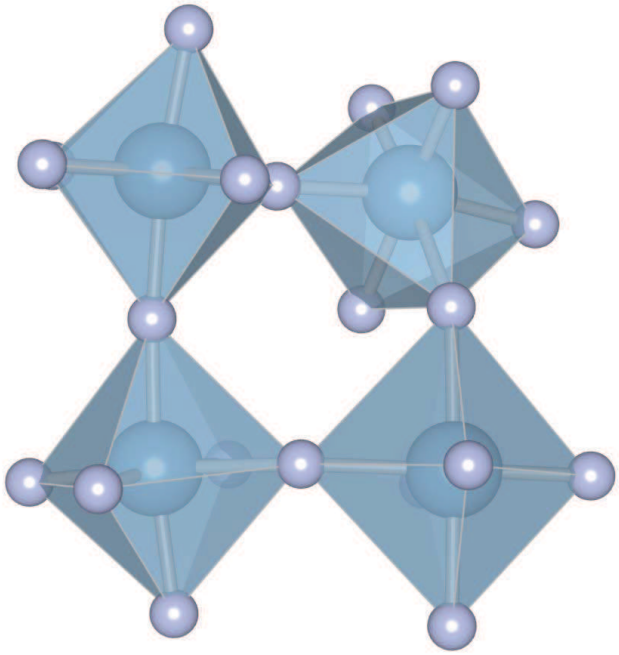

Figure 5.10 – A typical four-membered ring consisting of corner-sharing AlF_6 octahedra. Bonds which do not form part of the ring are omitted for clarity.

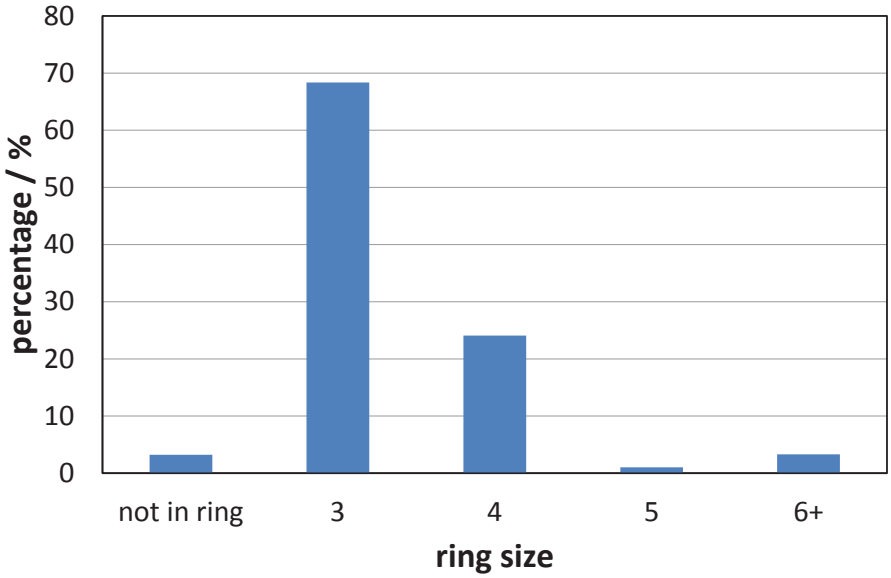

Figure 5.11 – Intermediate-range structure of $LiAlF_4$ as expressed by the ring size distribution of aluminium fluoride octahedra.

the $LiAlF_4$ stoichiometry, sheets of AlF_6 octahedra could not extend very far as, in a two-dimensional structure, there are insufficient spaces for lithium ions. One-dimensional chains and larger rings of AlF_6 octahedra offer more structural flexibility for sufficient lithium ions to fully charge compensate non-bridging F ions.

5.4.3 Modelled Physical Properties

The observed short and intermediate-range structure of $LiAlF_4$ can help to explain some of the observed physical properties. The simulated thermal expansion of the glass is shown in Figure 5.12. A change in the expansion during heating is observed at about 1340 K. This represents the glass transition temperature of the material, around which a smooth change in the thermal expansion coefficient of the material (Figure 5.12) takes place. This transition may arise due to the high degree of polymerisation in the glass, which makes it prone to deformation and movement of the polymerised rings with respect to each other, once sufficient thermal vibrational energy is available locally. Hysteresis between heating and cooling curves is caused by a variation in activation energies for the deformation of rings upon heating and cooling. Larger rings are less rigid and will deform more easily (i.e. at a lower temperature) when heating, whereas the smaller rings will only start to deform very close to the melting point. Upon cooling, both large and small rings will have sufficient energies to deform, leading to a cell length that is closer to equilibrium for that temperature.

Compared to other glasses containing network modifying species (e.g. soda-lime glass with a transition temperature of about 810 K [10]), the transition temperature is high. It is, however, still below the glass transition temperature observed in fused silica, with a value of 1500 K [10]. That the transition temperature is higher than materials such as soda-lime may be attributed to the octahedrally coordinated Al, which can accommodate more network modifiers than tetrahedal silicate glass before a breakdown of the rigid glass network, as characterised by the ring size distribution.

The lack of a crystalline phase for the $LiAlF_4$ composition meant that it was not possible to provide an accurate estimate of a melting temperature. Due to the presence of non-bridging bonds, it will most likely be slightly lower than the experimentally determined melting point of crystalline AlF_3 at 1564 K [164].

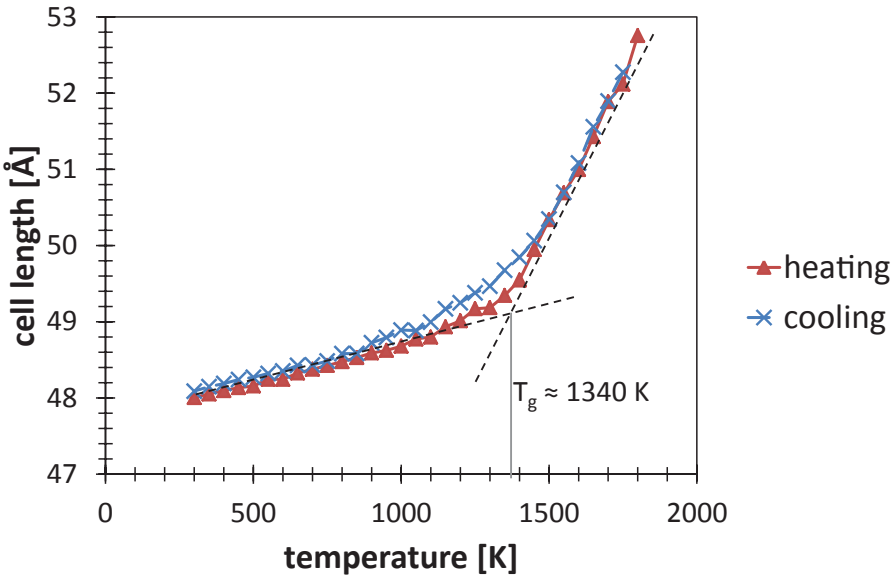

Figure 5.12 – Linear thermal expansion of a $LiAlF_4$ glass showing a glass transition at 1340 K.

The cyclic temperature data was also used to make estimates of the linear thermal expansion coefficients, α_L, which are reported in Table 5.1 for temperatures below and above the glass transition temperature. Between 1200 K and 1400 K the thermal expansion coefficient increases gradually from $26.4 \cdot 10^{-6}\,K^{-1}$ to $137 \cdot 10^{-6}\,K^{-1}$.

Table 5.1 – Predicted linear thermal expansion coefficients of $LiAlF_4$. A prediction of thermal expansion coefficients was not possible in the temperature range over which the glass transition occurs.

Range	α_L ($10^{-6}\,K^{-1}$)
300 - 1200 K	26.4
1400 - 1800 K	137.0

5.5 Ionic Conductivity in $LiAlF_4$

An understanding of mechanisms and trends concerning the ionic conductivity of $LiAlF_4$ would be of great use in predicting and optimising the performance of future lithium ion battery designs. In order to determine the ionic conductivity via simulation, the diffusivity of the various ions first needs to be established. It can be related to the mean squared displacement (MSD) of the various ions through the Einstein relation for thermal transport:

$$D_i = \frac{d}{dt}\frac{1}{6}\left\langle |r_i(t) - r_i(0)|^2 \right\rangle \tag{28}$$

where D_i is the diffusivity of element i, and $\left\langle |r_i(t) - r_i(0)|^2 \right\rangle$ is the ensemble average, equivalent to the mean squared displacement of i. This relation assumes a liquid and a sufficiently large time, t, to avoid correlation effects, so is less reliable at lower simulation temperatures [165]. The Li ions in the glass are very mobile, but by making use of the Einstein relation, it is assumed that they behave similarly to ions in a liquid state, which may not be correct for all Li ions.

The self-diffusion coefficient D_i was derived for each element at each temperature. As diffusion is a thermally activated process, it can be described as a function of temperature T by the Arrhenius relationship

$$D_i(T) = D_{i,0} \exp\left(-E_a/kT\right) \tag{29}$$

where the pre-exponential term $D_{i,0}$ describes the diffusivity of element i at infinite temperature, E_a denotes the activation energy for diffusion, and k is the Boltzmann constant. The slope of a plot of the natural log of the diffusivity versus the inverse of the temperature shows how E_a varies. Of course, the Arrhenius relationship best describes the situation for a crystal where ionic transport occurs with equivalent transitions between equivalent sites with well defined activation energies. In a glass there may be a great multitude of different transitions each with a different activation energy.

The activation energy for Li^+ diffusion is shown in Figure 5.13 (data is plotted above 600 K, as there is insufficient diffusion below 600 K to generate equilibrium MSD data). Two distinct

regions can be observed: one above and one below the glass transition temperature as identified in Figure 5.13. Around the glass transition temperature, the points do not fall easily into a smooth change. Curiously, the apparent activation energy is higher at high temperatures, which is related to the migration mechanism discussed in the next section. The activation energies are consistent with values observed for other lithium ion conducting materials developed for lithium battery applications (e.g. 0.37 eV for $Li_{0.7}TiS_2$) [166], but lower than those of lithium containing silicate glasses of the Li_2O-Al_2O_3-SiO_2 system, which have reported values of between 0.68 to 0.78 eV, depending on composition [167]. Neither Al ions, nor F ions undergo any translational diffusion on the time scale of these simulations.

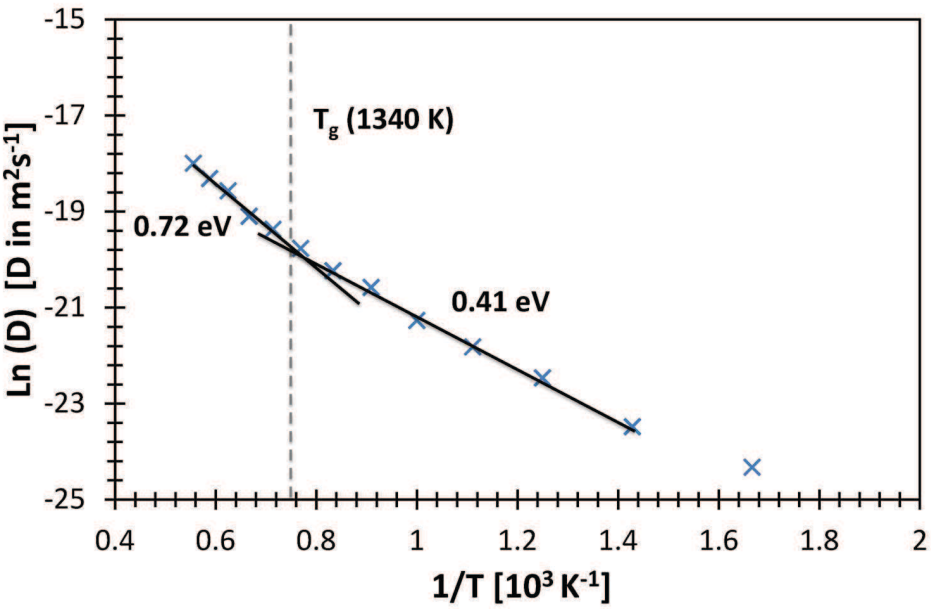

Figure 5.13 – The activation energies for diffusion of Li^+ are identified by plotting the log of Li^+ diffusivity against the inverse of temperature. Two distinct temperature ranges exist, one from 700 K to 1200 K, and the other from 1400 K to 1800 K, with associated activation energies of 0.41 eV and 0.72 eV respectively.

Generally, the diffusion of Li ions at all temperatures seems to fall into a number of regimes. This is demonstrated by the box and whisker plot in Figure 5.14, which is composed of two whiskers representing the spread in the lower and upper quartiles, and a box representing the second and third quartiles, separated by the median. Thus, Figure 5.14 shows that most atoms do not move much relative to their starting position. The upper quartile of Li ions, however, shows significantly higher diffusion than the median at all temperatures. Furthermore, these

ions are more mobile around T_g.

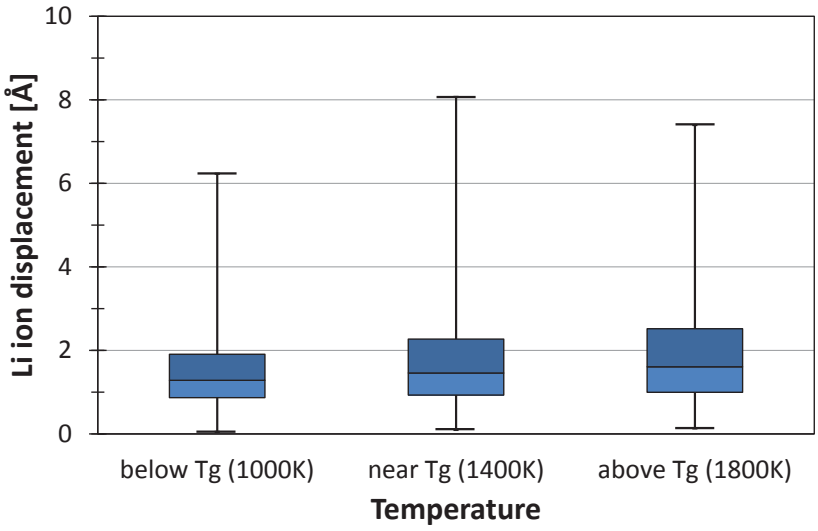

Figure 5.14 – Box and whisker plot showing the displacement of Li ions during 1 ps of equilibrium molecular dynamics at three different temperatures. Only a fraction of the ions are responsible for the observed diffusion, with the median diffusion being largely unaffected by temperature change.

The different behaviours of Li ions is further elucidated in Figure 5.15. This shows the behaviour of four characteristic Li ions. The first, Figure 5.15(A) shows an ion that is confined to one site in which it is constrained to only vibrate around a single equilibrium position. This ion would fall within the first quartile of Figure 5.14. The second, 5.15(B), is less constrained but still remains close to its original site. The motion of this ion could fall in the second quartile in the plot, but might also fall in the 3^{rd} quartile. The third graph, 5.15(C), is consistent with the ion making a transition (a jump or hop) to a second site about 2 Å away from the initial site and perhaps even a third site 4 Å distant. However, this ion moves back to its original site after a while. Thus, it may be constrained to move only between a series of sites and might not be free to move through the material large distances. The final Li ion, whose motion is depicted in Figure 5.15(D), moves a greater distance away from its original site and does not return, at least not at any point during the 1 ps reported. Such an ion may be an example of a fast moving species. In any case, its motion is facilitated by some very rapid transitions, for example, between 2 Å and 4 Å and would fall into the 4^{th} quartile of Figure 5.14.

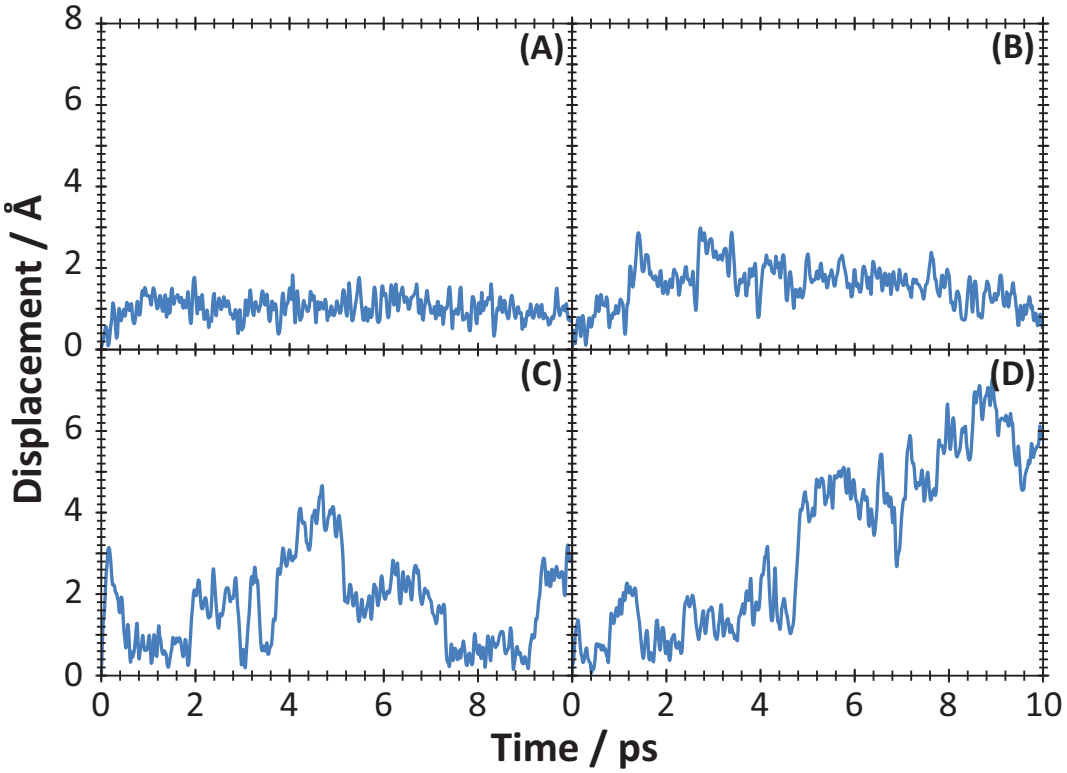

Figure 5.15 – Four distinct Li ion trajectories identified in simulations at 1000 K. Many Li ions are constrained to vibrate about their initial position (A). Other ions are less constrained but do not make a clear transition to another site (B). Conversely, (C) shows an ion that has clearly made a number of transitions but does not fully escape from its initial position. Finally (D) shows an ion that has made a permanent transition away from its original position, at least on this short time scale.

An example of the diffusion path of such a fast moving ion is shown in Figure 5.16. The motion of the Li ion is depicted over 1 ps of simulation time by its change in colour from red at the beginning to blue at the end. During the middle of the time period it is white. Thus, the diagram indicates that the Li ion moves quickly from its original positions, spends time at a central location and then moves quickly to its final position. This behaviour is, of course, typical of a hopping process as identified in Figure 5.15 (C) or 5.15 (D).

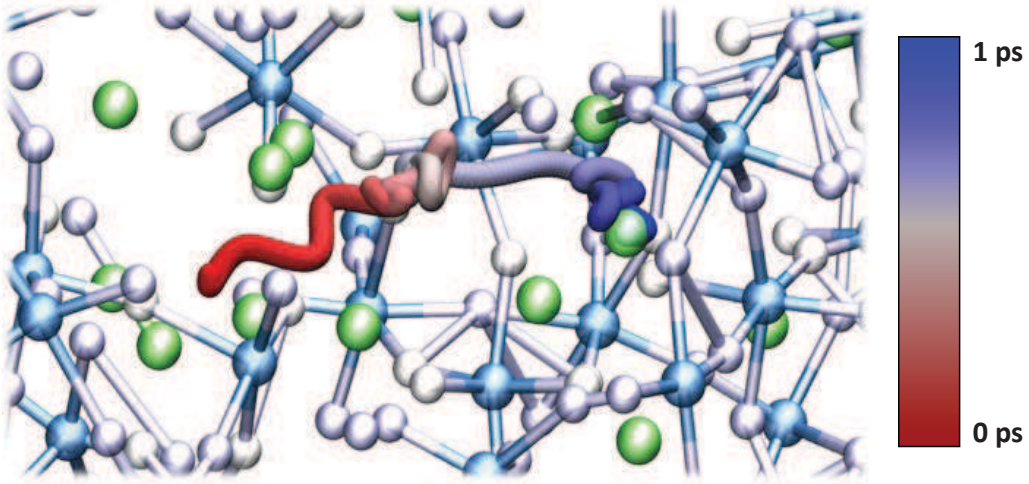

Figure 5.16 – Diagram showing part of the typical migration path of a mobile Li ion. A hopping migration of an individual Li ion at 1000 K is shown by a colour gradient from red to blue, which corresponds to 1 ps. All other ions are shown only in their final positions.

6 Summary and Conclusions

In this thesis, the relationship between the structure of glasses and their properties has been investigated. The computational technique of MD forms the basis for the study of the atomic scale structure of the two very different glass systems. One is a fluoride with a framework formed by corner sharing octahedra, the other a silicate with a framework of corner sharing tetrahedra. The use of a general technique than can be used to predict the expected properties of a range of related glasses is therefore crucial. In particular, network connectivity, thermo-mechanical properties (e.g. glass transition temperatures), and diffusivity of ions within the glasses can be considered as has been demonstrated and the results used to comment on other properties such as corrosion resistance.

6.1 Molecular Dynamics Modelling of Glasses

In this study, prior to a deeper analysis of the structure of glasses, suitable ways of deriving model glass structures had to be identified. The MD method was chosen, because it provides a computationally efficient way to model and analyse glasses at the atomic scale. While the basic properties of glasses can be explained by the random network theory and its modification [9, 103], obtaining glass structures that match experimental observations is challenging. The pair potentials used in this thesis have been shown to yield good results, capable of describing the interaction of ions in the glass. They are based on empirically or theoretically derived potential functions for various ions [60]. The functional forms employed are relatively simple and computationally tractable. The process of parameter selection was different for the two systems. In the case of the silicate, parameters were already established. Conversely for the fluoride system, new parameters were required to be derived through comparison (or fitting) to a number of crystalline structures. This multi-structure fitting approach, which de facto included a range of interatomic separations has worked for these glass structures as it has previously for crystalline materials [77].

Prior to being able to investigate more complex glasses, a suitable method of forming glasses was tested using established potentials in the silicate glass system. The widely used melt-quench procedure [46, 168–170] was used to derive simple silicate glass structures from the melt using three different established pair potential sets; the potentials published by Pedone

et al. [77, 143], the BKS potential set [78, 171] and a modification by Cormack *et al. [99]* of functions first proposed by Teter *et al. [99]*. Glass structures were derived using the same melt-quench procedure for each of these glasses and the merits of the different potentials compared.

Considering the accuracy of the density predictions, as well as PDFs, bond angles and network connectivity of the glasses derived through the various potentials, a single potential set was selected for the following work in the silicate glass system. Whilst all pair-potentials generated glasses, whose PDFs mimic experimentally derived correlation functions, the Pedone potential set showed the most promise [77,143]. The main reason for this being that the atomic structures derived using Pedone potentials showed the best agreement with glass theory and MAS NMR data. The Pedone potentials were also determined to be the most practical in the context of computational efficiency due to the good description of silicate glass structures of various compositions even at short (computationally less expensive) cutoffs [109]. The accuracy of the predictions for simple glasses, as well as the transferability, due to the large number of elements (including Zn) already included in the potential set was very useful in the context of this work.

In this thesis, one of the main aims has been to assist the development of nuclear waste glasses. Understanding the effect of radiation damage on nuclear glasses is of great importance, so it is of interest to model it; this can be done by simulating damage cascades caused by PKAs [22]. The energies involved in these radiation events is very high and so the robustness of the various potentials in these conditions needed to be considered [17]. To overcome the problems of the Buckingham potential form [60, 72] on which both the BKS [78, 171] and the Teter potentials [79] are based, traditional pair potentials were combined with a nuclear repulsion term based on the Ziegler-Biersack-Littmarck (ZBL) [80] potential. The ZBL potential term was splined (see section 2.8.1) onto the pair potential at short distances below about 2 Å, to avoid discontinuities in the potential.

Self-irradiation simulations of simple silicate glasses were performed and despite irradiating with doses equivalent to those expected during a wasteform's lifetime in a repository (thousands to tens of thousands of years), little change was observed in the volume, despite high temperature fluctuations. Nevertheless, significant structural changes were observed after the glass had been damaged. The average network connectivity was shown to decrease from 3.15

to 2.54 bonds per network-forming atom. Equally, the average ring size had risen from 5.85 to 7.99 network formers per ring. The observed changes were caused by the depolymerisation of the network; areas of high polymerisation are particularly prone to collisions, due to smaller ring size and less flexible bonding. These results suggest that the observed swelling of vitrified wastes is not directly related to the damage caused by elastic collisions of ions, despite significant structural change. However, the depolymerisation of the network may lead to more changes in the bulk properties during extended periods of recovery, which has not been modelled.

6.2 Zinc Oxide in Nuclear Waste Glasses

An investigation into the effect of zinc oxide on sodium silicate glasses was carried out, as experimental observations have shown that zinc oxide addition to a glass can enhance the corrosion resistance of the glass [47, 141, 172], as well as lower the viscosity of various nuclear waste glass compositions [140, 142]. This of great interest to the field of nuclear waste vitrification as it simplifies the processing procedure and allows higher concentrations of otherwise problematic elements such as molybdenum to be immobilised [173]. To ascertain the structural origins of these zinc induced property changes, a series of MD calculations were performed.

These simulations have facilitated a comparison of the local and intermediate structures of a simple sodium silicate glass with one in which some of the Si has been replaced with Zn. While the Dietzel field strength theory [130] predicts that ZnO is a network intermediate, here Zn atoms are shown to participate in network formation in this specific composition. Zn ions are found in ZnO_4 tetrahedra in the glass, which are incorporated into the polymerised SiO_4 matrix, matching experimental XAFS data [47]. A comparison of the PDFs of a sodium silicate glass containing ZnO to one not containing any ZnO shows similar structural peaks relating to the short-range structure of the glass. The Si-O and O-O peaks in particular, were found to be very similar in both glasses. The formation of ZnO_4 tetrahedra did not lead to a distortion of the SiO_4 tetrahedra compared to the base glass, and no other obvious distortions or polyedral structures were found that could explain the differences in glass durability and properties. By analysing the partial PDFs, it was found that the differences between the two glasses were observed in the intermediate structure, specifically in the interactions involving

Na. Further investigation of the role of Na ions in the glass showed that the disparity in the Q^n distribution, associated with a more polymerised network in a glass with added ZnO, can be explained by the distribution of Na ions within the structure. The difference in charge between the Zn^{2+} ion compared to the Si^{4+} ion in tetrahedral environments in this system helps to promote a more homogeneous distribution of Na ions in the Zn containing glass compared to the base glass, which contains large clusters of Na ions. This is supported by ring size data, showing the existance of large rings of bonded SiO_4 tetrahedra surrounding Na ion clusters in glasses not containing Zn. A cluster size analysis was also performed, showing the increased average separation between Na ions in a Zn containing glass.

The more even distribution of Na may help to explain the improved glass durability observed in Zn containing glasses. It seems plausible that without Zn ions there are pronounced localised concentrations of network modifiers, thus rendering local areas of the glass structure more susceptible to leaching and glass corrosion. This process can make the glass susceptible to continued corrosion, as it gradually increases the surface area available for further corrosion. The enhanced durability mechanism presented here, is also in agreement with experimental observations, which show that the leach rate was significantly lowered in glasses containing Zn, compared to those without, which had a significantly higher surface roughness after leaching [137, 141, 172].

6.3 Lithium-Aluminium-Fluoride Glasses

A new glass composition, which is predicted to exist in thin films derived from vapour deposition was investigated, motivated by its interesting properties, including the combination of transparency and high Li ion conductivity, which has been observed experimentally [54–56, 156]. Interest has recently been renewed in this material, due to a potential application in lithium ion batteries as a chemically inert, yet lithium conductive barrier coating [20, 150, 174]. In order to help explain and optimise the mobility of the lithium ions within the glass, a MD glass model was created based on empirically derived pair potentials as discussed above.

Suitable Buckingham type [72] pair potentials necessary for the MD model had to be derived empirically through static lattice fitting in the GULP code [81]. Three related crystal structures

(LiF, AlF_3 and α-Li_3AlF_6) were used during the potential fitting.

On the basis of these potentials, a glass of composition $LiAlF_4$ was derived through a simulated melt-quench procedure from 5300 K to 300 K in the DL_POLY_3 code [65]. Further iterative cycling of the temperature to 1800 K and back eventually led to a stable, annealed material, whose density did not change in further heating and cooling cycles. This procedure for deriving a suitable glass structure can be used in future studies.

The final structure was found to resemble that of other glasses, in that it consists of a network of polymerised polyhedra, in this case AlF_6 octahedra, with some areas being de-polymerised by the presence of network modifiers, in this case Li. The PDFs of this glass provide evidence for a well-ordered first coordination sphere of Al-F and F-F interactions, due to the regularity of the AlF_6 octahedra in the glass. An analysis of the bonding and coordination environment of the octahedra reveals a highly polymerised glass matrix, in which the Li ions are spread out. The rigidity of this matrix allows high mobility for certain Li ions, which were observed to migrate in a hopping process between metastable Li positions, akin to interstitial sites in a crystalline material. While the average activation energy for Li ion migration below the glass transition temperature is relatively low at 0.41 eV, only a fraction of the Li ions have the necessary energy to permanently move to a new site, because not all migration barriers can be overcome at these temperatures.

Interestingly, the material exhibits significant diffusion both below and above the glass transition temperature, which is estimated to be around 1340 K. Diffusion may even be fastest at, or near, the glass transition giving rise to the observed lack of a smooth transition between lower and upper temperature regimes. However, no dramatic change in the diffusion mechanism was observed at the glass transition temperature.

It is worth noting that the properties under investigation here were those of a bulk $LiAlF_4$ glass. Diffusion along interfaces between the glass thin film and the electrode or electrolyte in a lithium ion battery could be significantly different due to surface effects [87, 175]. $LiAlF_4$ is an interesting and unusual glass-forming material, which holds significant promise for application in lithium ion battery technologies.

7 Further Work

The investigation into the structure and properties of two specialised glasses in this work has raised a number of interesting issues, which have occured both during and as a result of the work presented here.

7.1 Durability of Nuclear Waste Glasses in Aqueous Enviroments

The durability of nuclear waste glasses in water, as well as the distribution of alkalis in the waste material are important concepts that require further attention. Only relatively simple glass compositions were considered in this thesis, so to extend this work, the incorporation of different elements into the model would help to establish the role of each element, as well as the interactions between these elements. Whilst the sodium silicate glass compositions described in this thesis are related to nuclear waste glasses, an extended model could include the network former boron. Deriving and incorporating a suitable boron potential into the Pedone potential set should be an objective for further work. Despite the aforementioned difficulties in accurately modelling boron oxide in multi-component glasses, it is possible to model boron containing glasses using classical MD in cases where only one type of bonding is experimentally observed for boron in that composition [46]. Although the enhanced durability effect of zinc was also observed in boron containing glasses [48, 140] it would be interesting to investigate the atomic level effect of zinc on these glasses, as they already contain two network forming species. The effect of other elements on the structure and properties of glasses should also be considered, in particular regarding their interplay with zinc. While CaO is commonly added along with ZnO, the corrosion resistance improvement from CaO addition appears to be less pronounced [140], which may originate from a somewhat different structural role of Ca.

Finally, incorporating different alkali ions within such glass compositions should be studied. The effect of different alkalis on structure and chemistry may make it easier to effectively immobilise problematic alkaline isotopes, such as ^{137}Cs, which along with ^{90}Sr is one of the primary sources of radiation in nuclear waste during the first 500 years of storage [22]. Expanding the potential set could also enable a combined study of the radioactive isotopes ^{103}Ru/^{106}Ru and ^{134}Cs/^{137}Cs, which are of great concern, as they can volatilise during glass

formation [17]. This places limits on the processing temperatures, meaning that some crystalline phases will not melt. Additionally, Ru is known to precipitate from the waste as colloidal RuO_2 particles, forming a refractory at the bottom of the induction melter. It has been observed that as much as 50% of Ru in the waste stream is left in the reprocessing plant dissolver [17], necessitating regular maintenance and the removal of the refractory formed. A better understanding of the behaviour of these two elements would allow us to predict ways of stabilising Ru and Cs within the melt and the final waste product, leading to more efficient processing and a better wasteform. However, a model of these systems would first require the accurate representation of glass-crystal interfaces on the atomic scale.

A previous study by Rushton [46] has investigated the effects of glass-crystal interfaces. By adaptation of the current glass model, it would be possible to predict interfacial energies and diffusion along interfaces. Diffusion is of particular relevance to nuclear waste, as these processes, both thermal and athermal, may allow dangerous radionuclides to migrate to the surface and potentially leave the wasteform. An investigation of the mixed alkali effect may offer insights into the migration kinetics of the alkali Cs in a mixed-alkali glass, as is predicted that the mixing of alkalis reduces "hopping" between sites [104, 148].

The effect of zinc on the clustering behaviour of alkali species in the glass, as discussed in this work, may have further benefits in applications where smooth glass surfaces need to be maintained over extended periods of time. Aging of glasses is a serious problem in the photovoltaic industry, as the processing of flat glasses is often not performed at the same facility or company that produces the glass. Stockpiling and transport can cause several months to pass before the glass is further processed, during which significant aging effects through degradation of the glass surface can occur [176]. There is significant interest in avoiding corrosion of the surface during this time and as this thesis has shown, the effect that ZnO has on the clustering behaviour of alkalis could benefit these types of glasses, assuming that other important properties (such as IR absorption bands) can be maintained.

7.2 Improvements to the Glass Model

As increased computing power becomes available with time, methods which were outside the possibilities of this work may become accessible. While MD and static lattice calculations were

appropriate to the systems and problems studied in this thesis, other simulation methods could be considered in the future. In general, there are three aspects of theoretical glass research which benefit from increased computational power:

First and foremost is the size of the modelled system; an increase in computational power allows for larger systems to be modelled. A system with several thousand atoms may be sufficient to study glass structures in general, larger simulation boxes are desirable in the simulation of glasses in particular, as they allow the study of long-range events. Radiation damage resulting from high energy ions and in-depth studies into the percolation and conductivities of network modifiers are two examples where larger may be necessary. In addition to simply expanding the system size of the MD simulation, spatial multi-scale simulations could also be performed, in which another simulation technique may be used to investigate certain glass properties in more detail at a different length scale [177]. For example, the ability to link atomic scale MD simulations to larger scale finite element simulations could be used to investigate bulk properties of glasses with atomic scale defects (such as a radiation damaged glass). This may provide insights into strengthening glass coatings or bulk glasses against cracking. This is equally detrimental to nuclear waste glasses, where it increases the surface area through which radionuclides may escape from the waste glass, as it is to protective thin film coatings in electronic devices, where cracks could lead to a breakdown of the protective effect.

The second aspect in which increased computational power is useful is in the ability to model longer time scales. As chemical processes are highly temperature dependent, a more accurate atomic scale model could be used to establish corrosion or diffusion rates for specific temperature and material conditions (surface area, impurities, radiation damage, etc.), which could feed into a second simulation in which much larger timescales could be considered. This may enable the study of the effect of long-term storage of nuclear waste glasses, including changes to elemental make-up of the waste resulting from nuclear decays, accumulating radiation damage and swelling of the glass structure and changing temperatures. A temporal multi-scale simulation could also be used to investigate the material properties of a conductive glass through a multitude of charge/discharge cycles, in which the sudden bursts of electricity may lead to long-term changes in the glass structure or chemical reactions at the glass/electrolyte or the glass/electrode interfaces [153,154]. Again, multi-scale models may be used, where one

model is used to accurately model important, yet infrequent events over short time periods, whilst another is used to describe the long-term effects on a material. Methods such as accelerated MD [178], parallel replica dynamics [179], temperature accelerated dynamics(TAD) [180] and kinetic Monte Carlo [181] exist, which whilst adding additional complexity to the modell (and thus potentially reducing the degree of transferability) could allow modelling systems over much longer time scales than those accessible with traditional MD. Some of these, such as TAD are, however, difficult to use in systems where ions are contained in potential wells with different vitrational characteristics.

The final aspect in which computational power may improve the accuracy of glass simulations is in the methods themselves. Boron oxide is an important component of many technical glasses, including most radioactive waste compositions. Unfortunately, boron oxide is difficult to model by classical MD simulation since MD relies on the accuracy of the potential model on which it is based. This can be problematic, such as with boron oxide, where the same elements can undergo different kinds of bonding: boron oxide can exist in glasses as both a trigonal BO_3 (sp^2 bonding), as well as the tetrahedral BO_4 (sp^3 bonding) form, depending on the composition of the glass, and the alkali content in particular [182]. In order to accurately model the varying bonding states, the model would have to allow for individual ions to have different short-range potentials.

One of the biggest shortcomings of classical MD is that electrons are not directly modelled. MD models are therefore limited in their transferability to systems containing the same kinds of bonding as the one on which the potential was based. One way of alleviating this problem is to use a method such as Car-Parinello MD [183], which couples the computationally intensive DFT method [57] to classical MD, thereby allowing a better description of the electronic properties and chemical bonding in the material. Rather than relying on an empirical potential, in the Car-Parinello method the MD potential is dynamically changing based on DFT calculations [183]. In addition to providing a more robust and transferable description of glasses, quantum scale models would also allow for important processes such as ionisation damage to be studied, as it explicitly allows for ions of the same species to have different oxidation states [184].

7.3 Li-conducting Aluminium Fluoride Glasses

Ionically conducting glasses are somewhat of an antithesis to nuclear waste glass compositions, as immobilising the network modifiers is desirable in nuclear waste glasses, but the opposite is true for ionically conducting glasses. Once again, it is the alkalis that are responsible for some of the most interesting properties, and deserve more extensive study. In particular, further work should concentrate on the migration of ions and establish ways of promoting Li ion conductivity, given that only a small fraction was found to be responsible for the majority of the conductivity. By tailoring the composition and the glass network structure, it may be possible to increase the proportion of mobile Li.

The study of $LiAlF_4$ glass presented in this thesis was that of a bulk material. It may be interesting, however, to consider the thin film nature of this material in its desired application as a coating and investigate any strucural changes at the interface which may lead to changes in local conductivity, as glasses are known to order near glass-crystal interfaces [185]. A thin-film study should also aim to accurately predict properties relevant to thin films, such as thermal expansivity, as well as surface energies and reconstructions.

The conductivity of this glass system is clearly dependent on the ratio of LiF and AlF_3 [54, 56, 156], but different compositions may be necessary in thin film applications if the elements segregate near the surfaces and are not evenly spread throughout the material. It would also be interesting to establish more certainly how properties such as the glass transition temperature changes as a function of composition and thereby help tailor the composition for battery applications.

Similarly to radiation damage in nuclear waste glasses, the high energies of modern lasers require transparent solids that are have very high transmittance so that they remain unaffacted. At the National Ignition Facility, only four different types of materials are currently in use: KDP (potassium dihydrogen phosphate) crystals, phosphate laser glasses, fused silica and borosilicate glasses [186]. All of them have specific surface treatments to avoid and remove any defects which can very quickly lead to catastrophic failures of the materials due to the high energies involved, which also makes them extremely expensive [186]. It would be interesting to investigate the optical properties of lithium aluminium fluoride glasses, which may have interesting absorption properties due to the absence of silicon and oxygen and may

fill a niche in optical applications.

Lithium ion batteries suffer from high cost and reactivity of lithium. Particularly for applications in which size and conditions (in particular temperature) are less of an issue, sodium ion batteries are very attractive and share much of the same technology, but may be produced at much lower cost and tend to be a lot less volatile than lithium based batteries [187]. A key challenge is to reduce the energy and volume density gap that these batteries have compared to lithium ion batteries. Theoretical work on sodium ion transport appears to be limited, opening up possibilities to study aluminium fluoride glasses using sodium as the alkali, which will also lead to a better understanding of the aluminium fluoride glass system in general.

References

[1] T. Suzuki, Nuclear Power Generation and Energy Security: The Challenges and Possibilities of Regional Cooperation, Technical Report, The James A. Baker III Institute for Public Policy of Rice University **(2000)**.

[2] U.S. Energy Information Administration, OPEC and non-OPEC oil production 1970-2020 **(1999)**, URL http://www.eia.gov/ftproot/presentations/ieo99_3im/sld010.htm, Last accessed: 20 May 2013.

[3] J. Mouawad, Oil Prices Pass Record Set in '80s, but Then Recede. New York **(2008)**, URL http://www.nytimes.com/2008/03/03/business/worldbusiness/03cnd-oil.html, Last accessed: 20 May 2013.

[4] 2012 Key World Energy Statistics, Technical Report, International Energy Agency, Paris **(2012)**.

[5] S. Carnot, *Réflexions sur la puissance motrice du feu et sur les machines propres à développer cette puissance*, Bachelier Libraire, Paris **(1824)**.

[6] International Energy Agency, Supply shock from North American oil rippling through global markets **(2013)**, URL http://www.iea.org/newsroomandevents/pressreleases/2013/may/name,38080,en.html.

[7] Intergovernmental Panel on Climate Change, Climate Change 2007 : An Assessment of the Intergovernmental Panel on Climate Change, Technical Report November, IPCC **(2007)**.

[8] J. Owen, Ancient Egyptian City Yields World's Oldest Glassworks **(2005)**, URL http://news.nationalgeographic.co.uk/news/2005/06/0616_050616_egyptglass.html, Last accessed: 04.02.2013.

[9] F. W. H. Zachariasen, The Atomic Arrangement in Glass. *Journal of the American Chemical Society* **(1932)**, Vol. 54, pp. 3841–3851.

[10] H. G. Pfaender, *Schott Guide to Glass*, Chapman and Hall, London **(1996)**.

[11] R. J. Mortimer, Electrochromic Materials. *Annual Review of Materials Research* **(2011)**, Vol. 41, pp. 241–268.

[12] C. Stalhandske, The impact of refining agents on glass colour. *Glasteknisk Tidskrift* **(2000)**, Vol. 55, pp. 65–71.

[13] B. Myson and P. Richet, *Silicale Glasses and Melts - Properties and Structure*, 1st ed., Elsevier, London **(2005)**.

[14] Schott AG, Radiation Shielding Glass, Product Description **(2013)**, URL http://www.schott.com/architecture/english/products/radiation-shielding-glass.html, Last accessed: 15 April 2013.

[15] D. Shi, *Biomaterials and Tissue Engineering*, Springer, Berlin **(2004)**.

[16] I. W. Donald, B. L. Metcalfe, and R. N. J. Taylor, Review - The immobilization of high level radioactive wastes using ceramics and glasses. *Journal of Materials Science* **(1997)**, Vol. 32, pp. 5851–5887.

[17] M. Ojovan and W. Lee, *An Introduction to Nuclear Waste Immobilisation*, 1st ed., Elsevier, London **(2005)**.

[18] I. W. Donald, *Waste Immobilization in Glass and Ceramic Based Hosts*, Wiley **(2010)**.

[19] J. A. Harrington, *Infrared Fibres and Their Applications*, The International Society for Optical Engineering, Washington **(2004)**.

[20] C. Ban, D. Gillaspie, Z. Wu, Y. Jung, G.-h. Kim, and A. Dillon, Effect of Surface Coatings on Electrochemical Behavior of Li-ion Materials. San Francisco **(2010)**.

[21] T. Stechert, M. Rushton, R. Grimes, and A. Dillon, Predicted structure, thermo-mechanical properties and Li ion transport in LiAlF4 glass. *Journal of Non-Crystalline Solids* **(2012)**, Vol. 358, pp. 1917–1923.

[22] R. C. Ewing, W. J. Weber, and F. W. Clinard, Radiation Effects in Nuclear Waste Forms for High-level Radioactive Waste. *Progress in Nuclear Energy* **(1995)**, Vol. 29, pp. 63–127.

[23] Managing the Nuclear Legacy: A strategy for action, Technical Report, Department of Trade and Industry, London **(2002)**.

[24] D. Rhodes, NNL Nuclear Training Course: Encapsulation Technologies, Presentation. Leeds **(2009)**.

[25] D. Rhodes, NNL Nuclear Training Course: History of Sellafield, Presentation. Leeds **(2009)**.

[26] W. Weaver, NNL Nuclear Training Course: Fission reactors - Current types, Presentation. Leeds **(2009)**.

[27] T. Beattie, NNL Nuclear Training Course: Implementing Geological Disposal in the UK, Presentation. Leeds **(2009)**.

[28] W. E. Lee and R. W. Grimes, Nuclear waste: a UK perspective. *Energy Materials* **(2006)**, Vol. 1, p. 22.

[29] Wikipedia, Binding Energy **(2006)**, URL http://en.wikipedia.org/wiki/File:Binding_energy_curve_-_common_isotopes.svg, Last accessed: 15 March 2013.

[30] K. D. Reeve and J. L. Woolfrey, Accelerated irradiation testing of Synroc using fast neutrons: I, First results on barium hollandite, perovskite, and undoped Synroc B. *Journal of the Australian Ceramics Society* **(1980)**, Vol. 16, pp. 10–15.

[31] K. E. Sickafus, L. Minervini, R. W. Grimes, J. A. Valdez, M. Ishimaru, F. Li, K. McClellan, and T. Hartmann, Radiation Tolerance of Complex Oxides. *Science* **(2000)**, Vol. 289, pp. 748–751.

[32] K. E. Sickafus, R. W. Grimes, J. A. Valdez, A. Cleave, M. Tang, M. Ishimaru, S. M. Corish, C. R. Stanek, and B. P. Uberuaga, Radiation-induced amorphization resistance and radiation tolerance in structurally related oxides. *Nature materials* **(2007)**, Vol. 6, pp. 217–23.

[33] Wikipedia, Isotopes and Half-life **(2009)**, URL http://commons.wikimedia.org/wiki/File:Isotopes_and_half-life.svg, Last accessed: 9 March 2013.

[34] P. D. Wilson, NNL Nuclear Training Course: Reprocessing and Recycling, Presentation. Leeds **(2009)**.

[35] P. D. Wilson, *The Nuclear Fuel Cycle*, Oxford University Press, Oxford **(1996)**.

[36] Washington State Department of Health, An Overview of Hanford and Radiation Health Effects **(2005)**, URL http://www.doh.wa.gov/hanford/publications/overview/overview.html, Last accessed: 04 Dec 2010.

[37] S. O. W. Department Of Ecology, Columbia River Basin Water Management Program **(2010)**.

[38] BBC News, Washington State nuclear waste tanks 'leaking' **(2013)**, URL http://www.bbc.co.uk/news/world-us-canada-21555902, Last accessed: 16 May 2013.

[39] G. Mackay, NNL Nuclear Training Course: Major Nuclear Accidents: A personal view, Presentation. Leeds **(2009)**.

[40] P. D. Wilson, NNL Nuclear Training Course: Familiarisation with Nuclear Technology - Advanced Issues, Presentation **(2009)**.

[41] M. Holt, R. J. Campbell, and M. B. Nikitin, Fukushima Nuclear Disaster, Technical Report, U.S. Congressional Research Service, Washington D.C. **(2012)**.

[42] R. D. Spence and C. Shi, *Stabilization and Solidification of Hazardous, Radioactive, and Mixed Wastes*, CRC Press, New York **(2005)**.

[43] J.-S. Kim, S.-K. Kwon, M. Sanchez, and G.-C. Cho, Geological storage of high level nuclear waste. *KSCE Journal of Civil Engineering* **(2011)**, Vol. 15, pp. 721–737.

[44] Committee on Disposition of High-Level Radioactive Waste Through Geological Isolation (U.S.), *Disposition of High-Level Waste and Spent Nuclear Fuel: The Continuing Societal and Technical Challenges*, National Academy Press, Washington D.C. **(2001)**.

[45] A. Ringwood, S. Kesson, N. Ware, W. Hibberson, and A. Major, Immobilisation of High Level Nuclear Reactor Wastes in SYNROC. *Nature* **(1979)**, Vol. 278, pp. 219–223.

[46] M. J. D. Rushton, R. W. Grimes, and S. L. Owens, Predicted Changes to Alkali Concentration Adjacent to Glass-Crystal Interfaces. *Journal of the American Ceramic Society* **(2008)**, Vol. 91, pp. 1659–1664.

[47] N. J. Cassingham, M. C. Stennett, P. A. Bingham, G. Aquilanti, and N. C. Hyatt, The Structural Role of Zn in Nuclear Waste Glasses. *International Journal of Applied Glass Science* **(2011)**, Vol. 2, pp. 343–353.

[48] P. Trocellier, S. Djanarthany, J. Chene, A. Haddi, A. Brass, S. Poissonnet, and F. Farges, Chemical durability of alkali-borosilicate glasses studied by analytical SEM, IBA, isotopic-tracing and SIMS. *Nuclear Instruments and Methods in Physics Research B* **(2005)**, Vol. 240, pp. 337–344.

[49] M. I. Ojovan, J. M. Juoi, and W. E. Lee, Application of Glass Composite Materials for Nuclear Waste Immobilization. *Journal of the Pakistan Materials Society* **(2008)**, Vol. 2, pp. 72–76.

[50] T. J. Garino, T. M. Nenoff, J. L. Krumhansl, and D. X. Rademacher, Low-Temperature Sintering Bi-Si-Zn Oxide Glasses for Use in Either Glass Composite Materials or Core/Shell 129I Waste Forms. *Journal of the American Ceramic Society* **(2011)**, Vol. 2419, pp. 2412–2419.

[51] A. A. Digeos, J. A. Valdez, K. E. Sickafus, S. Atiq, R. W. Grimes, and A. R. Boccaccini, Glass matrix / pyrochlore phase composites for nuclear wastes encapsulation. *Journal of Materials Science* **(2003)**, Vol. 8, pp. 1597 – 1604.

[52] W. E. Lee, M. Gilbert, S. T. Murphy, and R. W. Grimes, Opportunities for Advanced Ceramics and Composites in the Nuclear Sector. *Journal of the American Ceramic Society* **(2013)**, Vol. 96, pp. 2005–2030.

[53] E. M. Michie, R. W. Grimes, and A. R. Boccaccini, Hot-pressed phosphate glass-ceramic matrix composites containing calcium phosphate particles for nuclear waste encapsulation. *Journal of Materials Science* **(2008)**, Vol. 43, pp. 4152–4156.

[54] T. Oi and K. Miyauchi, Amorphous Thin Film Ionic Conductors of $mLiF.nAlF_3$. *Materials Research Bulletin* **(1981)**, Vol. 16, pp. 1281–1289.

[55] T. Oi, K. Miyauchi, and K. Uehara, Electrochromism of $WO_3/LiAlF_4/LiIn$ thin-film overlayers. *Journal of Applied Physics* **(1982)**, Vol. 53, p. 1823.

[56] T. Oi, Amorphous Lithium Fluoaluminate; US patent #4,367,267 **(1982)**.

[57] P. Hohenberg and W. Kohn, Inhomogeneous electron gas. *Physical Review B* **(1964)**, Vol. 136, pp. 864–871.

[58] B. J. Alder and T. E. Wainwright, Studies in Molecular Dynamics. I. General Method. *Journal of Chemical Physics* **(1959)**, Vol. 31, p. 459.

[59] J. B. Gibson, A. N. Goland, M. Milgram, and G. H. Vineyard, Dynamics of Radiation Damage. *Physical Review* **(1960)**, Vol. 120.

[60] D. C. Rapaport, *The Art of Molecular Dynamics Simulation*, 2nd ed., Cambridge University Press, Cambridge **(1995)**.

[61] B. M. Lee, H. K. Baik, B. S. Seong, S. Munetoh, and T. Motooka, Generation of glass SiO_2 structures by various cooling rates: A molecular-dynamics study. *Computational Materials Science* **(2006)**, Vol. 37, pp. 203–208.

[62] J. D. Van der Waals, Over de Continuiteit van den Gas- en Vloeistoftoestand. Thesis, Universiteit Leiden, Leiden **(1873)**.

[63] M. Born, *Atomtheorie des Festen Zustandes*, Teubner, Leipzig **(1923)**.

[64] W. Pauli, Über den Zusammenhang des Abschlusses der Elektronengruppen im Atom mit der Komplexstruktur der Spektren. *Zeitschrift für Physik* **(1925)**, Vol. 31, pp. 765–783.

[65] I. T. Todorov, W. Smith, K. Trachenko, and M. T. Dove, DL_POLY_3: new dimensions in molecular dynamics simulations via massive parallelism. *Journal of Materials Chemistry* **(2006)**, Vol. 16, pp. 1911–1918.

[66] C. A. de Coulomb, Premier mémoire sur l'électricité et le magnétisme. in *Histoire de l'Académie Royale des Sciences* **(1785)**, pp. 569–577.

[67] P. Ewald, Die Berechnung optischer und elektrostatischer Gitterpotentiale. *Annalen der Physik* **(1921)**, Vol. 369, pp. 253–287.

[68] U. Essmann, L. Perera, M. L. Berkowitz, T. Darden, H. Lee, and L. G. Pedersen, A smooth particle mesh Ewald method. *Journal of Chemical Physics* **(1995)**, Vol. 103, pp. 31–34.

[69] I. T. Todorov and W. Smith, THE DL_POLY_3 USER MANUAL **(2009)**.

[70] J. E. Lennard-Jones, On the Determination of Molecular Fields. II. From the Equation of State of a Gas. *Proceedings of the Royal Society A* **(1924)**, Vol. 106, pp. 463–477.

[71] J. E. Lennard-Jones, Cohesion. *Proceedings of the Physical Society* **(1931)**, Vol. 43, pp. 461–482.

[72] R. A. Buckingham, The Classical Equation of State of Gaseous Helium, Neon and Argon. *Proceedings of the Royal Society A* **(1938)**, Vol. 168, pp. 264–283.

[73] M. Born and J. E. Mayer, Zur Gittertheorie der Ionenkristalle. *Zeitschrift für Physik* **(1932)**, Vol. 75, pp. 1–18.

[74] M. L. Huggins and J. E. Mayer, Interatomic Distances in Crystals of the Alkali Halides. *Journal of Chemical Physics* **(1933)**, Vol. 1, p. 643.

[75] J. E. Mayer, Dispersion and Polarizability and the van der Waals Potential in the Alkali Halides. *Journal of Chemical Physics* **(1933)**, Vol. 1, p. 270.

[76] P. M. Morse, Diatomic Molecules According to the Wave Mechanics II. Vibrational Levels. *Physical Review* **(1929)**, Vol. 34, pp. 57–64.

[77] A. Pedone, G. Malavasi, M. C. Menziani, A. N. Cormack, and U. Segre, A New Self-Consistent Empirical Interatomic Potential Model for Oxides, Silicates, and Silica-Based Glasses. *Journal of Physical Chemistry B* **(2006)**, Vol. 110, pp. 11,780–95.

[78] G. J. Kramer, N. P. Farragher, B. W. H. van Beest, and R. Van Santen, Interatomic force fields for silicas, aluminophosphates, and zeolites: Derivation based on ab initio calculations. *Physical Review B* **(1991)**, Vol. 43, pp. 5068–5080.

[79] A. N. Cormack, J. Du, and T. R. Zeitler, Alkali ion migration mechanisms in silicate glasses probed by molecular dynamics simulations. *Physical Chemistry Chemical Physics* **(2002)**, Vol. 4, pp. 3193–3197.

[80] J. F. Ziegler, J. P. Biersack, and U. Littmarck, *The stopping and range of ions in solids*, Pergamon, New York **(1985)**.

[81] J. Gale and A. Rohl, The General Utility Lattice Program (GULP). *Molecular Simulation* **(2003)**, Vol. 29, pp. 291–341.

[82] J. H. Burns, A. C. Tennissen, and G. D. Brunton, The crystal structure of α-Li_3AlF_6. *Acta Crystallographica B* **(1968)**, Vol. 24, pp. 225–230.

[83] P. Daniel, A. Bulou, M. Rousseau, J. Nouet, J. L. Fourquet, M. Leblanc, and R. Burriel, A study of the structural phase transitions in AlF ,: x-ray powder diffraction , DSC and

Raman scattering investigations of the lattice dynamics and phonon spectrum. *Journal of Physics: Condensed Matter* **(1990)**, Vol. 2, pp. 5663–5677.

[84] K. Recker, F. Wallrafen, and K. Dupré, Directional solidification of the LiF-LiBaF3 eutectic. *Naturwissenschaften* **(1988)**, Vol. 75, pp. 156–157.

[85] D. A. Fletcher, R. F. McMeeking, and D. Parkin, The United Kingdom Chemical Database Service. *Journal of Chemical Information and Modeling* **(1996)**, Vol. 36, pp. 746–749.

[86] F. H. Allen, The Cambridge Structural Database: a quarter of a million crystal structures and rising. *Acta Crystallographica B* **(2002)**, Vol. 58, pp. 380–388.

[87] V. L. Bulatov and R. W. Grimes, Low-frequency oscillations in nanoclusters of lanthanum trifluoride. *Philosophical Magazine Letters* **(1998)**, Vol. 77, pp. 267–273.

[88] B. G. Dick and A. W. Overhauser, Theory of the Dielectric Constants of Alkali Halide Crystals. *Physical Review* **(1958)**, Vol. 112, pp. 90–103.

[89] I. Newton, *Philosophiae Naturalis Principia Mathematica* **(1687)**.

[90] L. Verlet, Computer "Experiments" on Classical Fluids. I. Thermodynamical Properties of Lennard-Jones Molecules. *Physical Review* **(1967)**, Vol. 159, pp. 98–103.

[91] D. J. Evans and G. Morriss, *Statistical Mechanics of Nonequilibrium Liquids*, 2nd ed., Cambridge University Press, Cambridge **(2008)**.

[92] J. Loschmidt, Zur Grösse der Luftmoleküle. *Sitzungsberichte der kaiserlichen Akademie der Wissenschaften Wien* **(1865)**, Vol. 52, pp. 395–413.

[93] T. Höhr, P. Pendzig, W. Dieterich, and P. Maass, Dynamics of disordered dipolar systems. *Physical Chemistry Chemical Physics* **(2002)**, Vol. 4, pp. 3168–3172.

[94] H. J. C. Berendsen, J. P. M. Postma, W. F. van Gunsteren, A. DiNola, and J. R. Haak, Molecular Dynamics with Coupling to an External Bath. *Journal of Chemical Physics* **(1984)**, Vol. 81, pp. 3684–3690.

[95] S. Nose, A unified formulation of the constant temperature molecular dynamics methods. *Journal of Chemical Physics* **(1984)**, Vol. 6, pp. 511–519.

[96] J. F. Ziegler, M. Ziegler, and J. Biersack, Nuclear Instruments and SRIM SRIM - The stopping and range of ions in matter (2010). *Nuclear Instruments and Methods in Physics Research B* **(2010)**, Vol. 268, pp. 1818–1823.

[97] W. Humphrey, A. Dalke, and K. Schulten, VMD: Visual Molecular Dynamics. *Journal of Molecular Graphics* **(1996)**, Vol. 14, pp. 33–38.

[98] A. C. Wright, *Neutron and X-Ray Amorphography*, C. J. Simmons and O. H. El-Bayoumi, Editors, The American Ceramic Society, Westerville **(1993)**.

[99] A. Cormack and Y. Cao, Molecular dynamics simulation of silicate glasses. *Molecular Engineering* **(1996)**, Vol. 6, pp. 183–227.

[100] P. Feuston and S. H. Garofalini, Empirical three-body potential for vitreous silica. *Journal of Chemical Physics* **(1988)**, Vol. 08854, pp. 5818–5824.

[101] D. R. Sadoway, MIT Open Courseware: Introduction to Solid State Chemistry, Lecture. Boston **(2009)**, URL http://ocw.mit.edu.

[102] J. O. Isard, The mixed alkali effect in glass. *Journal of Non-Crystalline Solids* **(1969)**, Vol. 1, pp. 235–261.

[103] G. N. Greaves, EXAFS and the structure of glass. *Journal of Non-Crystalline Solids* **(1985)**, Vol. 71, pp. 203–217.

[104] G. N. Greaves, W. Smith, E. Guilotto, and E. Pantos, Local structure, microstructure and glass properties. *Journal of Non-Crystalline Solids* **(1997)**, Vol. 222, pp. 13–24.

[105] P. Abraitis, F. Livens, J. Monteith, J. Small, D. Trivedi, D. Vaughan, and R. Wogelius, The kinetics and mechanisms of simulated British Magnox waste glass dissolution as a function of pH, silicic acid activity and time in low temperature aqueous systems. *Applied Geochemistry* **(2000)**, Vol. 15, pp. 1399–1416.

[106] G. N. Greaves, Structure and ionic transport in disordered silicates. *Mineralogical Magazine* **(2000)**, Vol. 64, pp. 441–446.

[107] P. Pernice and A. Aronne, The mixed-alkali effect in lithium-sodium metasilicate glasses. *Journal of Materials Science Letters* **(1991)**, Vol. 10, pp. 297–298.

[108] M. I. Ojovan and W. E. Lee, Connectivity and glass transition in disordered oxide systems. *Journal of Non-Crystalline Solids* **(2010)**, Vol. 356, pp. 2534–2540.

[109] M. Pota, A. Pedone, G. Malavasi, C. Durante, M. Cocchi, and M. Menziani, Molecular dynamics simulations of sodium silicate glasses: Optimization and limits of the computational procedure. *Computational Materials Science* **(2010)**, Vol. 47, pp. 739–751.

[110] E. J. F. Shackelford and W. Alexander, *Structure of Materials*, CRC Press, Boca Raton **(2001)**.

[111] A. C. Wright, The comparison of molecular dynamics simulations with diffraction experiments. *Journal of Non-Crystalline Solids* **(1993)**, Vol. 159, pp. 264–268.

[112] A. C. Wright, A. G. Clare, B. Bachra, R. N. Sinclair, A. C. Hannon, and B. Vessal, Neutron Diffraction Studies of Silicate Glasses. *Transactions of the American Crystallographic Association* **(1991)**, Vol. 27, pp. 239–254.

[113] X. Yuan and A. N. Cormack, Local structures of MD-modeled vitreous silica and sodium silicate glasses. *Journal of Non-Crystalline Solids* **(2001)**, Vol. 283, pp. 69–87.

[114] J. Du and A. N. Cormack, The medium range structure of sodium silicate glasses: a molecular dynamics simulation. *Journal of Non-Crystalline Solids* **(2004)**, Vol. 349, pp. 66–79.

[115] X. Yuan and A. Cormack, SiOSi bond angle and torsion angle distribution in vitreous silica and sodium silicate glasses. *Journal of Non-Crystalline Solids* **(2003)**, Vol. 319, pp. 31–43.

[116] P. Vashishta, R. K. Kalia, and J. P. Rino, Interaction potential for SiO2: A molecular-dynamics study of structural correlations. *Physical Review B* **(1990)**, Vol. 41, pp. 12,197–12,209.

[117] H. Maekawa, T. Maekawa, K. Kawamura, and T. Yokokawa, The structural groups of alkali silicate glasses determlined from ^{29}Si MAS-NMR. *Journal of Non-Crystalline Solids* **(1991)**, Vol. 127, pp. 53–64.

[118] B. Rossiter and J. Hamilton, *Physical Methods of Chemistry: Determination of Structural Features of Crystalline and Amorphous Solids (Vol. 5)*, 2nd ed., Wiley-Blackwell **(1990)**.

[119] J. Delaye and D. Ghaleb, Displacement cascades in a borosilicate glass: Influence of the level of polymerization on the cascade morphology. *Nuclear Instruments and Methods in Physics Research B* **(1998)**, Vol. 135, pp. 201–206.

[120] D. E. Farrell, N. Bernstein, and W. K. Liu, Thermal effects in 10 keV Si PKA cascades in 3C-SiC. *Journal of Nuclear Materials* **(2009)**, Vol. c, pp. 572–581.

[121] F. Mota, J. Caturla, M. Perlado, J. Moll, and A. Ibarra, Molecular dynamics study of structure transformation and H effects in irradiated silica. *Journal of Nuclear Materials* **(2009)**, Vol. 388, pp. 75–78.

[122] I. Ryazanov, V. Metelkin, and V. Semenov, Modeling of cascade and sub-cascade formation at high PKA energies in irradiated fusion structural materials. *Journal of Nuclear Materials* **(2009)**, Vol. 388, pp. 132–134.

[123] J. Delaye and D. Ghaleb, Molecular dynamics study of the influence of mobile cations on the reconstruction of an irradiated silicate glass. *Journal of Non-Crystalline Solids* **(2003)**, Vol. 330, pp. 106–121.

[124] G. Bureau, J. Delaye, S. Peuget, and G. Calas, Molecular dynamics study of structural changes versus deposited energy dose in a sodium borosilicate glass. *Nuclear Instruments and Methods in Physics Research B* **(2008)**, Vol. 266, pp. 2707–2710.

[125] T. Stechert, M. Rushton, and R. Grimes, Predicted Mechanism for Enhanced Durability of Zinc Containing Silicate Glasses. *Journal of the American Ceramic Society* **(2013)**, Vol. 96, pp. 1450–1455.

[126] N. Bobkova and S. Khot'ko, Science for Glass Productions: Zinc Oxide in Borate Glass-Forming Systems. *Glass and Ceramics* **(2005)**, Vol. 62, pp. 167–170.

[127] C. Klingshirn, ZnO: material, physics and applications. *ChemPhysChem* **(2007)**, Vol. 8, pp. 782–803.

[128] V. L. Solozhenko, O. O. Kurakevych, P. S. Sokolov, and A. N. Baranov, Kinetics of the wurtzite-to-rock-salt phase transformation in ZnO at high pressure. *Journal of Physical Chemistry A* **(2011)**, Vol. 115, pp. 4354–8.

[129] S. Baruah and J. Dutta, Hydrothermal growth of ZnO nanostructures. *Science and Technology of Advanced Materials* **(2009)**, Vol. 10, p. 013001.

[130] A. Dietzel, Die Kationenfeldstärken und ihre Beziehungen zu Entglasungsvorgängen, zur Verbindungsbildung und zu den Schmelzpunkten von Silicaten. *Zeitschrift für Elektrochemie* **(1942)**, Vol. 48, pp. 9–23.

[131] A. Varshneya, *Fundamentals of Inorganic Glasses*, 1st ed., Elsevier Inc., San Diego **(1993)**.

[132] R. D. Shannon, Revised Effective Ionic Radii and Systematic Studies of Interatomie Distances in Halides and Chaleogenides. *Acta Crystallographica A* **(1976)**, Vol. A32, pp. 751–767.

[133] J. E. Shelby, *Introduction to Glass Science and Technology*, 2nd ed., Royal Society of Chemistry, London **(2005)**.

[134] C. Nelson, T. Furukawa, and W. B. White, Transition Metal Ions in Glasses: Network Modifiers or Quasi-molecular Complexes? *Materials Research Bulletin* **(1983)**, Vol. 18, pp. 959–966.

[135] D. G. Minser, B. Walden, and W. B. White, Structure of Alkali-Zinc Silicate Glasses by Raman Spectroscopy. *Journal of the American Ceramic Society* **(1984)**, Vol. 67, pp. C47–C49.

[136] N. Bobkova and S. A. Gailevich, Structural Role of Zinc in Glasses of the Zirconium-Sodium-Borosilicate system. *Zhurnal Prikladnoi Spektraskopii* **(1983)**, Vol. 38, pp. 572–576.

[137] G. D. Mea, A. Gasparotto, M. Bettinelli, A. Montenero, and R. Scaglioni, Chemical durability of zinc-containing glasses. *Journal of Non-Crystalline Solids* **(1986)**, Vol. 84, pp. 443–451.

[138] G. Lusvardi, G. Malavasi, L. Menabue, and M. C. Menziani, Synthesis, Characterization, and Molecular Dynamics Simulation of Na2O-CaO-SiO2-ZnO Glasses. *Journal of Physical Chemistry B* **(2002)**, Vol. 106, pp. 9753–9760.

[139] G. Lusvardi, G. Malavasi, L. Menabue, U. Segre, M. Carnasciali, and A. Ubaldini, A combined experimental and computational approach to $(Na_2O)1\text{-}x.CaO.(ZnO)x.2SiO_2$ glasses characterization. *Journal of Non-Crystalline Solids* **(2004)**, Vol. 345-346, pp. 710–714.

[140] B. F. Dunnett, Investigation of the Effect of Calcium and Zinc Additions to WVP, Technical Report 2, British Nuclear Fuels Limited **(2005)**.

[141] G. Lusvardi, G. Malavasi, L. Menabue, M. C. Menziani, A. Pedone, U. Segre, V. Aina, A. Perardi, C. Morterra, F. Boccafoschi, S. Gatti, M. Bosetti, and M. Cannas, Properties of zinc releasing surfaces for clinical applications. *Journal of Biomaterials Applications* **(2008)**, Vol. 22, pp. 505–26.

[142] C. C. Ramshaw and C. E. Stephen, Summary of the study of the addition of zinc oxide to the base glass formulation for the vitrification of HA waste, Technical Report, British Nuclear Fuels Limited **(2003)**.

[143] A. Pedone, G. Malavasi, A. N. Cormack, U. Segre, and M. C. Menziani, Insight into Elastic Properties of Binary Alkali Silicate Glasses; Prediction and Interpretation through Atomistic Simulation Techniques. *Chemistry of Materials*, Vol. 19, pp. 3144–3154.

[144] W. G. Hoover, Canonical dynamics: Equilibrium phase-space distributions. *Physical Review A* **(1985)**, Vol. 31.

[145] N. Zotov and H. Keppler, The structure of sodium tetrasilicate glass from neutron diffraction, reverse Monte Carlo simulations and Raman spectroscopy. *Physics and Chemistry of Minerals* **(1998)**, Vol. 25, pp. 259–267.

[146] K.-F. Hesse, F. Liebau, and H. Böhm, Disodium Zincosilicate , $Na_2ZnSi_3O_8$. *Acta Crystallographica B* **(1977)**, Vol. 33, pp. 1333–1337.

[147] A. Fluegel, Global Model for Calculating Room-Temperature Glass Density from the Composition. *Journal of the American Ceramic Society* **(2007)**, Vol. 90, pp. 2622–2625.

[148] W. Smith, T. R. Forester, G. N. Greaves, S. Hayter, and M. J. Gillan, Molecular dynamics simulation of alkali-metal diffusion in alkali-metal disilicate glasses. *Journal of Materials Chemistry* **(1997)**, Vol. 7, pp. 331–336.

[149] EV Everywhere: Grand Challenge Blueprint, Technical Report, U.S. Department of Energy **(2013)**.

[150] Y. S. Jung, A. S. Cavanagh, A. C. Dillon, M. D. Groner, S. M. George, and S.-H. Lee, Enhanced Stability of $LiCoO_2$ Cathodes in Lithium-Ion Batteries Using Surface

Modification by Atomic Layer Deposition. *Journal of The Electrochemical Society* **(2010)**, Vol. 157, p. A75.

[151] National Transportation Safety Board (U.S.), NTSB identifies origin of JAL Boeing 787 battery fire; design, certification and manufacturing processes come under scrutiny, Technical Report, National Transportation Safety Board, Boston **(2013)**, URL http://www.ntsb.gov/news/2013/130207.html.

[152] D. Roland, Japan Airlines Finds Fault on Modified Dreamliner **(2013)**, URL http://www.telegraph.co.uk/finance/newsbysector/transport/10094460/Japan-Airlines-finds-fault-on-modified-Dreamliner.html, Last accessed: 4 June 2013.

[153] E. Peled, The Electrochemical Behavior of Alkali and Alkaline Earth Metals in Non-aqueous Battery Systems: The Solid Electrolyte Interphase Model. *Journal of The Electrochemical Society* **(1979)**, Vol. 126, pp. 2047–2051.

[154] Y. S. Jung, A. S. Cavanagh, L. A. Riley, S.-H. Kang, A. C. Dillon, M. D. Groner, S. M. George, and S.-H. Lee, Ultrathin direct atomic layer deposition on composite electrodes for highly durable and safe Li-ion batteries. *Advanced materials (Deerfield Beach, Fla.)* **(2010)**, Vol. 22, pp. 2172–6.

[155] L. A. Riley, S. Van Atta, A. S. Cavanagh, Y. Yan, S. M. George, P. Liu, A. C. Dillon, and S.-H. Lee, Electrochemical effects of ALD surface modification on combustion synthesized $LiNi_{1/3}Mn_{1/3}Co_{1/3}O_2$ as a layered-cathode material. *Journal of Power Sources* **(2011)**, Vol. 196, pp. 3317–3324.

[156] J.-M. Dance and T. Oi, Ionic conductivity of amorphous mLiF-nNiF_2 thin films. *Thin Solid Films* **(1983)**, Vol. 104, pp. 71–73.

[157] G. Garton and B. M. Wanklyn, Polymorphism in Li_3AlF_6 **(1965)**, Vol. 27, pp. 2466–2469.

[158] G. Garton and B.M. Wanklyn, Some Observations on the Tetrafluoroaluminates of Lithium and Sodium **(1965)**, Vol. 27, pp. 2461–2465.

[159] V. Rühle, Berendsen and Nose-Hoover Thermostats **(2007)**, pp. 1–4, URL http://www2.mpip-mainz.mpg.de/~andrienk/journal_club/thermostats.pdf, Last accessed: 14 February 2013.

[160] I. Farnan, P. J. Grandinetti, J. Baltisberger, J. Stebbins, U. Werner, M. Eastman, and A. Pines, Quantification of the disorder in network-modified silicate glasses. *Nature* **(1992)**, Vol. 358.

[161] K. C. Ross, R. H. Mitchell, and A. R. Chakhmouradian, The crystal structure of synthetic simmonsite, Na2LiAlF6. *Journal of Solid State Chemistry* **(2003)**, Vol. 172, pp. 95–101.

[162] M. I. Ojovan and W. E. Lee, Topologically disordered systems at the glass transition. *Journal of Physics: Condensed Matter* **(2006)**, Vol. 18, pp. 11,507–11,520.

[163] J. Stanzione III, K. Strawhecker, and R. Wool, Observing the twinkling fractal nature of the glass transition. *Journal of Non-Crystalline Solids* **(2011)**, Vol. 357, pp. 311–319.

[164] Aluminium fluoride, anhydrous, 99+%. Alfa Aeasar. Product Sheet. Last accessed: 29 Sept. 2011. http://www.alfa.com/en/GP100W.pgm?DSSTK=11497. URL http://www.alfa.com/en/GP100W.pgm?DSSTK=11497.

[165] M. P. Allen and D. J. Tildesley, *Computer Simulation of Liquids*, M. P. Allen and D. J. Tildesley, Editors, Clarendon Press, Oxford **(1989)**.

[166] M. Wilkening, W. Küchler, and P. Heitjans, From Ultraslow to Fast Lithium Diffusion in the 2D Ion Conductor $Li_{0.7}TiS_2$ Probed Directly by Stimulated-Echo NMR and Nuclear Magnetic Relaxation. *Physical Review Letters* **(2006)**, Vol. 97, pp. 1–4.

[167] W. Li and S. H. Garofalini, Molecular dynamics simulation of lithium diffusion in Li_2O-Al_2O_3-SiO_2 glasses. *Solid State Ionics* **(2004)**, Vol. 166, pp. 365–373.

[168] C. Huang and A. N. Cormack, The structure of sodium silicate glass. *Journal of Chemical Physics* **(1990)**, Vol. 93, p. 8180.

[169] A. Tilocca, N. de Leeuw, and A. Cormack, Shell-model molecular dynamics calculations of modified silicate glasses. *Physical Review B* **(2006)**, Vol. 73, pp. 1–14.

[170] A. Tilocca, Short- and medium-range structure of multicomponent bioactive glasses and melts: An assessment of the performances of shell-model and rigid-ion potentials. *Journal of Chemical Physics* **(2008)**, Vol. 129, p. 084504.

[171] G. J. Kramer, B. W. H. van Beest, and R. A. Van Santen, Relation between crystal symmetry and ionicity in silica polymorphs. *Nature* **(1991)**, Vol. 351.

[172] G. Ennas, A. Musinu, and G. Piccaluga, Structure and chemical durability of zinc-containing glasses. *Journal of Non-Crystalline Solids* **(1990)**, Vol. 125, pp. 181–185.

[173] B. F. Dunnett, N. R. Gribble, R. Short, E. Turner, C. J. Steele, and A. Riley, Vitrification of high molybdenum waste. *European Journal of Glass Science and Technology A* **(2012)**, Vol. 53.

[174] C. Ban, Z. Wu, D. T. Gillaspie, L. Chen, Y. Yan, J. L. Blackburn, and A. C. Dillon, Nanostructured Fe_3O_4/SWNT electrode: Binder-free and high-rate li-ion anode. *Advanced materials (Deerfield Beach, Fla.)* **(2010)**, Vol. 22, pp. E145–9.

[175] V. L. Bulatov, R. W. Grimes, and A. H. Harker, Mobility of ions in Lanthanum Fluoride Nanoclusters. *JOM-e* **(1997)**, Vol. 49.

[176] C. M. Lampert, Failure and Degradation Modes in Selected Solar Materials: A Review, Technical Report, International Energy Agency **(1989)**, URL http://eetd.lbl.gov/sites/all/files/publications/27814_0.pdf.

[177] M. Horstmeyer, Multiscale Modeling: A Review. in *Practical Aspects of Computational Chemistry: Methods, Concepts and Applications*, J. Leszczynski and M. K. Shukla, Editors, Springer, New York **(2009)**, Chapter 4, pp. 87–136.

[178] A. F. Voter, A method for accelerating the molecular dynamics simulation of infrequent events. *Journal of Chemical Physics* **(1997)**, Vol. 106, pp. 4665–4677.

[179] A. F. Voter, Parallel replica method for dynamics of infrequent events. *Phys. Rev. B* **(1998)**, Vol. 57, pp. R13,985—-R13,988.

[180] M. R. Sørensen and A. F. Voter, Temperature-accelerated dynamics for simulation of infrequent events. *Journal of Chemical Physics* **(2000)**, Vol. 112, pp. 9599–9606.

[181] G. Henkelman and H. Jónsson, Long time scale kinetic Monte Carlo simulations without lattice approximation and predefined event table. *Journal of Chemical Physics* **(2001)**, Vol. 115, pp. 9657–9666.

[182] C. M. Kuppinger and J. E. Shelby, Viscosity and Thermal Expansion of Mixed-Alkali Borate Glasses. *Journal of the American Ceramic Society* **(1986)**, Vol. 69, pp. C–292—-C–293.

[183] R. Car and M. Parrinello, Unified approach for molecular dynamics and density-functional theory. *Physical review letters* **(1985)**, Vol. 55.

[184] G. R. Choppin, J.-O. Liljenzin, and J. Rydberg, *Radiochemistry and Nuclear Chemsitry: Chapter 7 - Radiation Effects on Matter*, 3rd ed., Butterworth Heinemann **(2002)**.

[185] M. Rushton, R. Grimes, and S. Owens, Partial ordering of glass networks adjacent to simulated glass-crystal interfaces. *Journal of Non-Crystalline Solids* **(2011)**, Vol. 357, pp. 3278–3287.

[186] T. I. Suratwala, ECI Functional Glasses Conference; Session 24: Glass Surface Damage. Syracuse **(2013)**.

[187] S. W. Martin, ECI Functional Glasses Conference; Session 14: Glasses for Energy Storage. Syracuse **(2013)**.